

**Investigations of Ion Channels with
Computational Simulations and
Biochemical Experiments**

Thesis by

Steven Adrian Spronk

In Partial Fulfillment of the Requirements

for the Degree of

Doctor of Philosophy

California Institute of Technology

Pasadena, California

2006

(Defended February 13, 2006)

© 2006

Steven Adrian Spronk

All Rights Reserved

Acknowledgements

My graduate studies at Caltech have been a wonderful experience. First of all, working for Dennis Dougherty has been fantastic. He is an excellent scientist and a model advisor, able to keep track of all the strange turns my research has taken. I have learned a lot from talking with him about my research, but beyond that, I also aspire to be as good a writer and speaker as he is, and I admire the way he is able to balance his professional and family life.

Thank you also to Doug Rees, my thesis committee chairman, with whom I enjoyed working during my projects with mechanosensitive channels. I also appreciate the contributions and encouraging words of my other committee members, Jack Beauchamp and Peter Dervan.

The real joy in working in the Dougherty lab has been the interactions I have had with my labmates, all of whom I consider friends. Three of them deserve special recognition. First of all, Don Elmore helped me get started in the simulations, teaching me the ins and outs of the software and the maintenance of our computer system. He is always happy to help in whatever way he can. Outside of lab, he was also a fun quiz bowl teammate. Sarah Monahan taught me everything that I know about tissue culture and most everything about molecular biology. She is also a brilliant scientist and an even better person. The scientific community took a hit when she decided to do photography instead. Josh Maurer taught me whatever molecular biology Sarah did not teach me. He was full of suggestions during the many times I got stuck early in my studies.

As for my other labmates, I found a fellow White Sox fan in Justin Gallivan. Lintong Li had a desk next to me and was fun to chat with. I admire Gabe Brandt's

voracious appetite for scientific knowledge and the way he can retain so much information about everything. Although I hardly did any organic chemistry, Vince Liptak helped me in my reactions when I most needed it. Niki Zacharias often kept me company during the graveyard shift. David Dahan was a formidable opponent in fantasy hockey, as a person who actually played the sport. James Petersson's goofiness kept things light, and his work ethic and the breadth of his research, not to mention his rock-climbing skills, were inspirational. I was amazed by the variety of experiences that Darren Beene has had in his life and am glad that he decided to settle down in Pasadena for a few years, so I could get to know him. Tingwei Mu was a pleasure to play soccer with. Amanda Cashin's outgoing nature made her a great teammate of sorts as we went through interviewing for jobs and finishing up our graduate work. Lori Lee is friendly and fun, even when we talk about serious issues. Erik Rodriguez is quick to help when things really need to get done in lab. Mike Torrice is always there to catch the Simpsons and Seinfeld references I constantly throw around. Amy Eastwood's sparkling personality will take her far in life—even farther than the 26.2 miles she ran in Boston last year. Joanne Xiu is a pleasure to be around. Katie McMenimen never complained when I played my cheesy music but actually gave me more. I have truly enjoyed the conversations that I have had with Kiowa Bower, and I thank him for sharing his perspectives with me. Ariele Hanek is a caring person. Jinti Wang is a hard worker and always has a smile on her face. I admire Kristin Rule's willingness to speak her mind. Jai Shanata has been extremely patient with me when my stuff kept spilling across his desk. Kay Limapichat, I am sure, will continue in the Dougherty tradition of being the coolest lab on campus.

Friends outside of lab, both at Caltech and elsewhere, have greatly enriched my experience in Pasadena. Jeremy Heidel, my roommate for five years, and I have shared so many fun times talking, playing games, watching and playing sports, and hanging out. Endy Min has a real servant's heart and an unparalleled zest for life. Swaroop Mishra, Julie Casperson, and Tim Best often helped me over the midweek hump. Also thank you to my wonderful friends from church, my "family away from family" for the last six-and-a-half years, especially Nick Lawrence, Tim Chinniah, Paul Sutherlin, and Robert Schwenk, who have been with me since the beginning.

A special thanks is reserved for my family, even if sometimes they make fun of my nerdiness, although they are just telling it like it is. My siblings, Cindy, Karen, and Paul have helped shape me into who I am today. My parents are the best in the world and have supported me with unwavering love through all the good and bad times. In addition, my dad, who has a Ph.D. in biochemistry, has been really helpful during the many times I have struggled with experiments.

Without question, the highlight of my time in Pasadena has been finding my beautiful wife of noble character Tiffany. She has shown me more love and patience than I deserve, and I cannot imagine being with anyone else. I am a better man because of her, and I am so glad that she will be there with me wherever we end up next, and beyond.

Lastly, all the gifts that I have received—my intellect, my abilities, my love for science—come from God above and my Savior Jesus, whose strength has carried me through the difficult times. I could not have succeeded without it. I have no hope or joy except through His grace. Praise be to God!

Abstract

Chapter one describes studies of the voltage-dependent hydration and conduction properties of the hydrophobic pore of the mechanosensitive channel of small conductance, MscS. A detailed picture of water and ion properties in small pores is important for understanding the behavior of biological ion channels. Several recent modeling studies have shown that small, hydrophobic pores exclude water and ions even if they are physically large enough to accommodate them, a mechanism called hydrophobic gating. This mechanism has been implicated in the gating of several channels, including MscS. Although the pore in the crystal structure of MscS is wide and was initially hypothesized to be open, it is lined by hydrophobic residues and may represent a nonconducting state. Molecular dynamics simulations were performed on MscS to determine whether or not the structure can conduct ions. Unlike previous simulations of hydrophobic nanopores, electric fields were applied to this system to model the transmembrane potential, which proved to be important. Although simulations without a potential resulted in a dehydrated, occluded pore, the application of a potential increased the hydration of the pore and resulted in current flow through the channel. The calculated channel conductance was in good agreement with experiment. Therefore, it is likely that the MscS crystal structure is closer to a conducting than to a nonconducting state.

Chapter two describes work toward a method using protein transduction domains (PTDs) to deliver tRNA to cultured mammalian cells. *In vivo* incorporation of unnatural amino acids using nonsense suppression is a powerful technique to study proteins. However, one challenge to the method is that the amount of unnatural protein that can be

produced is directly limited by the amount of unnatural aminoacyl-tRNA presented to the cellular translation machinery. Therefore, the success of this technique depends heavily on the ability to deliver aminoacyl-tRNA, which is produced *in vitro*, into cells.

Currently, the most commonly used system involves injection of a *Xenopus* oocyte. It is desirable to transfer the technology to a mammalian expression system, but because mammalian cells are so much smaller than oocytes, injection is not a practical delivery method, so other techniques must be utilized. An intriguing possibility is the use of PTDs, small peptides that greatly enhance the internalization of extracellular material. Several PTD-based approaches for tRNA delivery were attempted: covalent ligation of tRNA to a PTD, noncovalent complexation of tRNA and PTDs, and production of a fusion protein containing a PTD and a tRNA-binding domain. However, none of these methods was useful in delivering tRNA into mammalian cells in culture.

Chapter three describes efforts to develop a high throughput assay for gating of the mechanosensitive channel of large conductance, MscL. The bacterial ion channel MscL is an ideal starting point for understanding the molecular basis of mechanosensation. However, current methods for the characterization of its mutants, patch clamp and bacterial growth analysis, are difficult and time consuming, so a higher throughput method for screening mutants is desired. We have attempted to develop a fluorescence assay for detecting MscL activity in synthetic vesicles. The assay involved the separation of two solutions—one inside and one outside the vesicles—that are separately nonfluorescent but fluorescent when mixed. It was hoped that MscL activity due to downshock of the vesicles would bring about mixing of the solutions, producing fluorescence. The development of the assay required the optimization of several

variables: the method for producing a uniform vesicle population containing MscL, the fluorescence system, and the lipid and protein composition of the vesicles. However, no MscL activity was ever detected even after optimization, so the assay was not fully developed. The probable cause of the failure was the inability of current techniques to produce a sufficiently uniform vesicle population.

Table of Contents

Acknowledgements	iii
Abstract	vi
Table of Contents	ix
List of Figures	xii
List of Tables	xiv
Chapter 1: Voltage-Dependent Hydration and Conduction Properties of the Hydrophobic Pore of the Mechanosensitive Channel of Small Conductance	1
Abstract	1
Introduction	2
Hydrophobic Nanopores	2
The Mechanosensitive Channel of Small Conductance	3
Previous Simulations of MscS	6
Results and Discussion	7
Water Occupancy of the Pore in Unperturbed MscS	7
Application of a Voltage to the Simulation System	11
Pore Water Occupancy with Higher Salt Concentrations	18
Spontaneous Conduction of Ions Through the Hydrated Channel	21
Diffusion Properties of Chloride Ions	26
Potential Profile of the Simulation System	29
Simulations with Different Water Models and Temperature-Coupling Groups	31
Structural Features of the Conducting Versus the Occluded States	31
Studies of Selected Mutant Channels	36
Investigation of the Mechanism for Voltage Modulation	39
Conclusion	41
Methods	43
Assembly of the Simulation System	43
Molecular Dynamics	44
Simulations with Mutant MscS	46
Data Analysis	47
Computers	51
References	51

Chapter 2: The Delivery of tRNA to Cultured Mammalian Cells Mediated by Peptide Transduction Domains	56
Abstract	56
Introduction	57
Unnatural Amino Acid Incorporation by Nonsense Suppression	57
Protein Transduction Domains	60
Results and Discussion	62
Covalent Ligation	62
Noncovalent Delivery Complexes	65
Preparation of Tat-eEF1A Fusion Protein	82
Conclusion	90
Materials and Methods	91
tRNA Generation	91
Thiophosphate Reaction with Maleimide	91
Noncovalent Complexation Experiments	92
Production of Tat-eEF1A Fusion Protein	96
References	102
Chapter 3: Efforts Toward a High Throughput Assay for Gating of the Mechanosensitive Channel of Large Conductance	107
Abstract	107
Introduction	108
The Mechanosensitive Channel of Large Conductance	108
Current Techniques for Studying MscL	111
Theoretical Descriptions of Downshocked Vesicles	114
Results and Discussion	119
Vesicle Preparation	119
Verifying the Presence of MscL in Extruded Vesicles	123
Evaluation of Fluorescence Systems	128
Optimization of Vesicle Composition—Lipid Composition	130
Optimization of Vesicle Composition—Protein Amount	136

Chapter 3 (continued)

Conclusion	138
Materials and Methods	140
Materials	140
Vesicle Preparation	141
Electron Microscopy	142
Immunogold Labeling	143
Serial Downshock Protocol	143
Data Analysis	144
References	145

List of Figures

Chapter 1

Figure 1.1. The MscS structure	5
Figure 1.2. Schematic of all wild-type simulations	8
Figure 1.3. Equilibration of wild-type simulations	8
Figure 1.4. Pore water occupancy in restrained simulations	9
Figure 1.5. Pore water occupancy in unrestrained simulations	10
Figure 1.6. Pore water occupancy of simulations in different computer environments	14
Figure 1.7. Alignment and interaction energy of water in the pore	16
Figure 1.8. Pore water occupancy in simulations with higher salt	19
Figure 1.9. Conduction and diffusion charge movements in wild-type simulations	22
Figure 1.10. Chloride densities in positive and negative fields	25
Figure 1.11. Electrostatic potential profiles of the channel with different fields	30
Figure 1.12. Pore water occupancy and conduction and diffusion charge movements for control simulations	32
Figure 1.13. Channel profiles	33
Figure 1.14. Movement of TM3 helices	34
Figure 1.15. Radial distribution functions for chloride ions in the pore and in the bulk water	35
Figure 1.16. Pore water occupancy in mutant simulations	37
Figure 1.17. Conduction charge movements in mutant simulations	38
Figure 1.18. Positions of TM1 and TM2 in wild-type and mutant simulations	40

Chapter 2

Figure 2.1. The nonsense suppression method for unnatural amino acid incorporation	58
Figure 2.2. Fluorescence spectra for the detection of the reaction of various thiol and thiophosphates with a maleimide	64
Figure 2.3. HPLC and MS analysis of MPG prepared by solid-phase synthesis	66
Figure 2.4. Fluorescence quenching of MPG by complexation with plasmid DNA	67
Figure 2.5. Small-well containers used for cell culture	68
Figure 2.6. Cell growth in small-well containers	69
Figure 2.7. Fluorescence images of cells after application of MPG and wt-EGFP DNA	72
Figure 2.8. Transfection efficiency for Epizap and PolyFect Transfection Reagent	74
Figure 2.9. Optimization of the amount of PolyFect Transfection Reagent	75
Figure 2.10. Optimization of the amount of DNA to use with PolyFect Transfection Reagent	76
Figure 2.11. The HSAS assay for tRNA delivery	77
Figure 2.12. Fluorescence images of cells after application of MPG and HSAS with apparently successful delivery	79
Figure 2.13. Fluorescence images of cells after application of MPG and HSAS, with apparently failed delivery	80
Figure 2.14. Fluorescence images of cells after application of Antp and HSAS	82

Chapter 2 (continued)

Figure 2.15. Schematic of the delivery of tRNA using Tat-eEF1A	83
Figure 2.16. SDS-PAGE gel of protein harvested at different stages in the inclusion body purification	85
Figure 2.17. SDS-PAGE gel of retentates and filtrates after the concentration of Tat-eEF1A in different refolding buffers	87
Figure 2.18. Native PAGE gel of mixtures of Tat-eEF1A and tRNA	89

Chapter 3

Figure 3.1. Mechanosensation by MscL	109
Figure 3.2. The MscL structure	110
Figure 3.3. Schematic of the proposed assay	113
Figure 3.4. Schematic of the models for vesicles experiencing downshock	115
Figure 3.5. Size distributions of extruded vesicles	122
Figure 3.6. Western blot of vesicles prepared with and without MscL	124
Figure 3.7. Immunogold labeling of vesicles prepared with and without MscL	126
Figure 3.8. Freeze-fracture electron microscopy of vesicles prepared with MscL	127
Figure 3.9. Fraction of released osmolytes versus applied downshock for lipid mixtures with different melting temperatures	132
Figure 3.10. Fraction of released osmolytes versus applied downshock for lipid mixtures containing cholesterol	134
Figure 3.11. Fraction of released osmolytes versus applied downshock for vesicles with different amounts of protein	137

List of Tables

Chapter 1

Table 1.1. Conduction and diffusion current data in wild-type simulations	23
Table 1.2. Conduction current data in mutant simulations	38

Chapter 2

Table 2.1. Primary sequences of selected protein transduction domains	61
---	----

Chapter 3

Table 3.1. Acronyms, names, and chemical groups of lipids	119
Table 3.2. Melting temperatures of lipids and lipid mixtures	131
Table 3.3. Analysis of serial downshock experiments on vesicles with various lipid compositions	133
Table 3.4. Analysis of serial downshock experiments on vesicles with various amounts of protein	137

Chapter 1

Voltage-Dependent Hydration and Conduction Properties of the Hydrophobic Pore of the Mechanosensitive Channel of Small Conductance

Abstract

A detailed picture of water and ion properties in small pores is important for understanding the behavior of biological ion channels. Several recent modeling studies have shown that small, hydrophobic pores exclude water and ions even if they are physically large enough to accommodate them, a mechanism called hydrophobic gating. This mechanism has been implicated in the gating of several channels, including the mechanosensitive channel of small conductance, MscS. Although the pore in the crystal structure of MscS is wide and was initially hypothesized to be open, it is lined by hydrophobic residues and may represent a nonconducting state. Molecular dynamics simulations were performed on MscS to determine whether or not the structure can conduct ions. Unlike previous simulations of hydrophobic nanopores, electric fields were applied to this system to model the transmembrane potential, which proved to be important. Although simulations without a potential resulted in a dehydrated, occluded pore, the application of a potential increased the hydration of the pore and resulted in current flow through the channel. The calculated channel conductance was in good agreement with experiment. Therefore, it is likely that the MscS crystal structure is closer to a conducting than to a nonconducting state.

INTRODUCTION

Hydrophobic Nanopores

Biological ion channels play an essential role in cell survival by providing superb control over the molecules and ions they allow to enter and leave [1]. On a very simplistic level, these channels exist in two states, an impermeable closed state and a permeable open state. A stimulus, such as ligand binding or a change in the electrical or osmotic environment of the cell, can induce a transition from a closed resting state to an open state that allows passage of a particular set of ions or molecules. An essential part of this gating process is the formation of a pore through the membrane, such that the barrier to ion passage is greatly reduced compared to that of the impermeable lipid bilayer.

The requirement for a low barrier demands the presence of water or similar coordinating groups in an ion channel pore. The selectivity filter of potassium channels, for example, is lined by backbone carbonyls that mimic the coordination of an aqueous potassium ion [2]. In contrast, less selective channels such as the nicotinic acetylcholine receptor [1], the mechanosensitive channels of large and small conductance [3, 4], and α -hemolysin [5] are thought to have open states with wider pores that support hydrated ions.

The properties of water in these small pores are very important in understanding ion channel function. The microscopic properties of water are not fully understood, and it is well established that water in narrow spaces such as might be seen in the pore of an ion channel (on the order of a few molecules across) does not necessarily have the same properties as bulk water [6]. For example, molecular dynamics (MD) studies by

Beckstein and Sansom have established the surprising result that a hydrophobic pore is not necessarily filled with water, even if it is large enough to fit several water molecules [7–9]. Below a threshold radius, dependent on the hydrophobicity of the pore, water is essentially absent from a model pore even if there is space for it, producing a kind of “hydrophobic gate.” For a purely hydrophobic model pore, the threshold radius is ~ 4.5 Å, large enough to accommodate three water molecules [7], and the threshold for ion occupancy of the pore is even larger (~ 6.5 Å) [9]. MD simulations of the hydrophobic pores of more realistic systems showed a similar threshold behavior, although the threshold radius varied from that in the simple model. For example, the threshold radii for the pores of the nicotinic acetylcholine receptor and a carbon nanotube were found to be ~ 4.0 and ~ 2.5 Å, respectively [10, 11], and were quite sensitive to the parameterization of the interaction between the water and the pore wall, at least in the nanotube system [12].

The Mechanosensitive Channel of Small Conductance

As part of a general program investigating bacterial ion channels, we have been studying the bacterial mechanosensitive channel of small conductance (MscS). This channel is gated by membrane tension, and it is thought that MscS functions as a “release valve” for the rapid efflux of osmolytes under conditions of osmotic stress [13, 14]. In addition, MscS is modulated by voltage and displays a slight anion preference for conduction [4]. Despite its name, the channel shows a relatively large conductance of ~ 1.0 nS, consistent with the proposed function.

MscS is an interesting molecule for study for several reasons. First, as a prokaryotic mechanosensitive channel, MscS is an important model system for mechanosensation in higher organisms. In general, mechanosensitive channels have been implicated in the sensation of many different stimuli, such as touch and hearing [15]. Specifically, MscS homologues have been discovered in many kinds of organisms, even fungi and plants [16, 17], but their roles in higher organisms are only beginning to be elucidated [18]. Second, MscS is modulated by voltage [14, 19]. Voltage sensation is an important feature of many ion channels, but precise details of the mechanism remain largely unknown [20]. Last, MscS is one of only a handful of ion channels that have known crystal structures [21, 22], providing unique opportunities for structure-function studies.

The crystal structure of *E. coli* MscS has been reported by Rees and co-workers [23]. The protein is a homoheptamer of multidomain subunits of 286 amino acids in length (fig. 1.1A). From N- to C-terminus, the domain organization is as follows: a transmembrane (TM) domain comprised of three transmembrane helices, a middle- β domain that consists primarily of β -sheet, and a C-terminal α/β -domain (fig. 1.1B). There are vestibules on either side of the pore: the periplasmic vestibule, lined by the N-terminal halves of TM3, and the cytoplasmic vestibule, surrounded by the middle- β and C-terminal domains. The narrowest constriction, which shall hereafter be called the pore, is the region around two hydrophobic residues, L105 and L109 of TM3, near the cytoplasmic side of the bilayer. At its narrowest point, MscS displays a pore radius of ~ 3.5 Å. Because the pore is physically wide enough for the passage of water and ions, it was initially hypothesized that the crystal structure is a model of the open state of the

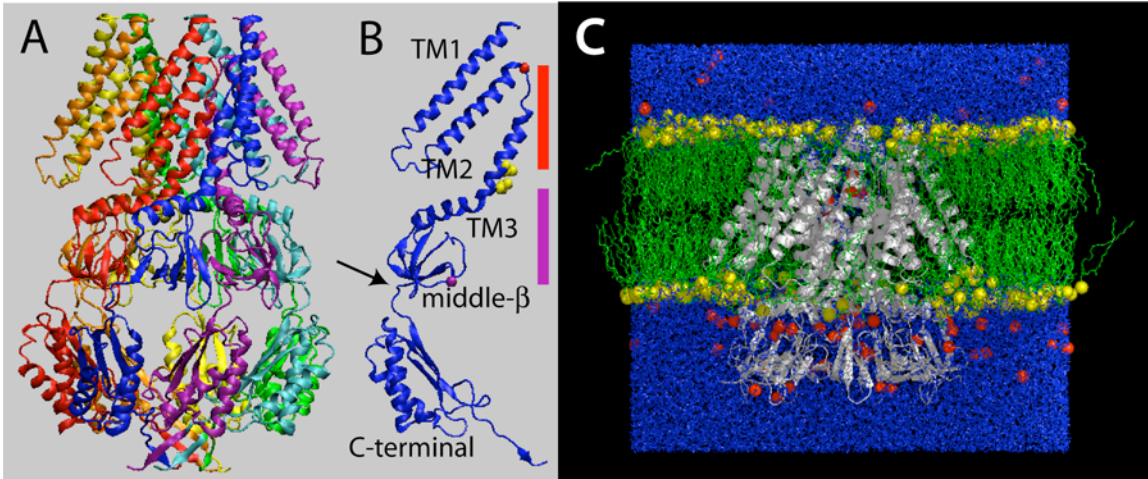


Fig. 1.1. *A*, Side view of the MscS homoheptamer, colored by subunit. *B*, An individual subunit with domains labeled. Yellow: sidechains of pore-lining L105 and L109; Red sphere: C α of V91, the upper boundary of the periplasmic vestibule; Purple sphere: C α of G140, the lower boundary of the cytoplasmic vestibule in the truncated MscS model. The red and purple boxes mark the approximate regions of the periplasmic and cytoplasmic vestibules, respectively. The arrow marks the end of the middle- β domain, the terminus of the simulated protein. *C*, The periodic box of the MD simulation system, showing the protein (white), phospholipid chains (green), phospholipid headgroups (yellow), water molecules (blue), and ions (red).

channel [23]. However, as noted above, 3.5 Å is slightly lower than the threshold radius for a hydrophobic gate determined by Beckstein and Sansom [7], suggesting that the structure is nonconducting.

Because of the usefulness of MscS as a model for mechanosensation and voltage modulation, an important question is whether the image of MscS produced by crystallography represents an open, conducting state of the channel or a nonconducting state. As we had done with the mechanosensitive channel of large conductance [24, 25], we turned to full-scale MD simulations of MscS to illuminate this problem. The simulation system, consisting of MscS surrounded by explicit lipid, water, and ions, is shown in fig. 1.1C.

Previous Simulations of MscS

While our efforts were in progress, two other MD simulations of MscS appeared. The first of these, reported by Anishkin and Sukharev, involved a somewhat simplified model that included only the channel-lining regions of the protein, harmonically restrained, and an octane slab to model the lipid [26]. They found that the pore was generally empty of water, and even when the pore was occupied, there was rarely more than a single file of water molecules. Furthermore, when a chloride ion was forced through the mostly dehydrated pore, it experienced a large barrier to conduction. Anishkin and Sukharev concluded that, because the relatively large conductance of MscS demands a much lower barrier than that observed in their simulations, the crystal structure is a nonconducting state with a hydrophobic gate.

Sotomayor and Schulten reported much larger-scale simulations of MscS involving full-length protein with an explicit lipid bilayer [27]. Like Anishkin and Sukharev, they found that simulations with a substantially restrained protein backbone produced a dehydrated pore region. Relaxing the restraints caused the protein to collapse, producing an occluded pore that is certainly nonconducting. However, when a large tension was applied to the system, the collapse was avoided, and a system with a substantially hydrated pore emerged.

Here we present the results of our MD simulations of MscS that were intended to shed light on whether or not the crystal structure is conducting or nonconducting, as well as provide further insights on the nature of hydrophobic pores. Our approach more nearly parallels that of Sotomayor and Schulten [27], in that we simulate nearly the entire protein in an explicit bilayer (fig. 1.1C). An informative addition in the present

simulations is an evaluation of the effect of an applied voltage on the MscS system. We find that an applied voltage can profoundly influence the hydration of the channel, whether in a restrained or unrestrained simulation. In addition, we find that an applied voltage can favor a hydrated state of the channel that, even during these relatively short simulation times, conducts a significant number of chloride ions. These results suggest that the image of MscS obtained from crystallography is likely more similar to an open, conducting state than to a nonconducting state.

RESULTS AND DISCUSSION

A large number of MD simulations of MscS were performed in a variety of conditions. Fig. 1.2 summarizes the simulations, indicating for each the salt content, presence or absence of restraints, initial pore state, and start and end times. The stabilization of the RMS deviations (RMSDs) of the protein from the crystal structure and the total system energies indicates that the simulations rapidly (< 2 ns) attained a steady state, as expected (fig. 1.3).

Water Occupancy of the Pore in Unperturbed MscS

The initial simulations (R^h0 ; R indicating a restrained protein backbone; h indicating an initially hydrated pore; 0 indicating zero applied voltage) included soft harmonic position restraints on all protein backbone atoms, using the same restraining force constant [418.4 kJ/(mol nm²)] as in previous studies [26, 27]. Even though the pore of the restrained system was initially hydrated, it emptied of water rapidly (in ~ 0.5 ns). The pore occasionally filled with water for periods of 200 or 300 ps, but for most of the

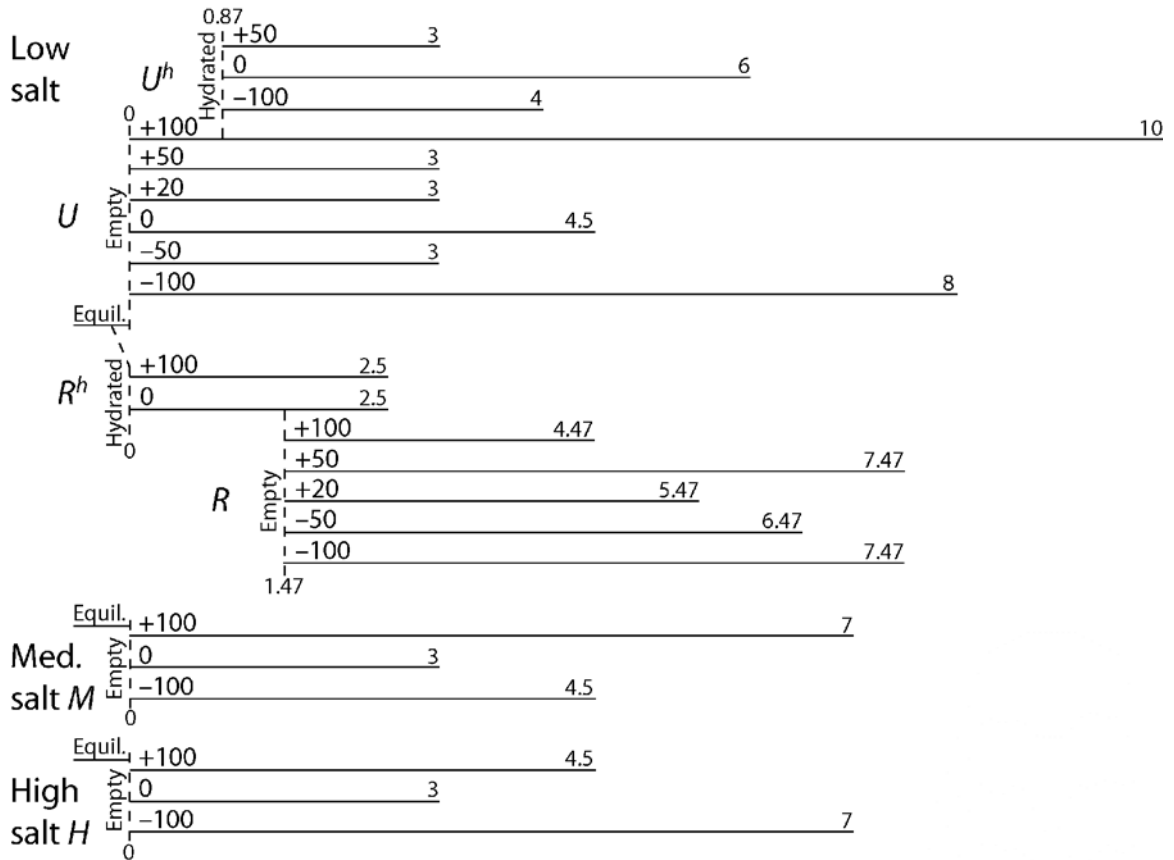


Fig. 1.2. Schematic of all wild-type simulations, indicating their salt content, initial hydration state (R^h , U^h : hydrated; R , U , M , H : empty), presence of restraints (R : restrained; U , M , H : unrestrained), applied electric field (in mV/nm), and start and end times (in ns).

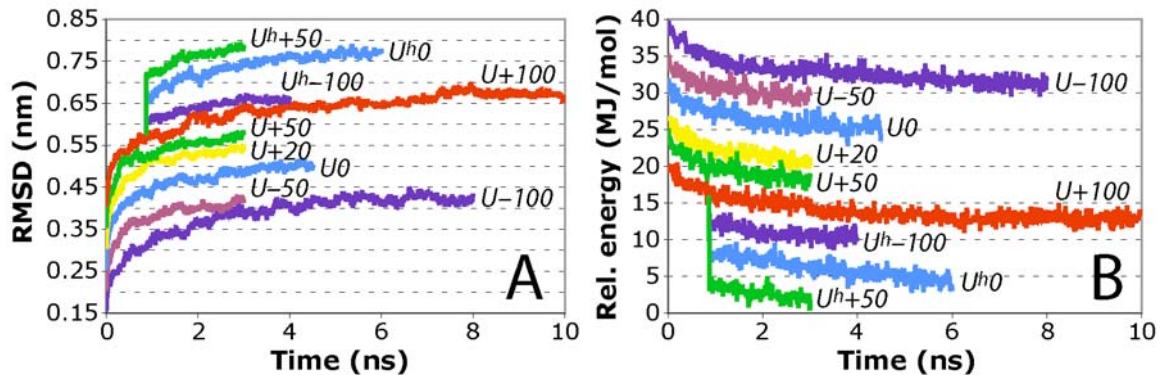


Fig. 1.3. Equilibration of wild-type simulations. RMS deviations (RMSDs) (A) and total energies (B) are shown as a function of time. For clarity, the RMSDs of the different simulations are offset in steps of 0.05 nm, and the energies are offset in steps of 4 MJ/mol. Most simulations have reached a steady state by ~ 2 ns.

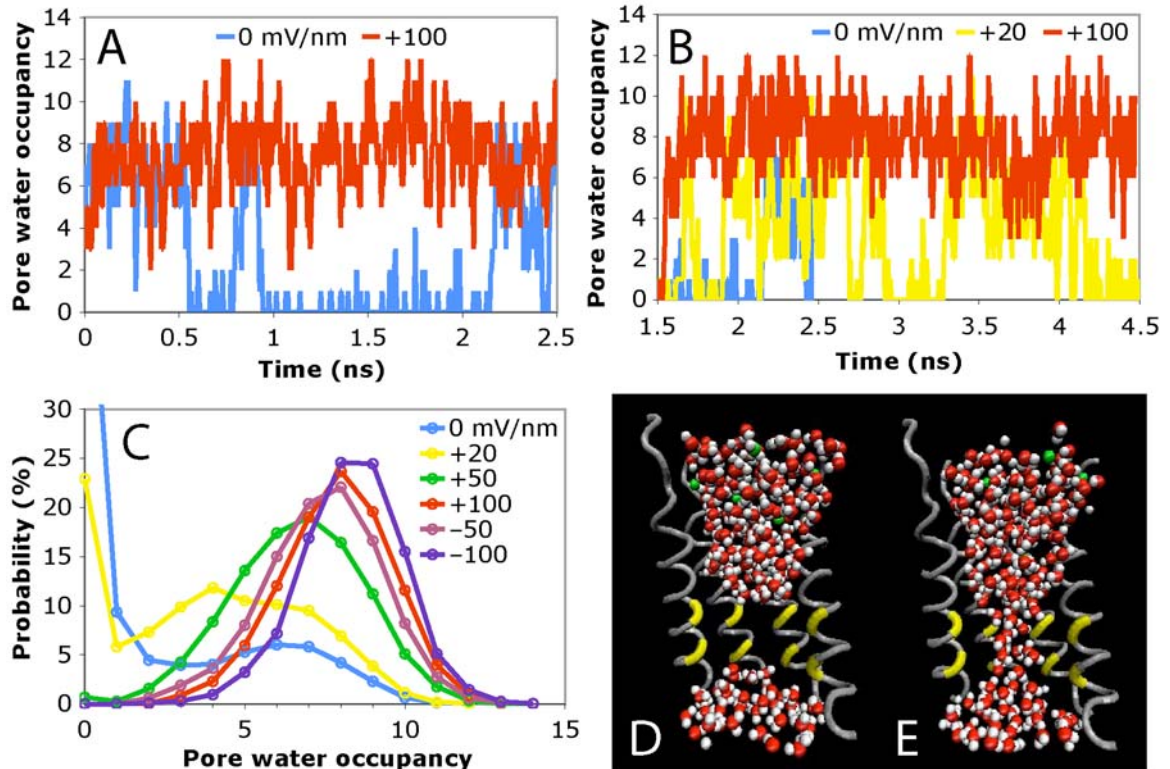


Fig. 1.4. *A–B*, The water occupancy of the pore as a function of time in R^h (*A*) and R (*B*) simulations with various electric fields. For clarity, $R+50$, $R-50$, and $R-100$ are not included in *B*. They have water behavior very similar to $R+100$ (red). *C*, Probability distributions of water occupancy in R and R^h for various electric fields. *D–E*, Snapshots of the pore viewed from the side in a dehydrated (*D*) and fully hydrated (*E*) state. The gray helices are the N-terminal halves of the TM3 helices, which line the channel. For clarity, only four of the seven helices are shown. The locations of the pore-lining leucines are shown in yellow. Water molecules (red and white) and chloride ions (green) are shown as spheres.

simulation, it was completely empty (fig. 1.4A, blue trace). The water was separated by the hydrophobic region into two distinct reservoirs (fig. 1.4D). These results are consistent with previous simulations of hydrophobic nanopores, because the size of the MscS pore is smaller than the threshold for hydration [7, 8].

Removing the restraining force did not change the hydration behavior of the system. Whether the initial state was empty ($U0$; U indicating an unrestrained protein backbone) or hydrated (U^h0), the pore quickly evolved into a dehydrated state

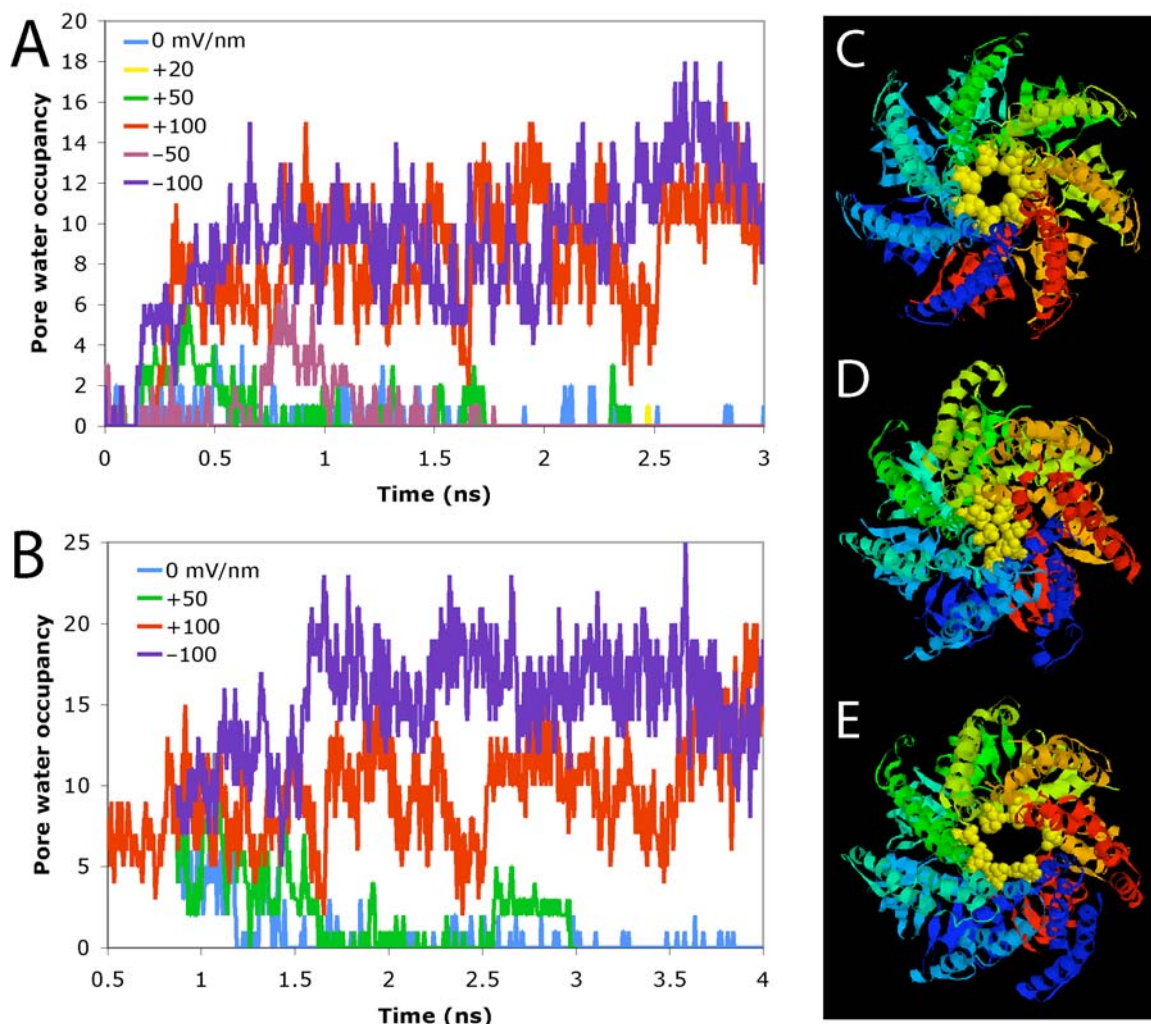


Fig. 1.5. *A–B*, The water occupancy of the pore as a function of time in *U* (*A*) and U^h (*B*) simulations with different electric fields. *C–E*, Snapshots of the pore viewed from the periplasm. *C* shows the crystal structure, and *D* and *E* show frames from the end of $U0$ and $U+100$, respectively. The protein is colored by subunit, except L105 and L109, which are in yellow spacefilling.

(fig. 1.5A–B, blue traces). Because the dehydration effectively produced a local vacuum (fig. 1.4D) and there were no restraints on the protein, the pore rapidly collapsed. In clear contrast to the crystal structure, which contains a wide pore (fig. 1.5C), this collapsed structure displayed an essentially complete occlusion of the channel, formed by L105 and L109 of TM3 (fig. 1.5D). It is certain that such a structure represents a closed, nonconducting form of the channel. These results completely parallel those of

Sotomayor and Schulten, who also considered an explicit bilayer and a fairly complete model of the protein [27]. Given that the present work employs a different force field and simulation package from that of Sotomayor and Schulten, the similarities are gratifying and enhance the confidence in the overall behavior of the system.

Application of a Voltage to the Simulation System

As noted above, along with being responsive to changes in membrane tension, the behavior of MscS is significantly perturbed by alterations in transmembrane voltage [14]. Given the intense interest in the molecular mechanism of voltage sensing in ion channels in general and Kv channels in particular [20, 22, 28–31], we found this to be one of the most attractive features of the MscS channel. We, and others, were especially intrigued by the presence of a number of arginine residues in the transmembrane domain of MscS [23]. Arginine residues play a critical role in voltage sensing in the Kv channels, and we have sought, both experimentally and computationally, to probe their role in MscS. Of course, in its natural environment MscS is always exposed to a significant transmembrane voltage. In fact, bacterial transmembrane potentials are unusually high, perhaps in the range of -120 to -160 mV, or more [32]. Also, all experimental studies of MscS using the patch-clamp methodology require a transmembrane potential to see conduction.

We began by subjecting the system with harmonic restraints to an applied electric field of $+100$ mV/nm. The sign convention is such that a negative electric field produces a bias that is in the same direction as a natural transmembrane potential; the inside of the cell is negative relative to the outside. Therefore, with this field, our simulation

represents a depolarized membrane. Under these conditions with an initially hydrated pore (R^h+100), the pore remained hydrated for the entirety of the simulation (fig. 1.4A, red trace). There was a continuous column of water molecules throughout the pore region (fig. 1.4E). In addition, the initially empty pore of $R+100$ became hydrated very rapidly (~ 0.1 ns) (fig. 1.4B, red trace). Again, the observation of the same steady-state behavior with different initial conditions indicates the robustness of the result. Thus, the application of a voltage to the system has qualitatively altered the behavior of the channel.

The $+100$ mV/nm field is relatively large. We therefore considered smaller potentials and the consequence of reversing the field. As we saw in $R+100$, the presence of other moderate or high electric fields (± 50 or -100 mV/nm) allowed rapid filling to create a hydrated pore, and the pore remained hydrated for essentially the entire length of the simulations. For a more modest field of $+20$ mV/nm, the pore displayed more frequent dewetting events, but we still observed increased hydration compared to simulations with no field (fig. 1.4B). Thus, an extraordinarily high field is not required to see qualitatively different wetting behaviors from the restrained simulations of Anishkin and Sukharev [26] or Sotomayor and Schulten [27]. The hydrophobic gate of MscS seen in previous simulations is absent in the presence of a potential.

The probability distribution for water in the pore for each of the six electric fields clearly indicates a field dependence on the amount of water hydrating the pore in the restrained simulations (fig. 1.4C). Without a field, there is very little water in the pore, but as the magnitude of the field increases the pore is more likely to be hydrated. Electric field effects on the threshold radii for model hydrophobic gates have not yet been studied,

but the data here strongly suggest that increasing the electric field reduces the threshold radius.

We next considered the effects of an applied voltage on the unrestrained system. Simulations with electric fields of ± 100 mV/nm ($U\pm 100$) displayed qualitatively similar water behavior to $R\pm 100$, with one important difference. When beginning from a dehydrated pore, the unrestrained simulations revealed a competition between water and the pore-lining leucines to fill the vacuum in the pore. The inherently chaotic behavior of MD was especially evident here, in that subtle differences in the simulations led to two distinct pore states. The $U+100$ and $U-100$ simulations were each performed several times, on different computer environments (fig. 1.6A–D). In some simulations, inward collapse of the leucines resulted in an occluded pore (like that seen in $U0$, fig. 1.5D) that contained no water. However, in other simulations, water entered the pore first and formed a stably hydrated state. Clearly, the pore state is very sensitive to the initial conditions of the simulations. Similar chaotic behavior involving the competition between the water and the leucines was seen in other simulations, discussed below. However, it is notable that once a certain threshold of hydration was attained by the pore (~ 5 water molecules), the channel remained fully hydrated throughout the simulation (fig. 1.6A–D; the red and purple traces in fig. 1.5A–B are representative examples of the simulations that contained stably hydrated pores).

In the simulations with a stably hydrated pore ($U+100$, $U-100$, U^h-100), the water prevented the collapse of the pore-lining leucines and maintained a pore approximately the same size as that of the crystal structure (fig. 1.5E). Because there were no restraints on the protein conformation, the pore was free to widen slightly and

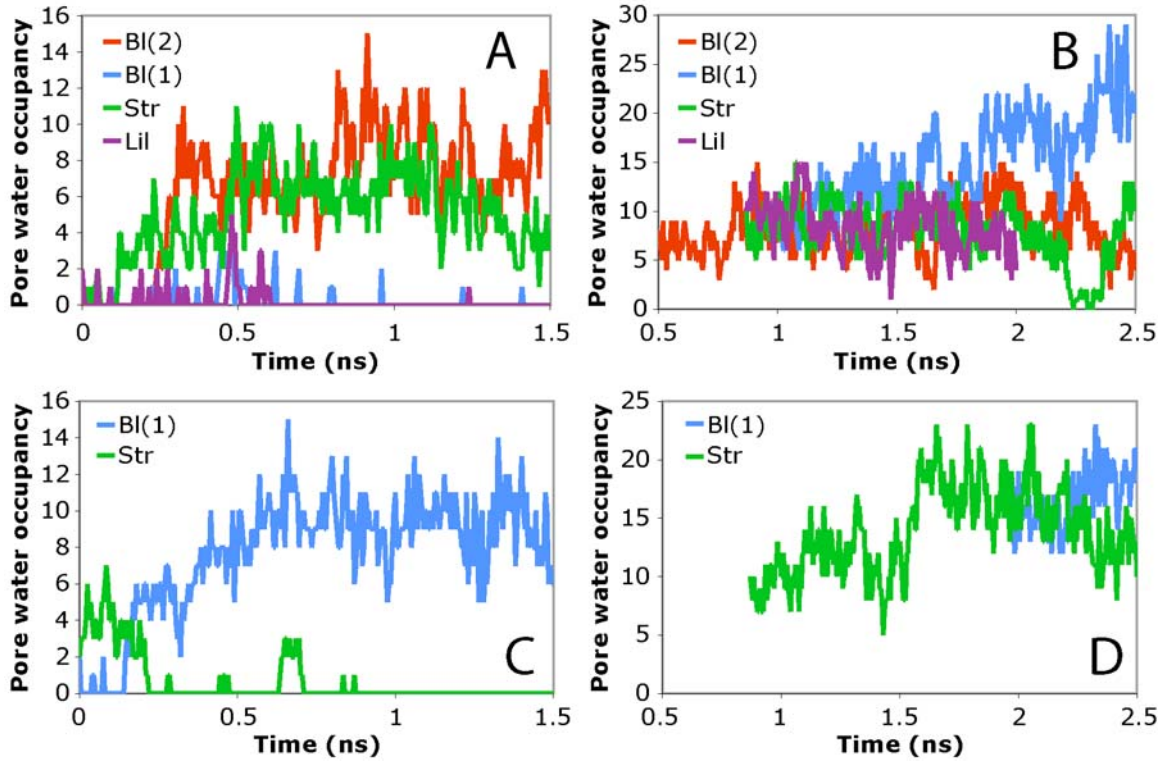


Fig. 1.6. Pore hydration of simulations from different computer environments. The data in each graph are from simulations with identical input parameters; only the computer environments differed. All simulations are unrestrained with an electric field of $+100$ (A–B) or -100 mV/nm (C–D). The pore was initially empty in A and C and hydrated in B and D. The computer environments used were as follows:
 Bl(2): Blackrider using two processors; Bl(1): Blackrider using one processor;
 Str: Strongbad using one processor; Lil: Liligor using one processor. Bl(2) in A was selected as the representative simulation U_{+100} , Bl(1) in C as U_{-100} , and Bl(1) in D as U^h_{-100} .

accommodate more water molecules than were present in the restrained simulations. As in the restrained simulations, a large potential stabilized a hydrated pore, further suggesting that MscS does not have a hydrophobic gate in a high electric field. Again, the results here are analogous to the work of Sotomayor and Schulten, who demonstrated that membrane tension, like the transmembrane potential in our simulation, is sufficient to maintain a wide, hydrated MscS pore [27]. It should be mentioned that voltage and tension affect MscS in different ways. Tension is the primary stimulus for activation, but

recent electrophysiological results indicated that voltage modulates its deactivation [19]. However, it is interesting that both tension and voltage are separately sufficient to maintain the pore state of the crystal structure.

However, a notable difference between the restrained and unrestrained simulations was observed with applied fields of lower magnitudes (+50 to -50 mV/nm). Field-dependent hydration of the pore was not observed in these unrestrained simulations. Instead, with lower fields, the system quickly evolved into the dehydrated, collapsed state, regardless of whether the pore was initially empty or hydrated (fig. 1.5A-B).

The fact that the hydration state of the pore is dependent on its flexibility, as observed in our simulations with +20 or ± 50 mV/nm fields, is in agreement with recent work by Beckstein and Sansom that showed a general inverse relationship between the flexibility of a hydrophobic pore and the probability of water occupancy [9]. They attributed this phenomenon to a decrease in the depth of the attractive well of the van der Waals potential of a water molecule interacting with the fluctuating walls. The results here suggest that in moderate electric fields, the shallower wells destabilize the water to the point that the field energy is no longer sufficient to maintain a hydrated pore. However, large fields of ± 100 mV/nm maintain a hydrated MscS pore even with no restraints at all.

We hypothesized that the mechanism by which a large field contributes to pore hydration involves the field-induced alignment of water dipoles in the pore. Snapshots of water in the pore clearly showed a field-dependent alignment (fig. 1.7A-C). We quantified this by plotting the alignment of the water ($\langle \cos \theta \rangle$, where θ is the angle between the water dipole and the z -axis) as a function of position in the periodic box for

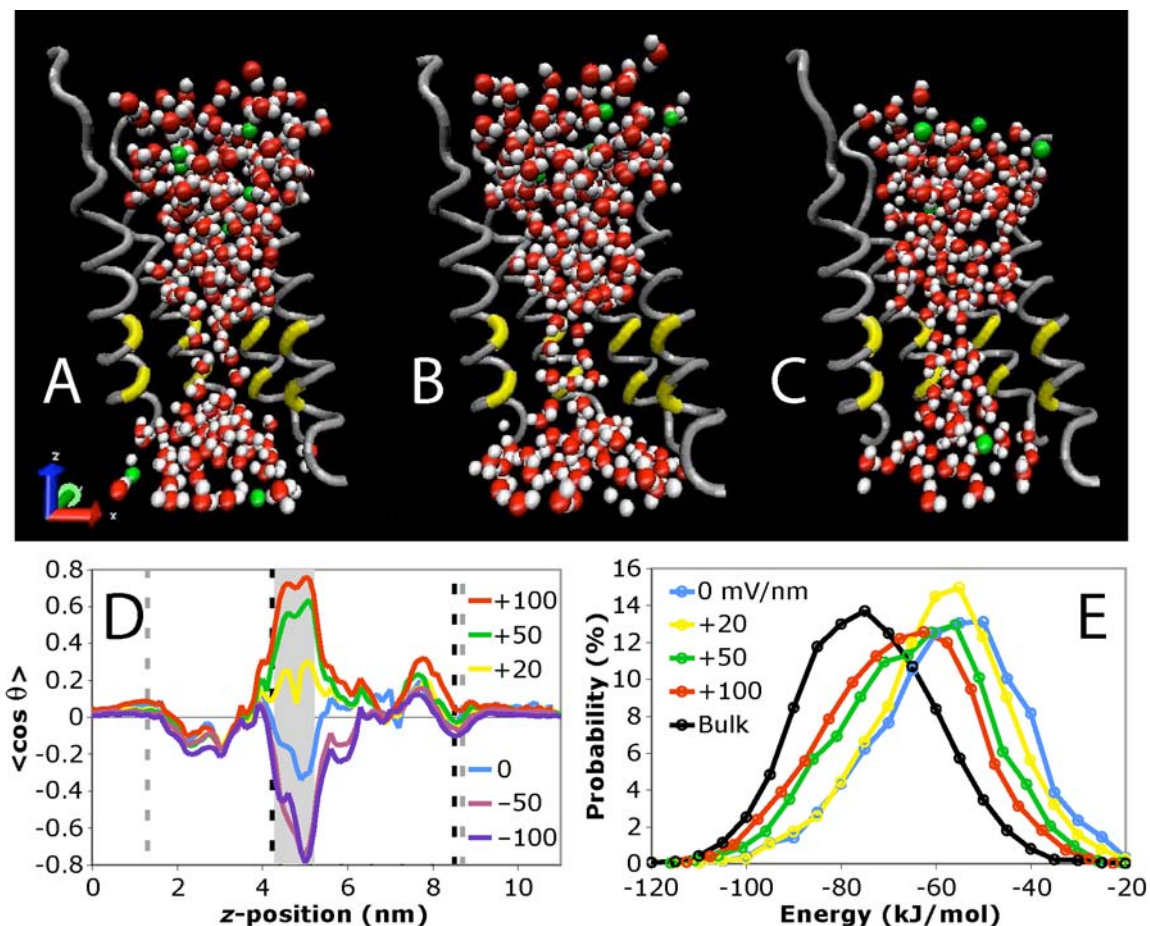


Fig. 1.7. A–C, Snapshots of the pore viewed from the side in $R+100$ (A), $R0$ (B), and $R-100$ (C), indicating the high degree of water alignment. The coloring is described in fig. 1.3D–E. The system axes are shown on the left. D, Net alignment of water dipoles as a function of position within the simulation system for various electric fields. To minimize the influence of water molecules that have a z value corresponding to the pore region but that are in fact embedded in the membrane, only water molecules that occupied the pore at some point in the simulation are considered. Important regions are marked as follows: Light gray vertical stripe: pore region; black dashed vertical stripes: the limits of the bilayer; gray dashed vertical stripes: the limits of the protein. E, Probability distributions of interaction energies of water molecules in the bulk and pore regions under the application of various electric fields. Dipole-field interactions are included in the energies. All data are from R and R^h simulations.

the R simulations (fig. 1.7D). In the regions near the edge of the box, in which the environment is most similar to bulk water, the water shows only a slight orientational preference, which is independent of the applied field. The fact that there is no field-dependence to the alignment is not surprising, because the dipole orientation energy of an

individual water molecule in even the largest electric field is only one-sixth of kT . The small nonzero net dipole in these regions is likely an artifact of the periodic boundary conditions, as recently reported [33]. The large dipoles of MscS and its infinite images lead to ordering of the water structure even in the bulk regions. In other regions of the simulation system, local interactions between polar groups in the protein and bilayer tend to orient the water in a field-independent manner.

The pore region, however, is unique in that there is a large field dependence on the alignment of the water. The alignment of the water correlates reasonably well with the water occupancy of the pore, with the 0 and +20 mV/nm fields showing a relatively poor alignment compared to the ± 50 and ± 100 mV/nm fields. In the ± 100 mV/nm fields, the absolute values of $\langle \cos \theta \rangle$ approach 0.8, a very high degree of alignment.

The observation of water alignment in stronger fields provides an explanation for the influence of an external field on pore hydration. In a hydrophobic pore, a water molecule oriented with its dipole parallel to the pore interacts through hydrogen bonds with the water molecules above and below it. Rotation of this dipole toward the wall of the pore is unfavorable, because the weak interaction between the water and the hydrophobic wall does not compensate for the energy lost from the weakened hydrogen bonds with the waters above and below.

The enthalpic gain from hydrogen bonding in forming a water column in a hydrophobic pore comes with an entropic penalty for forming such an ordered structure. In the present system, the enthalpy of the hydrogen bonding alone is insufficient to overcome this cost, as evidenced by the fact that in the absence of an electric field, a hydrated pore occurs only rarely. However, an electric field provides further stability for

the water column, in that the orientation energy of the several aligned water dipoles contributes favorably to the enthalpy, and the overall energy is lowered in a field-dependent manner. This can clearly be seen by comparing the interaction energy distributions for water in the pore in the various electric fields (fig. 1.7E). The energy distributions from the different fields form approximately Gaussian curves, all with about the same width. However, with an increasing field (and increasing alignment), the midpoints of these distributions are shifted toward lower energies, and the interaction energies approach those for bulk water. For an individual molecule, the dipole orientation energy is small, as mentioned earlier, but for several molecules, the energy becomes more significant. In this way, a hydrated pore is preferentially stabilized by larger electric fields.

The degree of alignment of the water with no applied electric field gives a sense of the strength of the electric field inherent to the protein itself. The pore is lined by seven α -helices, all with their helical dipoles pointing generally in the $+z$ direction. Dipole-dipole interactions favor an arrangement of water oriented with its dipole in the $-z$ direction, exactly as observed in our simulations. This may be why, in the *R* simulations, the -50 and -100 mV/nm fields had slightly greater hydration than the $+50$ and $+100$ mV/nm fields, respectively (fig. 1.4C).

Pore Water Occupancy with Higher Salt Concentrations

Unrestrained simulations with higher salt concentrations (200 and 300 mM instead of 100 mM; designated as *M* and *H*, for medium and high salt) and fields of $+100$, 0 , and -100 mV/nm were also performed and compared to the low-salt (*U*) simulations.

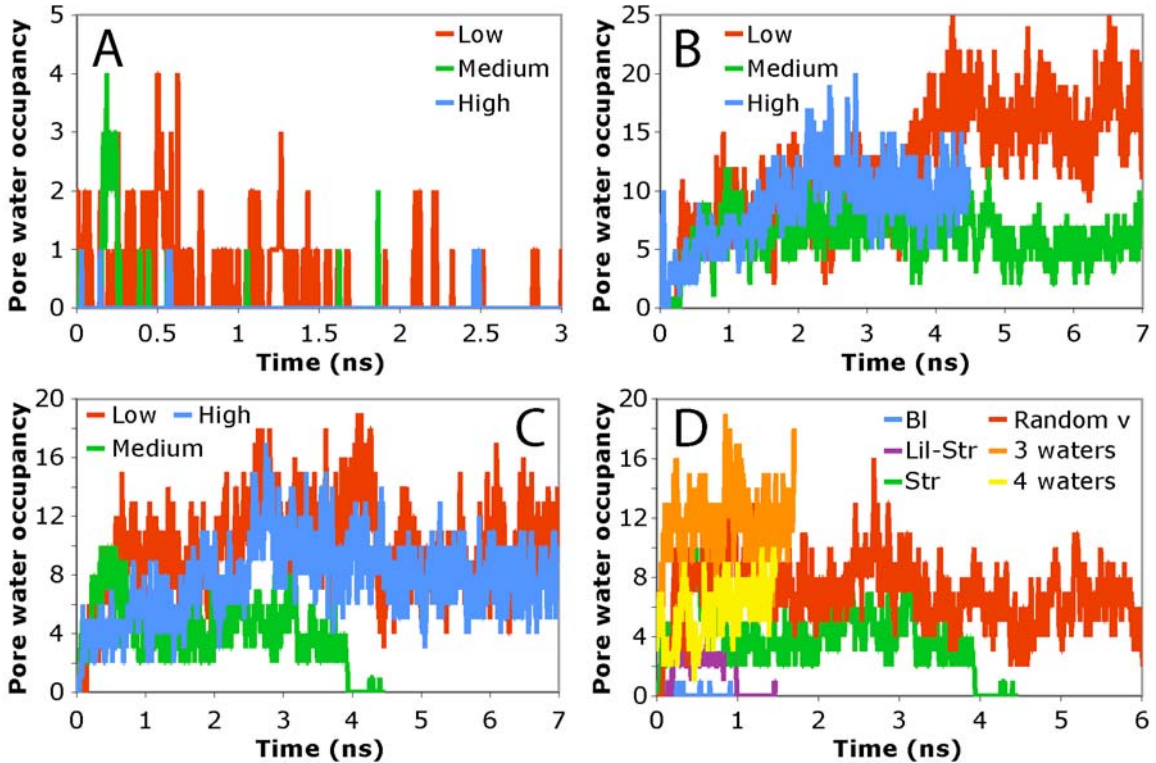


Fig. 1.8. A–C, The water occupancy of the pore as a function of time for simulations with fields of 0 (A), +100 (B), and –100 mV/nm (C). D, Pore water occupancy for $M-100$ simulations in different conditions. The first three represent “continuation simulations” with identical input parameters on different computer systems (Bl: Blackrider; Lil-Str: started on Liligor, but later transferred to Strongbad; Str: Strongbad). The last three represent “altered simulations” with slightly altered initial arrangements. In Random v, the velocities of all the atoms were randomized at the beginning of the simulation. In 3 waters and 4 waters, three or four water molecules were manually inserted into the pore at the beginning of the simulation.

For the most part, the salt concentration did not significantly affect the water occupancy of the pore. In $M0$ and $H0$, the pore remained in a dehydrated state and quickly became occluded by the pore-lining leucines, just as it did in $U0$ (fig. 1.8A). Also, in $H\pm 100$, as in $U\pm 100$, the pore remained hydrated for essentially the full length of the simulations (fig. 1.8B–C). However, the results of the $M\pm 100$ were slightly different from expected. Although the pore remained stably hydrated throughout $M+100$, there was generally less water in the pore than in $U+100$ or $H+100$ (fig. 1.8B–C). Even more unusual, the pore in $M-100$ emptied of water and became occluded after it had been substantially hydrated,

which contrasted with $U\pm 100$, $H\pm 100$, and $M+100$. In these simulations, when the pores attained a threshold level of hydration (~ 5 waters), they remained fully hydrated throughout the simulation.

Therefore, the $M-100$ results were explored more fully by observing the pore water occupancy in simulations with slightly different conditions. Three “continuation simulations,” which began with identical atom positions and velocities, were performed on different computer systems. Also, three “altered simulations” were performed. For two of these, three or four waters were added to the pore at the beginning of the simulations. For the third, the atom velocities at the beginning of the simulation were randomized. The velocities still reflected a system temperature of 310 K, like the other simulations, but different velocities were assigned to each atom.

As seen in $U\pm 100$, the continuation simulations displayed chaotic behavior involving the competition between the water and the pore-lining leucines to fill the evacuated pore (fig. 1.8D). In two continuation simulations, a hydrated pore was never attained before occlusion occurred. In the third continuation simulation, a hydrated pore emerged but eventually dehydrated, which, as mentioned earlier, was unexpected. However, the water in the altered simulations, in which the initial state of the system was slightly different, behaved like it had in previous simulations. In all three, the pore filled with water and remained hydrated for the full length of the simulations (fig. 1.8D). The emptying of the hydrated pore in $M-100$ was not consistently observed, suggesting that the one case where it occurred was anomalous. Therefore, the simulations with medium and high salt strengthened the idea suggested by the low-salt simulations that a field of ± 100 mV/nm is sufficient to stably hydrate the MscS pore.

A possible explanation for the unexpected results from the M simulations is that concentrated salt solutions have an increased surface tension, thereby preferentially stabilizing the liquid-vacuum interface of the dehydrated pore. This explanation was invoked by Anishkin and Sukharev for their observation that the pore water occupancy in their simulations was somewhat lower in 150 mM NaCl solution than in pure water [26]. This is consistent with the relationship between the M and U simulations, but not of that between the H and M or H and U simulations. Therefore, the discrepancies in the pore hydration of the U , M , and H simulations are still not completely understood.

Spontaneous Conduction of Ions Through the Hydrated Channel

A stably hydrated pore is necessary but not sufficient for ion conduction through the MscS crystal structure. Sotomayor and Schulten's work showed that membrane tension could oppose collapse and produce a hydrated channel, but no ionic conduction was seen in their simulations [27]. However, in the present simulations, the application of a transmembrane potential provides a natural driving force for ions to pass through the channel. Indeed, we observe a significant number of spontaneous ion transits through the channel when a voltage is applied.

We define a conduction event as the movement of an ion through the full length of the pore. For each simulation, a running total of the number of conduction events can be plotted as a function of time; on such a plot, a constant current is characterized by a more or less linear function. An approximation of the current can be calculated by dividing the number of events by the time between the first and last event. The most compelling case is $U+100$. Fig. 1.9A (upper red trace) shows that many conduction

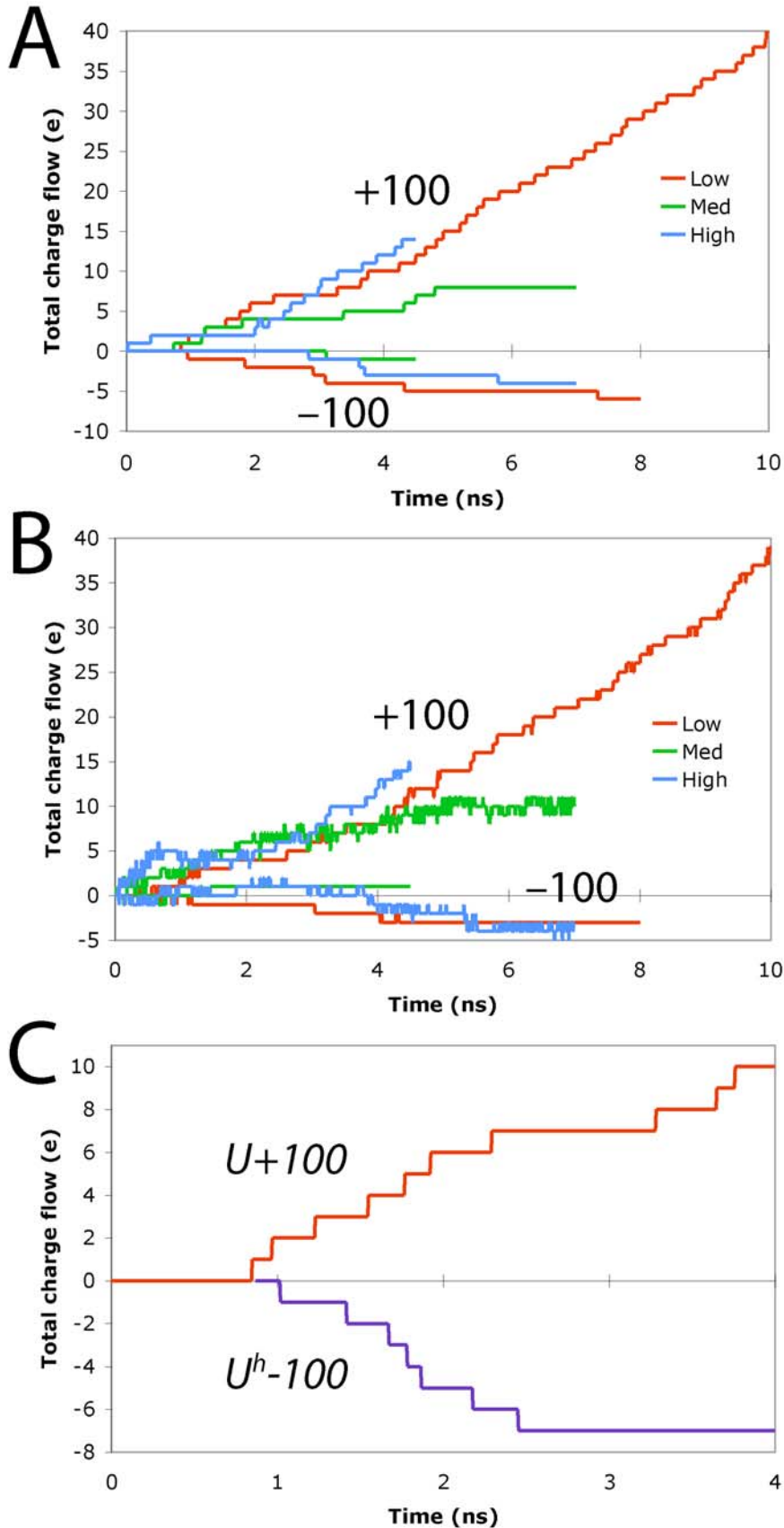


Table 1.1. Conduction and diffusion current data calculated from all wild-type MscS simulations that contained at least one conduction event

Simulation(s)	Field mV/nm	ΔV_z mV	Total Time ns	Conduction Current			Diffusion Current	
				Total Events ^a	Steady State ^b		Total Events ^a	St. State ^b <i>I</i> pA
					<i>I</i> pA	<i>g</i> nS		
<i>R+50</i>	+50	+550	6.0	1	Low ^c	Low	1	Low
<i>R+100, R^h+100</i>	+100	+1100	5.5	11	410	0.37	9	450
<i>U+100</i>			10.0	40	790	0.72	39	850
<i>M+100</i>			7.0	8	450	0.41	11	290
<i>H+100</i>			4.5	14	840	0.76	15	790
<i>R-100</i>	-100	-1100	6.0	2	Low	Low	1	0
<i>U-100, U^h-100</i>			11.1	13	Low	Low	5	0
<i>M-100</i>			4.5	1	Low	Low	1	0
<i>H-100</i>			7.0	4	-220	0.20	7	-260

^a All the events the entire simulation. ^b Calculated from only the steady-state regime.
^c Nonzero current or conductance that could not be meaningfully calculated, because it represents only 1 or 2 events.

events are observed during this simulation, and from ~3.3 ns onwards the charge movement data show a linear appearance. The current for this steady-state regime is calculated to be $4.9 e \text{ ns}^{-1}$, equivalent to 790 pA.

Other simulations, both restrained and unrestrained, generally showed a significant number of conduction events as long as the applied field was fairly large. Fig. 1.9A and table 1.1 summarize these results. Most of the conduction events—including all events in the low salt system—involved chloride ions. It should also be noted that not all the conduction events occurred in a steady-state regime, which is clear from fig. 1.9A. In several cases, particularly *U-100* and *U^h-100*, a current was observed early in the simulation, but the steady state of these simulations involved a very low current (fig. 1.9A–C). The discrepancy between steady-state currents in +100 and -100 mV/nm fields is discussed below.

Relating the calculated currents to the transmembrane potential allows for the determination of channel conductance. As seen in previous simulations, the transmembrane potential is equivalent to the potential drop across the entire periodic box [34, 35]. This phenomenon arises because the bath solution is a highly conductive environment compared to the membrane, so there is no potential difference throughout the aqueous region. Therefore, the entirety of the potential drop across the box is concentrated across the bilayer and protein, as discussed in more detail below. Therefore, the transmembrane potential ΔV_z can be determined as follows:

$$\Delta V_z = E_z L_z \quad (1.1)$$

where E_z is the constant electric field and L_z is the length of the simulation box in the z direction (very nearly 11.0 nm for all simulations). Therefore, for fields of +100, +50, +20, 0, -50, and -100 mV/nm, ΔV_z is 1100, 550, 220, 0, -550, and -1100 mV.

Single channel conductances calculated from the currents and transmembrane potentials for each simulation are shown in table 1.1. *U+100* and *H+100* have calculated conductance values of ~0.75 nS, close to experiment (1 nS). *R+100* and *M+100* have slightly lower conductances, although they are still within a factor of 2.5. Thus, in a field of +100 mV/nm, the conductance agrees quite well with experiment. Since the protein in these simulations shows only minor structural deviation from the crystal structure (fig. 1.5C–E), it is clear that the MscS crystal structure conformation can sustain a conductance that is consistent with the experimentally observed value.

The steady-state conductance measurements from -100 mV/nm fields are much lower than those from +100 mV/nm fields, indicating a deviation from Ohm's Law. This is most obviously revealed in the conduction data (table 1.1), but is also apparent from

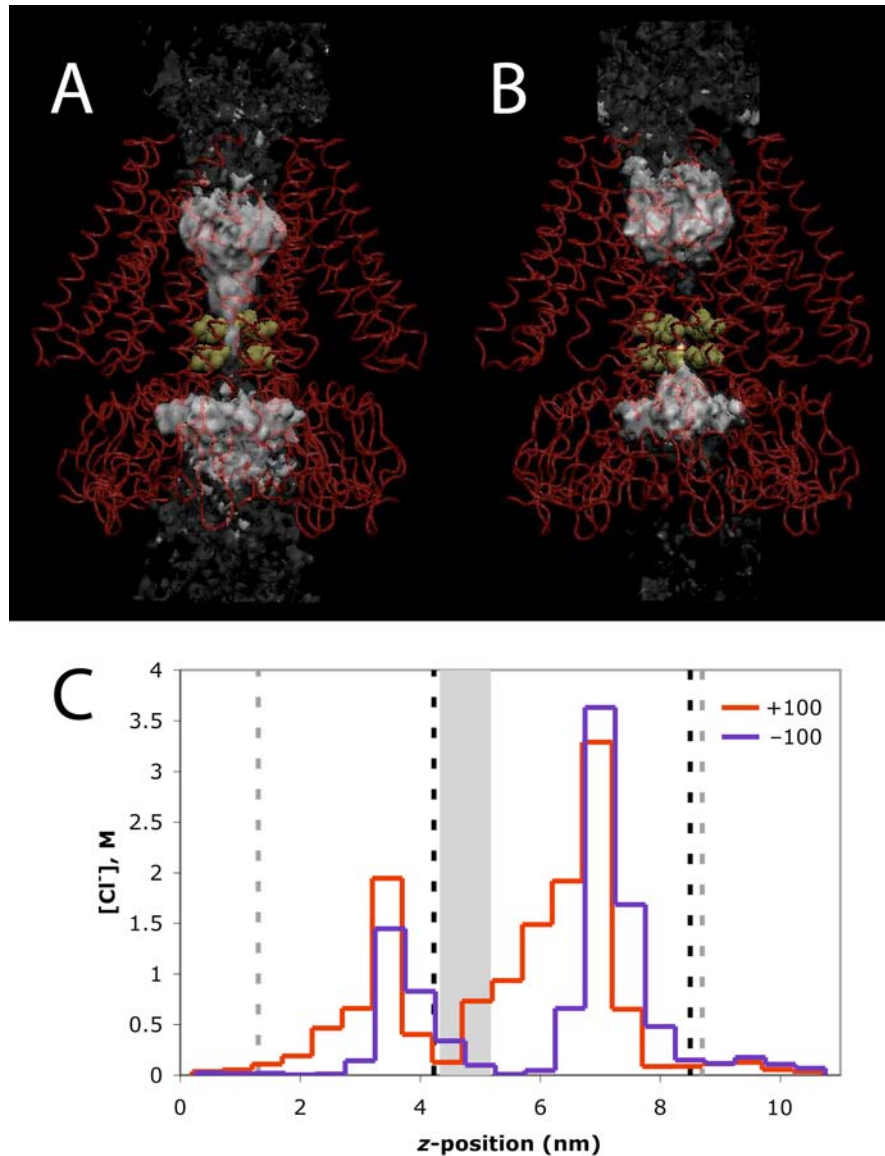


Fig 1.10. *A–B*, Time-averaged chloride density in the restrained simulations in fields of +100 (*A*) and –100 mV/nm (*B*). The regions with local concentrations of 1.33 M (opaque white) and 0.33 M (diffuse gray) are shown. The protein is shown in red, and L105 and L109 are shown in yellow spacefilling. *C*, The average chloride concentration in 0.25 nm slices of the channel region. Important regions of the simulation system are marked as in fig. 1.7D.

the local chloride concentrations (fig. 1.10). It is clear that the pore in a field of +100 mV/nm (fig. 1.10A) has a higher average chloride concentration than in a field of –100 mV/nm (fig. 1.10B). However, the discrepancy in the currents and conductances in opposite fields is not because of changes in the inherent conductance of the channel.

Instead, it is due to the fact that the current in the negative but not the positive fields is limited by diffusion, as discussed in the following section.

Diffusion Properties of Chloride Ions

The discrepancy in steady-state conduction currents between +100 and -100 mV/nm fields can be attributed to the differing abilities of the protein to resupply charge carriers to the periplasmic vestibule (the chloride source for conduction in positive fields) versus the cytoplasmic vestibule (the chloride source for conduction in negative fields). In any channel, a current can be sustained only if the arrival of new charge carriers at the channel's mouth is fast enough to replenish the ions that are conducted. The rate of diffusion to the mouth, therefore, is an upper limit on the current that a channel can sustain. Applying larger potentials cannot increase the current beyond this limit, so when currents are near the diffusion rate, the channel no longer follows Ohm's Law [1].

Diffusion currents (the flow of ions into the vestibules before their conduction) can be calculated in a manner similar to conduction current. Fig. 1.9B and table 1.1 summarize the data. The differences in diffusion into the periplasmic and cytoplasmic vestibules are immediately obvious. For $R+100$, R^h+100 , and $U+100$, we observe relatively large diffusion currents into the periplasmic vestibule. However, in the steady-state regimes of $R-100$, $U-100$, and U^h-100 , there are no diffusion events into the cytoplasmic vestibule. These observations lead to the conclusion that diffusion can adequately resupply chloride ions to the periplasmic vestibule under positive potentials,

but chloride ion flow into the cytoplasmic vestibule at negative potentials is limited by the rate of diffusion.

To verify this idea, the diffusion rates in the simulations with higher salt concentrations were compared to those in the low-salt simulations. If the conduction current is determined by the inherent conductance of the channel (Ohm's Law), increasing the concentration of the charge carriers should have no effect. However, if it is dictated by diffusion, increasing the concentration of the charge carriers should lead to increased conduction currents.

The former case is observed for fields of +100 mV/nm. For both $M+100$ and $H+100$, the conduction and diffusion currents are reasonably close to those in $R+100$ and $U+100$ (both of which use low salt). The independence of the current on the salt concentration indicates that with a +100 mV/nm field we have not reached the diffusion-limited current. In contrast, whereas the steady-state diffusion rates for $R-100$, $U-100$, and $M-100$ are essentially zero, increasing the salt concentration ($H-100$) increases the diffusion and conduction currents to measurable values (−260 pA and −220 pA). The fact that increasing the concentration of the charge carriers leads to higher currents in the −100 mV/nm field indicates that diffusion is indeed the rate-limiting factor.

Furthermore, the absolute value of the diffusion current (260 pA) is in reasonable agreement with the theoretical rate of diffusion to the cytoplasmic side of the MscS pore. The rate of diffusion of ions to a channel can be approximated as the rate of diffusion ϕ into a hemisphere of radius r spanning a channel's mouth [1]. In the absence of any gradients, this rate is determined as follows:

$$\phi = 2\pi r D c \quad (1.2)$$

where D is the diffusion coefficient and c is the concentration of charge carriers in the solution. For MscS we estimate that the appropriate radius is 0.5 nm on both the periplasmic and cytoplasmic sides of the pore. The ionic current is carried by chloride, which in high salt is at a concentration c of 300 mM (equivalent to $0.18 \text{ ions nm}^{-3}$) and has an aqueous diffusion coefficient D of $2.03 \text{ nm}^2 \text{ ns}^{-1}$ [1]. Therefore,

$$\phi = 2\pi(0.5 \text{ nm})(2.03 \text{ nm}^2 \text{ ns}^{-1})(0.18 \text{ ions nm}^{-3}) = 1.2 \text{ ions ns}^{-1}.$$

As such, if there were no gradients, the maximum sustainable current by a model pore of the dimensions of MscS is $1.2 e \text{ ns}^{-1}$, equivalent to 180 pA. The acceptable agreement between the $H-100$ currents and this theoretical diffusion rate provides further evidence that diffusion limits the negative current in -100 mV/nm fields.

The local chloride concentrations also reveal the discrepancy in the rates of diffusion into the two vestibules (fig. 1.10). In fields of $+100 \text{ mV/nm}$, there is significant chloride density throughout the region at the interface of the bulk solution and the periplasmic vestibule. In contrast, in fields of -100 mV/nm , the average chloride concentration at the interface of the bulk and the cytoplasmic vestibule is very low.

Because diffusion issues are not a concern in the $+100 \text{ mV/nm}$ simulations, it is appropriate to use these for an accurate determination of the conductance of MscS in our simulations. As mentioned earlier, the calculated value from these simulations is in good agreement with experiment. It is also worth noting that in the initial phase of U^h-100 , when there are ample charge carriers in the cytoplasmic vestibule, the conductance of the channel is 0.71 nS , very near to that for $U+100$ (fig. 1.9C). Only when the charge carriers are depleted (and not replenished by diffusion) does the current drop to its low steady-state value.

It should be noted that MscS in the simulation system is truncated after the middle- β domain (fig. 1.1B–C). The cytoplasmic vestibule is surrounded by the seven middle- β domains on the sides but is open on the bottom. In contrast, the cytoplasmic vestibule in full-length MscS is surrounded by the middle- β domains and the large C-terminal domains, with only small portals allowing ions to enter [23]. Thus, the full-length protein provides an even larger physical barrier to ionic diffusion into the cytoplasmic vestibule than does the model, and it is likely that the simulations overestimate the rate of diffusion of ions into the cytoplasmic vestibule. In addition, there are 26 disordered residues at the N-terminus of the crystal structure, which are not included in the simulation [23]. Because there is no known structure for this region, it is not clear how it influences diffusion rates into the periplasmic domain.

Potential Profile of the Simulation System

In the +100 mV/nm simulations, we observe diffusion currents that are significantly larger than the theoretical maximum of 180 pA. Therefore, in contrast to the cytoplasmic vestibule, the periplasmic vestibule must be an attractive sink for chloride ions. This is seen more clearly from analysis of the potential profile of the channel.

For each of the six applied electric fields, we determined the electric potential profile of the restrained simulation system (fig. 1.11). As mentioned above, like previous descriptions of transmembrane potentials, the entirety of the potential drop of the periodic box occurs in the actual transmembrane region [34, 35]. However, the protein environment causes the potential to deviate from the linear drop that would be expected for a homogeneous aqueous channel [35]. In our system, almost the entirety of the

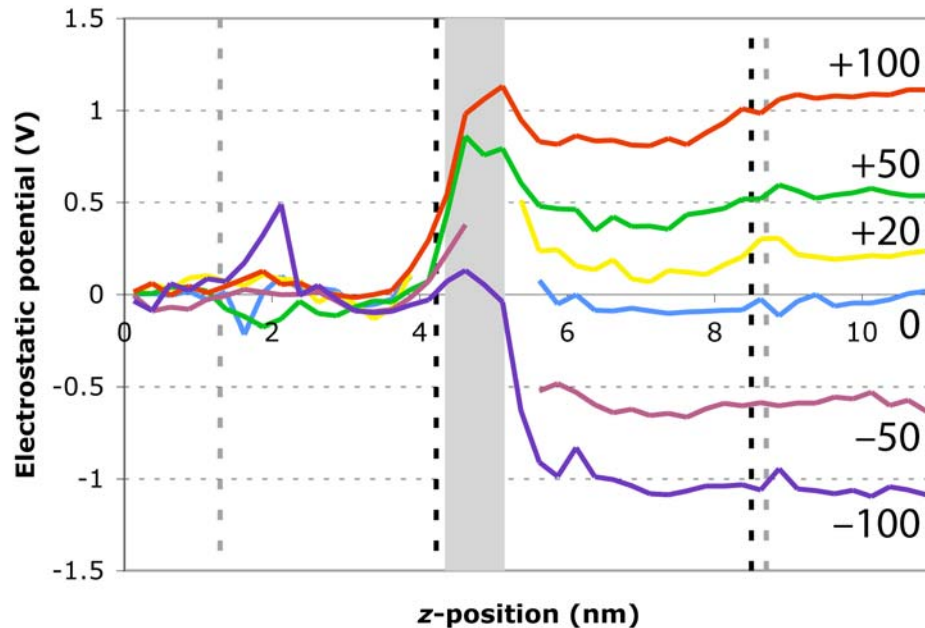


Fig. 1.11. Negative-ion electrostatic potential profiles for the simulation system under various electric fields in the R and R^h simulations. The plots for some fields are incomplete because no chloride ions were found in the pore region in some simulations. Important regions of the simulation system are marked as in fig. 1.7D.

potential drop occurs in the very narrow region of the pore. In addition, the relatively higher potential in this region indicates a significant barrier for chloride movement in either direction. This is undoubtedly due to the partial desolvation of the ion as it passes through the pore, as discussed below.

The protein provides different environments in the vestibules on either side of the pore. The periplasmic vestibule of the protein has a lower potential than the periplasmic bulk, most likely because of favorable interactions with the cationic residues in the TM domains. Furthermore, there is no barrier to entry from the bulk to the vestibule. The lower potential and lack of a barrier to entry create a sink for chloride that allows for a much higher diffusion than expected from theoretical considerations. The cytoplasmic vestibule, on the other hand, provides a potential no more favorable than the bulk, and

there even appears to be a slight barrier to entry. Therefore, diffusion into this vestibule is much slower than that into the periplasmic vestibule.

Simulations with Different Water Models and Temperature-Coupling Groups

Because simulations are only mathematical approximations, it must be demonstrated that our results are not artifacts of the specific parameters of the system. As discussed above, MscS simulations employing a different force field and software package also displayed the dehydration and occlusion of the pore in the absence of a potential and the maintenance of a wide, hydrated pore of the protein in a bilayer under tension [27]. The similarity of our results to these is evidence that the simulated phenomena are not simply artifacts.

To further demonstrate this, some simulations were performed using the TIP3P instead of SPC water model, and others were performed with the water and ions in a single temperature-coupling bath instead of separate ones. All of these simulations resulted in the same pore hydration (fig. 1.12A–B), ion conduction (fig. 1.12C), and ion diffusion (fig. 1.12D) behavior observed in our initial simulations. Therefore, it is very unlikely that the results presented here are artifacts of the simulation system.

Structural Features of the Conducting Versus the Occluded States

Our results provide the opportunity to compare the structures of a conducting form and an occluded form of the MscS channel. The contrasts are seen clearly in snapshots of MscS in the presence of a field of +100 mV/nm, in which the pore remains

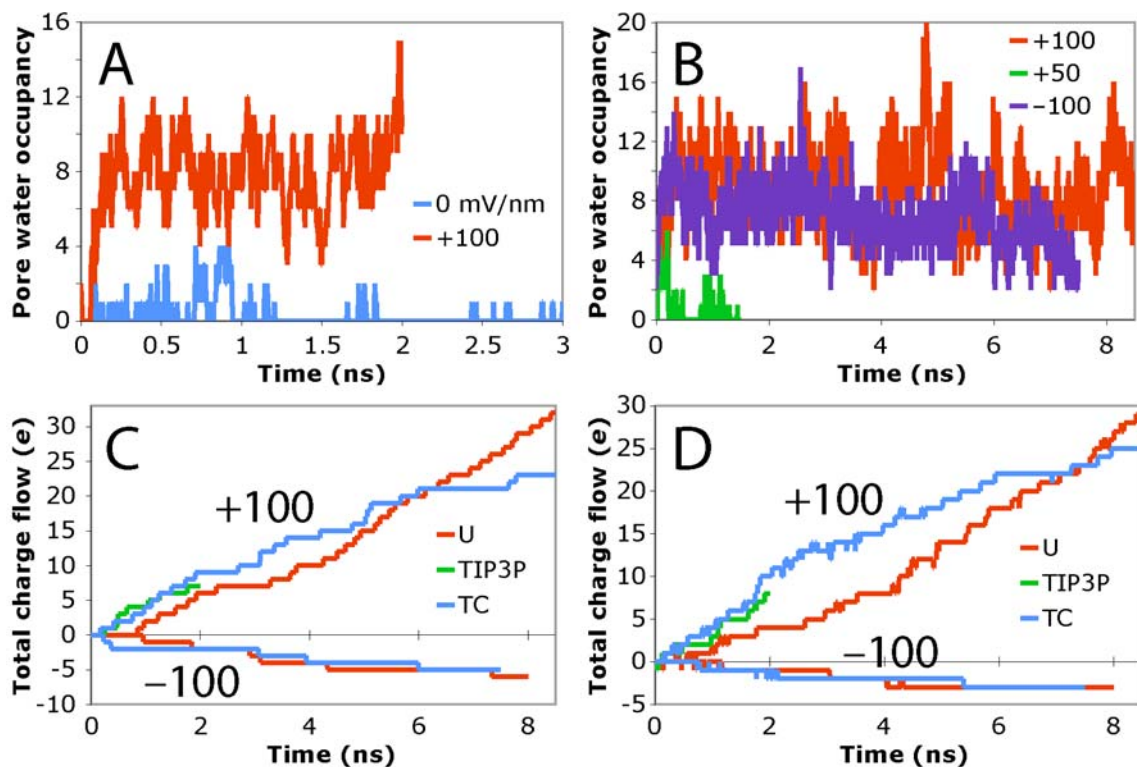


Fig. 1.12. *A*, Water occupancy of the pore in simulations using the TIP3P instead of SPC water model, with electric fields of +100 and 0 mV/nm. *B*, Water occupancy of the pore in simulations with the water and ions in a single temperature-coupling bath, with electric fields of +100, +50, and -100 mV/nm. *C–D*, Conduction (*C*) and diffusion (*D*) charge flow in simulations with fields of +100 and -100 mV/nm. U: the normal unrestrained simulations; TIP3P: simulations using TIP3P water; TC: simulations with the modified temperature-coupling baths.

fully hydrated and conducts well, and in the absence of a field, in which the pore has collapsed (fig. 1.4D–E). We will emphasize this pair in the analysis.

In the hydrated pore, the narrowest constriction—formed by L105 and L109—defines a pore radius of about 3 Å, similar to the crystal structure. This is the case for both +100 and -100 mV/nm fields. When there is no water in the pore, in low or moderate fields (-50 to +50 mV/nm), the constriction shrinks to less than 1 Å (fig. 1.13).

Later in *U+100*, the pore widens slightly beyond the original crystal structure radius. Both the occlusion and the widening of the pore result from asymmetric motions

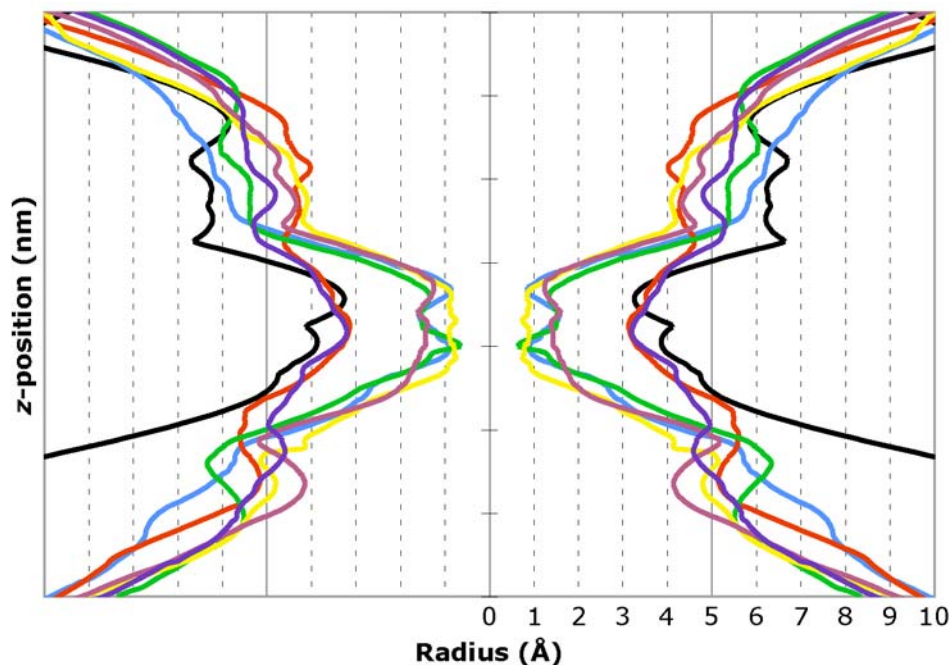


Fig. 1.13. Pore profiles, calculated by HOLE, for the crystal structure (black) and unrestrained simulations $U+100$ (red), $U+50$ (green), $U+20$ (yellow), $U0$ (blue), $U-50$ (magenta), and $U-100$ (purple). The profiles represent the pore at 3 ns in each simulation. Tick marks on the y-axis are 1 nm apart. The data have been reflected across the y-axis to create the appearance of a channel cross section.

of the TM3 helices. In both $U0$ and $U+100$, most of the TM3 helices undergo very little lateral movement in the pore region, but significant movement of only one helix results in the different pore states (fig. 1.14A–B). In $U0$, through a reorganization of the H-bonds and the unwinding of the turn at its N-terminus, TM3 of subunit C bends and moves into the empty pore (fig. 1.14C–E). Most of the other TM3s remain about the same distance from the center. The motion of TM3-C is very similar to the motions leading to the occluded state reported by Sotomayor and Schulten [27]. In $U+100$ we observe a different type of motion. During the expansion, TM3 of subunit F moves relatively far from the center, and its kink moves from G113 to A108, with a less severe kink angle (fig. 1.14F–G). A similar movement is observed for the adjacent TM3 from subunit G (fig. 1.14H). Because the timescale of the simulation is short, we cannot say that these

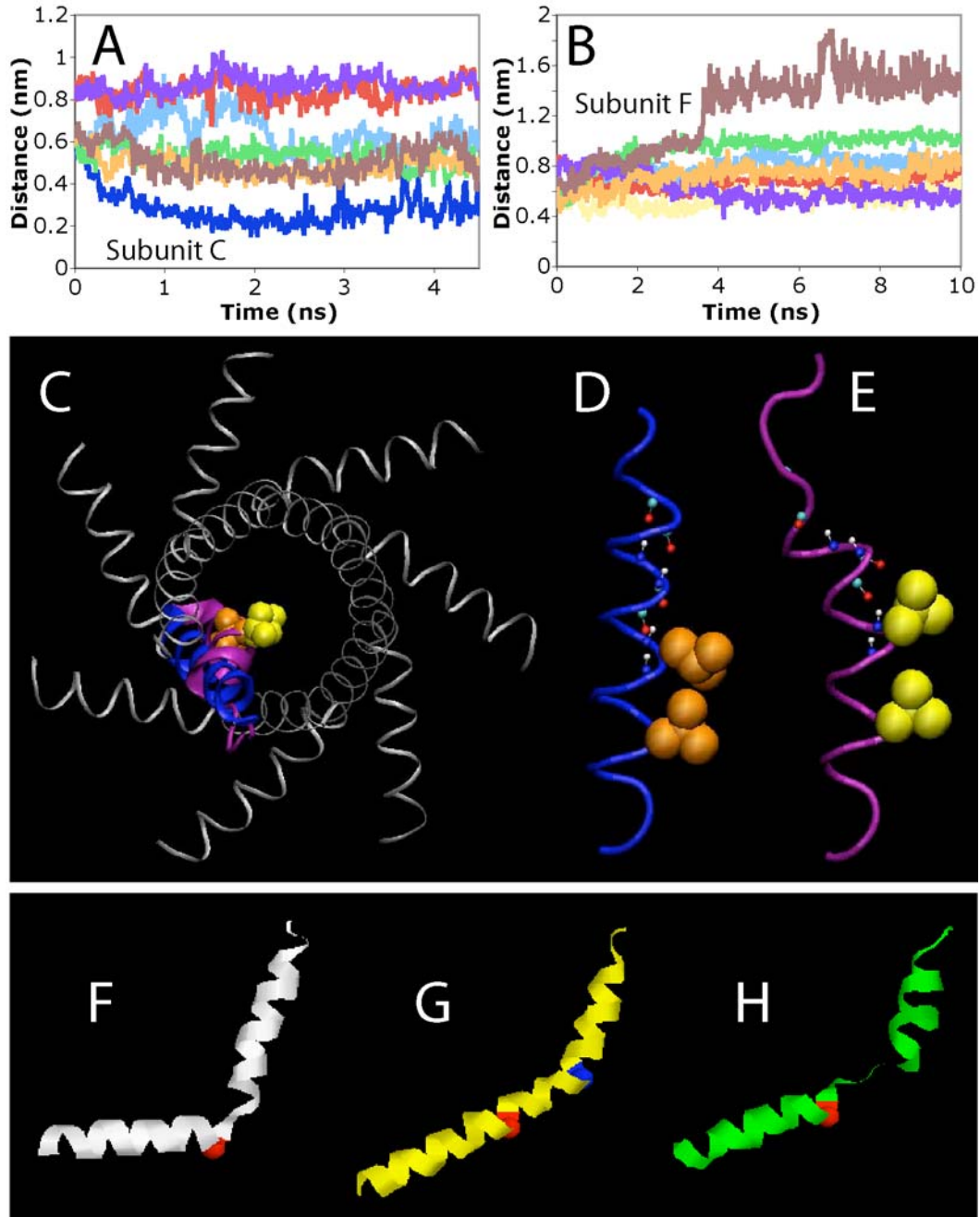


Fig. 1.14. A–B, Distance of each subunit from the pore center as a function of time for $U0$ (A) and $U+100$ (B). The distance represented is that from the center of mass of the seven L109 C α atoms to the Cy of L109 of each subunit. C–E, Snapshots of TM3 of subunit C at the beginning (blue) and end (purple) of $U0$. The sidechains of L105 and L109 are shown in spacefilling at the beginning (orange) and end (yellow) of $U0$. The view from the periplasm (C) shows how far the helix moves into the center of the pore. The TM3 helices of all the subunits are depicted in gray to clarify the pore at the beginning of $U0$. The side views (D–E) show the unwinding of the helix during the simulation. In addition, several backbone carbonyl and amide groups that begin in a normal α -helical hydrogen bonding arrangement (D) are broken as the helix is distorted (E). F–H, Snapshots showing side views of the TM3 helices of the E, F, and G subunits (panels F, G, and H, respectively) at the end of $U+100$. Red spheres represent the C α of G113, and the blue sphere represents the C α of A107-F, which has become the location of the helical kink. TM3-E is representative of a helix that remains similar to the crystal structure.

are relevant motions in a global conformational change, but it is notable that TM3 displays so much flexibility.

Another important structural feature is the solvation state of chloride ions as they pass through the pore. In Anishkin and Sukharev's simulations, a chloride that is forced to pass through the restrained MscS pore experiences a severe loss of solvation, losing all but half of its first solvation shell [26]. The high degree of desolvation required to conduct an ion provided some of the evidence for their claim that the MscS crystal structure must be a nonconducting state. For our simulations, we analyzed the solvation of the chloride ions passing through the pore by calculating their radial distribution function (RDF) $\rho(r)$.

Fig. 1.15 shows the calculated RDF of water oxygen atoms around chloride ions in bulk water, as well as the averaged RDF of 33 chloride ions in the steady-state phase

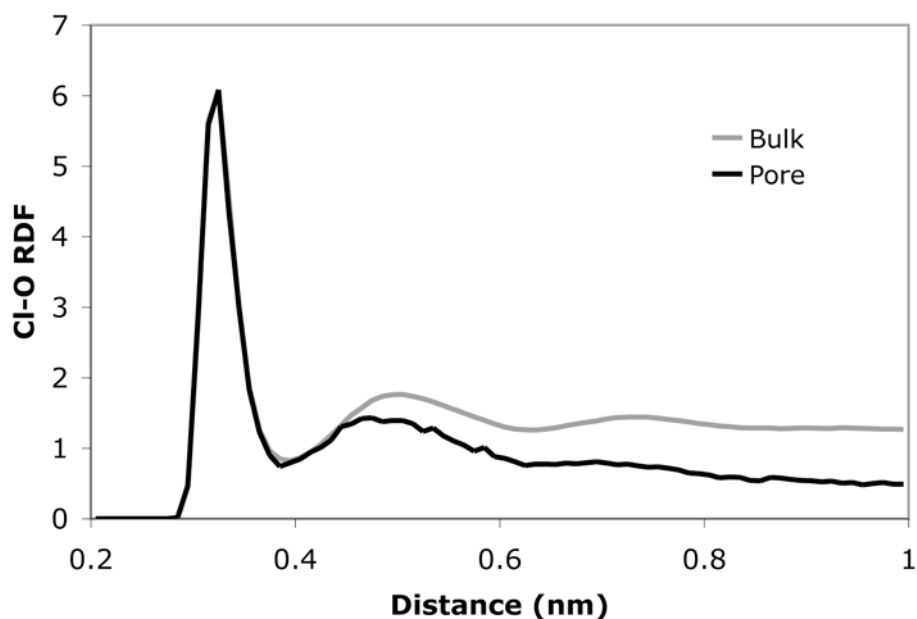


Fig. 1.15. Radial distribution functions (RDFs) of water oxygen atoms around chloride ions in the bulk and pore regions in $U+100$. The pore RDF is the average of the individual RDFs of the 33 chloride ions that were conducted in the steady-state regime, weighted by the length of time the ion spent in the pore.

of $U+100$ for only the times that they were in the pore. The “pore” chloride RDF is relatively noisy because there are fewer data points available for chloride ions in the pore than in the bulk.

The RDF of the bulk chloride shows three distinct solvation shells, with maxima at about 0.32, 0.50, and 0.73 nm. The number of waters present in each shell can be determined by integration of the function $r^2\rho(r)$. For chloride in the bulk, the shells are occupied by 7, 21, and 35 waters, respectively, although it is difficult to determine a precise endpoint for the third shell. These results—both the radii and occupancy of the solvation shells—agree well with those from previous experimental and computational work [36].

The RDF for the chloride ions in the pore shows different characteristics. A chloride in the pore does have a reduced solvation shell, but its first hydration shell is still essentially intact. Only the second shell and beyond have a lower occupancy. Integration of the peaks reveals that whereas the first shell has the full 7 waters, the second shell contains only 16 waters, and there is only a faintly discernable third shell. Although this amount of solvation is significantly less than that observed for the bulk chloride ions, it is much greater than that reported previously [26].

Studies of Selected Mutant Channels

MscS contains a number of charged residues in its transmembrane domains, including R46, R54, D67, R74, and R88 (fig. 1.16A). As noted above, transmembrane arginine residues likely play an important role in voltage sensing in other ion channels, so we performed several simulations, all completely unrestrained, of MscS mutants in which

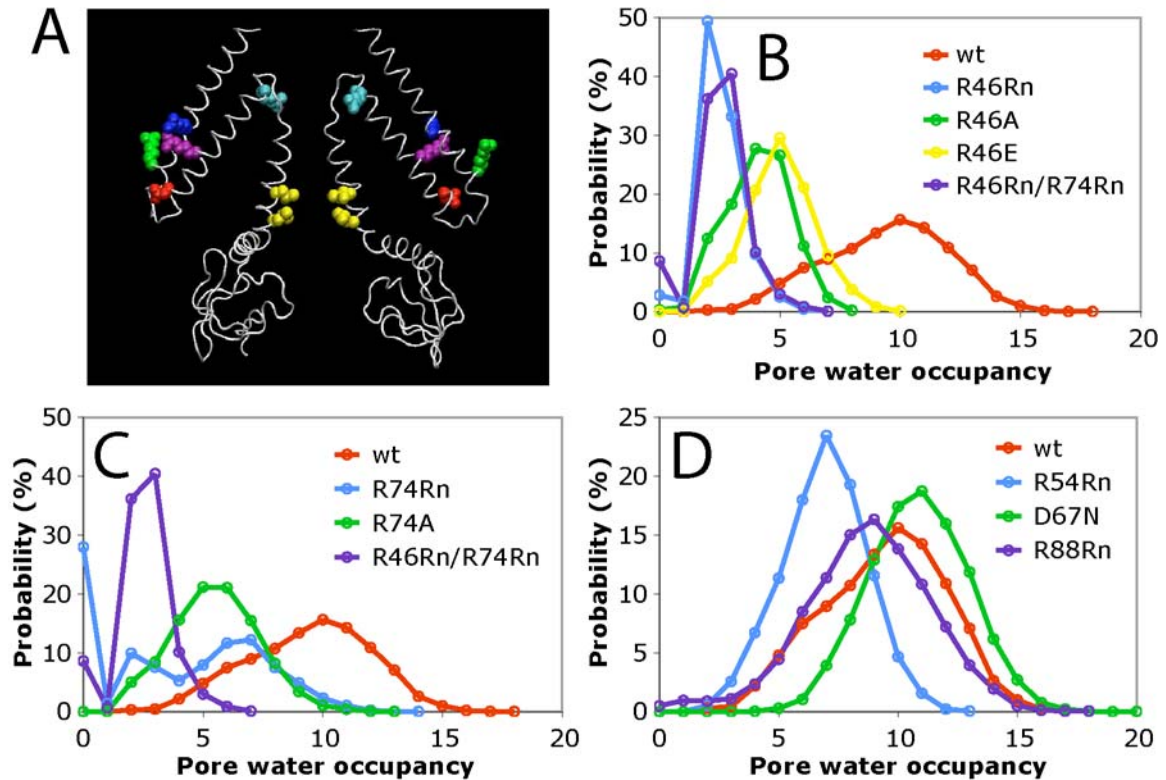


Fig. 1.16. A, View of the charged residues in the TM domains. Only two subunits are shown for clarity. The side chains of R46 (blue), R54 (green), D67 (red), R74 (purple), R88 (cyan), and L105 and L109 (yellow) are shown in spacefilling. B–D, Probability distributions of pore water occupancy in unrestrained simulations of R46 mutants (B), R74 mutants (C), and other mutants (D).

these charges were altered. The following mutants were studied: R46Rn, R46A, R46E, R54Rn, D67N, R74Rn, R74A, R46Rn/R74Rn, and R88Rn. Rn refers to a “neutralized arginine” residue that is missing one proton from the guanidinium group.

The water occupancies for the mutants are shown in fig. 1.16B–D. Mutations at R54, D67, and R88 do not have a substantial effect. However, mutations at R46 and R74, even to another polar residue, greatly reduce the hydration of the pore.

A possible explanation for these effects is that the charges, although distant, still contribute significantly to the electrostatic character of the pore. In model pores, partial charges greatly reduce the hydrophobicity and lead to greater pore hydration [9, 37]. In our case, the charges do not lie directly on the pore wall, but they apparently create a

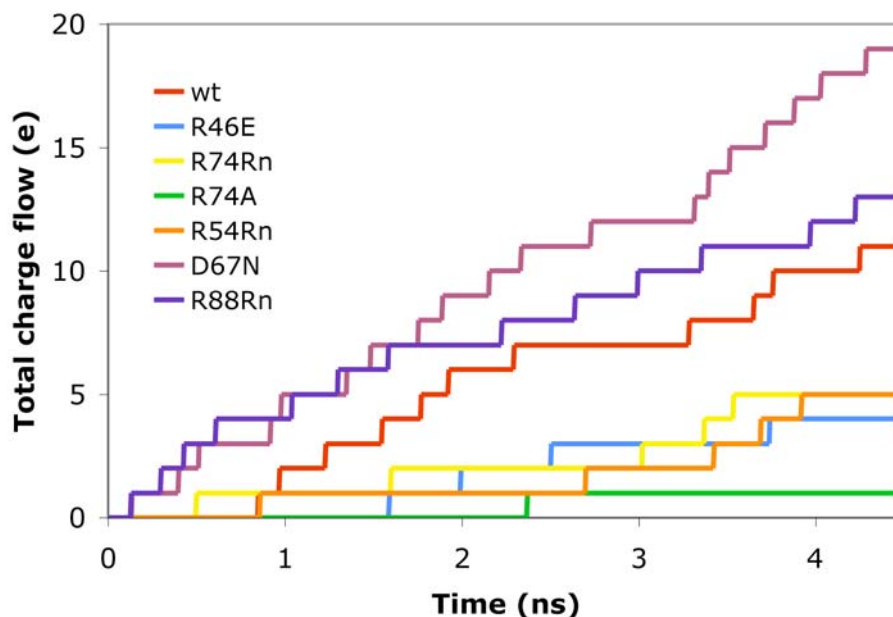


Fig. 1.17. Conductive charge movement for all the mutant simulations that produced at least one conduction event. The field in all the simulations is +100 mV/nm.

Mutant	Total Events	Steady State	
		I pA	g nS
wt	40	790	0.72
R46Rn	0	0	0.00
R46A	0	0	0.00
R46E	4	Low	Low
R74Rn	5	930	0.85
R74A	1	0	0.00
R46Rn/R74Rn	0	0	0.00
R54Rn	5	530	0.48
D67N	19	730	0.66
R88Rn	13	480	0.44

Table 1.2. Data on conduction currents for all mutant simulations, which contain a field of +100 mV/nm and a transmembrane potential of +1100 mV. Meanings of the headings are the same as those for table 1.1.

more hydrophilic environment. Removing the charges may make the pore more hydrophobic, thus reducing the hydration.

As expected from the fact that R54, D67, and R88 mutants have similar water behavior to wild type, conduction current data for these mutants are also reasonably close to wild type (fig. 1.17 and table 1.2). R46 and R74 mutants, on the other hand, have

lower currents, in line with the fact that they generally have less hydrated pores. R74Rn is an apparent exception to this trend, although the number of conduction events is small (only three in the steady-state regime) and probably does not accurately reflect the true conductance. These data indicate that mutations at R46 and R74 may result in loss-of-function channels.

There is no polarization built into the force field in our simulations, and there are no diffusible molecules between the transmembrane charges and the walls of the pore. Because the dielectric constant of the protein interior in our model is effectively 1, the influence of the charges is probably exaggerated. However, generally accepted values for the dielectric constant for proteins are typically quite low, in the range of 2–4 [38], so it is unlikely that the exaggeration is severe.

Investigation of the Mechanism for Voltage Modulation

Electrophysiological studies have demonstrated that voltage modulates MscS function. Early work suggested that depolarization of the membrane leads to increased open probabilities and a decreased threshold for activation by tension [14], but more recent work has indicated that voltage modulates deactivation but not activation [19]. In either case, MscS is sensitive to voltage changes. The crystal structure provided insight into a possible mechanism for this: a hinging motion of the TM1-TM2 arm that correlates lateral expansion (tension sensitivity) with upward movement of positive charges on the TM domains (voltage sensitivity) [23]. Our MD simulations shed some light on this mechanism, in that we can observe TM domain motion under the influence of different electric fields. The U simulations show that the positions of the TM1 and

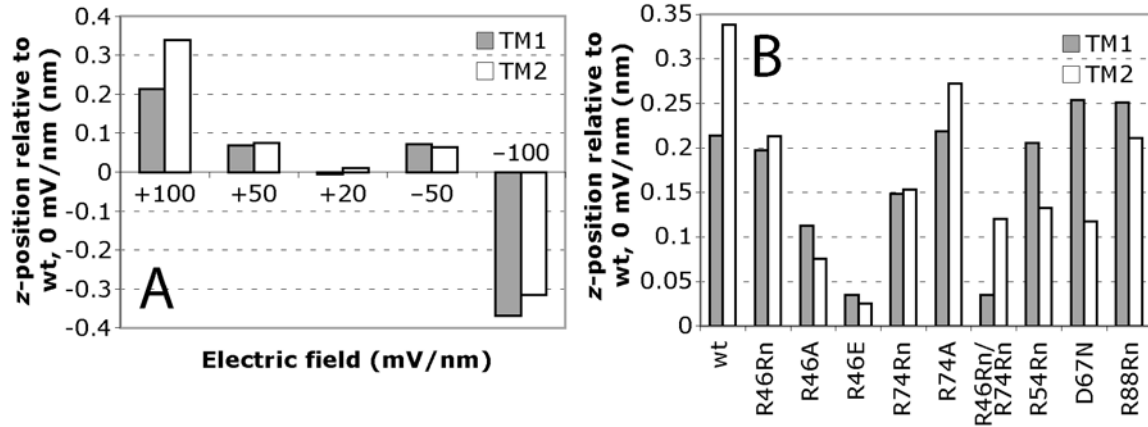


Fig. 1.18. Positions of the centers of mass for TM1 and TM2 averaged over the final 0.5 ns of some simulations, relative to that for $U0$. The positions are also corrected for fluctuations in the position of the lipid bilayer. *A*, U simulations of wt-MscS with different electric fields. *B*, Mutant simulations with an electric field of +100 mV/nm.

TM2 helices are indeed correlated with the field (fig. 1.18A). Relative to the unperturbed channel (in the absence of a field), the TM helices are nearer to the periplasm in the +100 mV/nm field, nearer to the cytoplasm in the -100 mV/nm field, but relatively unchanged in the low and moderate fields.

Furthermore, mutation of the charged residues within TM1 and TM2 alters the relative positions of the helices in the +100 mV/nm field in some cases (fig. 1.18B). For TM1 movement, most mutants have behavior similar to wild type (R46Rn, R74Rn, R74A, R54Rn, D67N, and R88Rn). The R46A, R46E, and R46Rn/R74Rn mutants, however, show only a slight positional change from the structure at 0 mV/nm, which suggests that R46 is the most important residue for voltage sensitivity. Mutants at this position are less responsive to transmembrane potential changes than wild type. The data for TM2 correlate reasonably well with the TM1 data, except for the R54Rn and D67N mutants, which show smaller positional changes than wild type for TM2.

It should be noted, however, that in our simulations the positions of the helices do not correlate with the hydration and conduction of the channel. In +100 and

–100 mV/nm fields, MscS contains a stably hydrated pore but has TM domains in quite different positions within the membrane. Taken together with the fact that MD simulations of only a few ns are too short to show protein conformational changes, it is not clear if the TM domain motions observed here are relevant to the activation or deactivation processes.

CONCLUSION

The MscS channel is a fascinating structure that responds to both membrane tension and transmembrane potential. The crystal structure of Rees and co-workers [23] provided many insights, but also raised intriguing questions about the relationships between structure and function in this channel. The simulations presented here confirm and expand upon previous work and also provide valuable new insights into the workings of MscS.

Both the minimalist system of Anishkin and Sukharev [26] and the much more complete model of Sotomayor and Schulten [27] concluded that, in the absence of a transmembrane potential, the crystal structure contains a “hydrophobic gate” that excludes water from the narrowest region of the channel and cannot be conducting. Our studies support that conclusion. However, this is only part of the story.

We now find that an applied voltage can prevent collapse of the unrestrained channel. Sotomayor and Schulten showed that the collapse could also be prevented if a substantial tension is applied to the membrane [27]. Importantly, in our simulations the open channel is extensively hydrated, and the degree of hydration depends on the magnitude of the voltage. This hydrated channel is able to conduct chloride ions, and the

single channel conductances seen are comparable to experimentally observed values. Much lower sodium ion conductance is seen, consistent with the known anion selectivity of the channel. Also, the severe desolvation of pore chloride ions seen by Anishkin and Sukharev is not seen here [26]. The hydrated channel under the influence of an electric field can readily accommodate a well-solvated chloride. As anticipated, preliminary simulations of mutant channels show that key transmembrane arginine residues play a critical but as yet not fully understood role in controlling the voltage sensitivity, hydration, and conductance of the channel.

To our knowledge, this is the first MD investigation of the influence of a transmembrane potential on the hydration of hydrophobic nanopores. Our results suggest that an increasing potential reduces the threshold radius for pore hydration. Although the transmembrane potentials applied in these simulations (at least 220 mV), are substantially higher than the 120–160 mV reported for bacterial membranes [32], the tensions employed by Sotomayor and Schulten are also unphysiologically high [27]. It has been noted before that, to observe effects on MD timescales, the magnitudes of external stimuli (both tension and voltage) generally must exceed the physiological range [39, 40]. Also, previous simulations of ion movement in membrane channels have used potentials as large or larger than the potentials used here [35, 41].

Of course, the simulations presented here and elsewhere are still quite approximate. The timescales are relatively short, and the force fields are imperfect. Furthermore, with a resolution of 3.9 Å and sevenfold averaging, there is still some uncertainty about precise details of the MscS structure. Nevertheless, all the observations derived from the present simulations are consistent with experimental facts, and it seems

likely that the qualitative behaviors seen here do reflect the situation under physiological conditions. Based on these observations, we conclude that the image of MscS derived from the crystal structure is more nearly that of an open, conducting state of the channel than a nonconducting state.

METHODS

Assembly of Simulation System

The initial structure for the protein, lipid, water, and ions was created as follows. The coordinates from the *E. coli* MscS crystal structure (PDB 1MXM) [23] were transformed so that the sevenfold axis was parallel to the z -axis. Because molecular dynamics simulations on full-length MscS would require huge amounts of CPU time due to the large number of atoms, the protein chains were truncated at the ends of the middle- β domains (fig. 1.1B), so that the model of each subunit extended from F27 (the N-terminus of the crystal structure) to S179. It is assumed that the truncated protein is a reasonable system for study because the cleaved portion, the C-terminal domain, is unlikely to strongly influence the region of interest, the pore. For all ionizable side chains, the protonation state was chosen to simulate a system at neutral pH. However, the N- and C-termini were kept neutral (NH_2 and CO_2H), reflecting the fact that the simulated peptide chains do not actually extend to the terminal residues of the protein.

The protein was embedded in a pre-equilibrated POPE bilayer model in the manner described previously [42]. SPC water was added to fill the remainder of the simulation box. Sodium and chloride ions were also added for two reasons. First, a salt solution is more physiologically relevant than a pure water solvent. Second, the large

+42 charge on the protein must be neutralized to avoid artifacts in the long-range electrostatics algorithm [43]. Therefore, for a low-salt system that approximates a NaCl concentration of 100 mM, 62 of the water molecules were replaced with 10 Na⁺ and 52 Cl⁻ ions. Medium (200 mM) and high (300 mM) salt solutions contained 61 Na⁺ and 103 Cl⁻ ions and 113 Na⁺ and 155 Cl⁻ ion, respectively. The wild-type MscS, low-salt system contained seven protein chains of 153 residues each, 455 POPE molecules, 28423 water molecules, 10 Na⁺ ions, and 52 Cl⁻ ions, for a total of 118665 atoms (fig. 1.1C). The simulation system was minimized using the steepest-descents method.

Molecular Dynamics

All minimizations and molecular dynamics were performed with GROMACS 3.1.3 and 3.1.4 software [44, 45] with the GROMACS force field supplemented by parameters for the lipid [46]. Van der Waals and short-range electrostatics were cut off at 1.0 nm, and the long-range electrostatics were treated with the particle mesh Ewald (PME) method of order 4 and grid spacing of 0.1 nm [43].

The minimized structures were heated to 310 K over 20 ps with heavy harmonic position restraints [force constant: 1000 kJ/(mol nm²)] on all C α atoms. Once at 310 K, the heavy restraints were maintained for 180 ps, and then gradually lifted over 330 ps. The frame at 350 ps (of the 530 ps total), which followed equilibration with a restraining force constant of 500 kJ/(mol nm²), was used as the starting structure for the restrained simulations. The final frame (at 530 ps) was used as the starting frame for the unrestrained simulations.

In all simulations, the temperature was maintained at 310 K by coupling to Berendsen thermostats with a time constant of 0.1 ps [47]. Separate baths were used for the protein, the lipid, the solvent, the Na^+ ions, and the Cl^- ions. Likewise, pressure was maintained with anisotropic pressure coupling in each direction to a Berendsen barostat at 1 bar with a time constant of 1.0 ps [47].

Fig. 1.2 indicates the salt system, restraints, electric field, initial pore hydration state, and start and end times of each wild-type MscS simulation. In all restrained simulations, all the atoms of the protein backbone were harmonically restrained with a force constant of $418.4 \text{ kJ}/(\text{mol nm}^2)$ [$1 \text{ kcal}/(\text{mol \AA}^2)$]. The pore at time 0 of the restrained simulation was hydrated (R^h), and simulations with electric fields of 0 and +100 mV/nm were run for 2.5 ns. The frame at 1.47 ns of the 0 mV/nm simulation, which contains a pore empty of water, was used as the initial frame for other simulations (R), with applied electric fields of +100, +50, +20, -50, and -100 mV/nm.

Unrestrained simulations of the low-salt system beginning with an empty pore (U) were performed with electric fields of +100, +50, +20, 0, -50, and -100 mV/nm. The frame at 0.87 ns of the +100 mV/nm simulation, which contains a hydrated pore, was used as the initial frame for three more unrestrained simulations (U^h) with electric fields of +50, 0, and -100 mV/nm. Unrestrained simulations with the medium-salt (M) and high-salt (H) systems were performed with electric fields of +100, 0, and -100 mV/nm.

Control simulations were also performed with the unrestrained, low-salt system. The TIP3P instead of the SPC water model was used in one series of simulations, which were performed with applied fields of 0 and +100 mV/nm. In the other series of

simulations, which were performed with fields of +50, +100, and -100 mV/nm, the water and ions were placed in a single temperature-coupling bath instead of separate ones.

Simulations with Mutant MscS

Unrestrained simulations were also performed with mutant MscS proteins under low-salt conditions. Five charged residues in the transmembrane domains of MscS—R46, R54, D67, R74, and R88—were explored by mutation in eight single mutants and one double mutant: R46Rn, R46A, R46E, R54Rn, D67N, R74Rn, R74A, R46Rn/R74Rn, and R88Rn. Rn is a neutralized arginine model in which one of the terminal protons has been removed, eliminating the charge on the side chain. Even though this residue is almost certainly never found *in vivo*, its parameters are available in the GROMACS force field. All of the mutations gave structures in which a charged residue was neutralized, except for R46E, in which the +1 charge was mutated to a -1 charge.

The mutant models were created from the initial low salt structure, and with one exception (D67N) no additional minimization was required. For the D67N mutant, only the lipid molecules and side chains that were within 0.5 nm of the N67 side chains were allowed to move. In this way, the close contacts induced by the mutations were removed while minimizing the perturbation to the initial structure. Because of the changes in the protein charge, ions were added to the systems to restore neutrality. Simulations for all mutants were performed with an electric field of +100 mV/nm for 4.47 ns.

Data Analysis

RMS deviations were calculated by `g_rms`. The reference group for alignment was all C α atoms, and the reference structure was the structure of the protein after the energy minimization of the entire system. For each frame in the trajectory, the reference group was aligned with that of the reference structure, and the RMS deviation for the whole protein was calculated. The total system energies were determined by using `g_energy`.

The pore as defined for water and ion occupancy determinations consisted of a cylinder with radius 1.5 nm between the centers of mass of the L105 and L109 C α atoms. Water and ion occupancies of the pore were monitored as a function of time with the GROMACS analysis tool `g_occupancy`. The code is not a standard part of the GROMACS package but was a generous gift from David Bostick (University of North Carolina).

A conduction event is defined as the full transit of an ion through the pore. The total charge flow through the pore was monitored by keeping a running total of the conduction events in each simulation. A steady-state regime of the simulation was usually easily discernable as a linear region in the plot of total charge flow as a function of time. The slope of the function in each steady-state regime represents the average current, which was determined by dividing the cumulative charge flow by the time between the first and last conduction events. Currents in MD simulations have been calculated previously using a qualitatively similar technique [34].

Diffusion currents were calculated similarly. A diffusion event was defined as the movement of an ion into a vestibule. The periplasmic vestibule was defined as a cylinder

of radius 1.5 nm between the centers of mass of the C α of L105 and V91, and the cytoplasmic vestibule as a cylinder of radius 1.5 nm between the centers of mass of the C α of L109 and G140 (fig. 1.1B). The cumulative number of diffusion events was plotted as a function of time, and the steady-state diffusion current was calculated by dividing the number of diffusion events by the time between the first and last events.

The net alignment of the water as a function of position in the simulation system was determined with `g_h2order`. Only the water molecules that occupied the pore at some point in a given trajectory were included in the calculation. This restriction was imposed because the z -position of the pore was quite close the cytoplasmic side of the bilayer, and the net alignment of the water in the pore would have been swamped by the many water molecules penetrating the headgroup region of the membrane.

The interaction energy distributions of the water in the pore of the restrained simulation systems with fields of 0, +20, +50, and +100 mV/nm were determined from at least 5000 individual interaction energies in each simulation. The individual interaction energies were calculated as the difference between the total energy of the system in a given frame of the trajectory with and without the water molecule. For each frame, the total energy was calculated using `g_energy`, and the pore water molecules were identified. One by one, they were manually removed from the system, and the energy was recalculated. Finally, the interaction energy distributions were shifted to account for the orientation energy of the water dipoles with the electric field. The orientation energy of a dipole of magnitude d with a field of magnitude E is

$$Energy = -Ed \cos \theta \quad (1.3)$$

where θ is the angle between the two vectors [48]. The average orientation energy for an ensemble of water molecules in the pore follows:

$$Energy = -E\langle N \rangle d\langle \cos \theta \rangle \quad (1.4)$$

where $\langle N \rangle$ is the expectation value for the occupancy of the pore. $\langle N \rangle$ was calculated from the probability distribution of the water occupancies (shown in fig. 1.4C), and $\langle \cos \theta \rangle$ is the net alignment, determined above.

The local chloride density was determined using `gridcount`, which is not part of the standard GROMACS package but is available for download on the contributions website (<http://www.gromacs.org/contributions/index.php>).

Electric potential profiles for negative ions for each of the six applied electric fields were determined for the restrained simulation system by calculating the average electrostatic energy of a chloride ion as a function of its position in the box. Chloride ions that sampled different regions of the simulation system were selected for analysis, but only for the times that they remained within approximately 2 nm of the protein's sevenfold axis. For the selected chloride ions, both the z -position (determined by `g_traj`) and the electrostatic energy between the ion and the rest of the system were computed at each time in the simulation. The calculation of the electrostatic energy was performed in the following manner. The trajectory of a simulation was rerun with nonstandard energy groups consisting of the single chloride ion of interest and the rest of the system. The short-range electrostatic energy was obtained using `g_energy`. However, the long-range electrostatic energy calculated by the PME algorithm cannot be broken down into separate energy components between particular atoms; it merely contributes a system-wide long-range electrostatic energy term to the total energy. To

overcome this complication, the trajectory was rerun a second time, with the charge of the chloride of interest artificially set to 0 (with `tpbconv -zeroq`). The difference between the total long-range electrostatic energies (obtained using `g_energy`) for the two rerun trajectories was the long-range energy for the chloride ion and the system. The sum of the short-term and long-term electrostatic energies was the total electrostatic energy. The energy values were placed in bins of width 0.25 nm according to their corresponding z -positions, and the average energy was calculated for each bin. The energy purely due to the electric field, which depends only on the z -position, was added to the bin's average energy to obtain the final potential as a function of position. For some electric fields, no chloride ions were ever found in the pore region, so the potential profiles were incomplete.

Pore radii were calculated by HOLE [49], which moves a flexible balloon along the length of the channel, and at each point, calculates the largest radius that can be accommodated.

Radial distribution functions (RDFs) were calculated using `g_rdf`. For the RDFs of just the chlorides in the pore, `g_occupancy` was used to determine the exact times that each chloride occupied the pore, and the RDF for this chloride was determined for only those times. The final RDF of the pore chlorides was calculated as a weighted average of the individual RDFs, weighted by the total number of timepoints from which the RDF was calculated.

TM1 and TM2 movements of wild-type and mutant MscS were analyzed in the following manner. For each simulation, the z -positions of the centers of mass of all the atoms in TM1, TM2, and lipid as a function of time were determined. For each time, the

position of the lipid was subtracted from the positions of the TMs. The average of these differences over the last 500 ps of the simulation was calculated as the TM position relative to the lipid. Finally, these relative positions were compared to the relative position determined for *U0*.

Images were prepared with VMD [50] and Rasmol.

Computers

Three computers were used for all of the simulations: Blackrider, a dual processor Dell Precision 530 running GROMACS 3.1.3 on a Red Hat Linux 7.1 operating system (OS); Strongbad, a dual processor Dell Precision 450 running GROMACS 3.1.4 on a Red Hat Linux 8.0 OS; and Liligor, a dual processor Dell Precision 420 running GROMACS 3.1.4 on a Red Hat Enterprise Linux OS. Typical speeds of MD simulations with the MscS system were 78, 86, and 34 ps/day on Blackrider, Strongbad, and Liligor, respectively.

REFERENCES

1. Hille, B. 2001. *Ion Channels of Excitable Membranes, Third Edition*. Sunderland, MA: Sinauer Associates, Inc.
2. Zhou, Y., J. H. Morais-Cabral, A. Kaufman, and R. MacKinnon. 2001. Chemistry of ion coordination and hydration revealed by a K⁺ channel-Fab complex at 2.0 Å resolution. *Nature*. 414:43-48.
3. Betanzos, M., C. S. Chiang, H. R. Guy, and S. Sukharev. 2002. A large iris-like expansion of a mechanosensitive channel protein induced by membrane tension. *Nat. Struct. Biol.* 9:704-710.
4. Sukharev, S. 2002. Purification of the small mechanosensitive channel of *Escherichia coli* (MscS): the subunit structure, conduction, and gating characteristics in liposomes. *Biophys. J.* 83:290-298.

5. Song, L., M. R. Hobaugh, C. Shustak, S. Cheley, H. Bayley, and J. E. Gouaux. 1996. Structure of staphylococcal alpha-hemolysin, a heptameric transmembrane pore. *Science*. 274:1859-1866.
6. Evans, R. 1990. Fluids adsorbed in narrow pores—phase-equilibria and structure. *J. Phys.: Condens. Matter*. 2:8989-9007.
7. Beckstein, O., P. C. Biggin, and M. S. P. Sansom. 2001. A hydrophobic gating mechanism for nanopores. *J. Phys. Chem. B*. 105:12902-12905.
8. Beckstein, O., and M. S. Sansom. 2003. Liquid-vapor oscillations of water in hydrophobic nanopores. *Proc. Natl. Acad. Sci. USA*. 100:7063-7068.
9. Beckstein, O., and M. S. Sansom. 2004. The influence of geometry, surface character, and flexibility on the permeation of ions and water through biological pores. *Phys. Biol.* 1:42-52.
10. Corry, B. 2006. An energy-efficient gating mechanism in the acetylcholine receptor channel suggested by molecular and brownian dynamics. *Biophys. J.* 90:799-810.
11. Wan, R., J. Li, H. Lu, and H. Fang. 2005. Controllable water channel gating of nanometer dimensions. *J. Am. Chem. Soc.* 127:7166-7170.
12. Hummer, G., J. C. Rasaiah, and J. P. Noworyta. 2001. Water conduction through the hydrophobic channel of a carbon nanotube. *Nature*. 414:188-190.
13. Levina, N., S. Totemeyer, N. R. Stokes, P. Louis, M. A. Jones, and I. R. Booth. 1999. Protection of *Escherichia coli* cells against extreme turgor by activation of MscS and MscL mechanosensitive channels: Identification of genes required for MscS activity. *EMBO J.* 18:1730-1737.
14. Martinac, B., M. Buechner, A. H. Delcour, J. Adler, and C. Kung. 1987. Pressure-sensitive ion channel in *Escherichia coli*. *Proc. Natl. Acad. Sci. USA*. 84:2297-2301.
15. Hamill, O. P., and B. Martinac. 2001. Molecular basis of mechanotransduction in living cells. *Physiol. Rev.* 81:685-740.
16. Kloda, A., and B. Martinac. 2002. Mechanosensitive channels of bacteria and archaea share a common ancestral origin. *Eur. Biophys. J.* 31:14-25.
17. Pivetti, C. D., M. R. Yen, S. Miller, W. Busch, Y. H. Tseng, I. R. Booth, and M. H. Saier, Jr. 2003. Two families of mechanosensitive channel proteins. *Microbiol. Mol. Biol. Rev.* 67:66-85.
18. Haswell, E. S., and E. M. Meyerowitz. 2006. MscS-like proteins control plastid size and shape in *Arabidopsis thaliana*. *Curr. Biol.* 16:1-11.

19. Akitake, B., A. Anishkin, and S. Sukharev. 2005. The "dashpot" mechanism of stretch-dependent gating in MscS. *J. Gen. Physiol.* 125:143-154.
20. Long, S. B., E. B. Campbell, and R. MacKinnon. 2005. Voltage sensor of Kv1.2: Structural basis of electromechanical coupling. *Science.* 309:903-908.
21. Booth, I. R., M. D. Edwards, and S. Miller. 2003. Bacterial ion channels. *Biochemistry.* 42:10045-10053.
22. Long, S. B., E. B. Campbell, and R. MacKinnon. 2005. Crystal structure of a mammalian voltage-dependent Shaker family K⁺ channel. *Science.* 309:897-903.
23. Bass, R. B., P. Strop, M. Barclay, and D. C. Rees. 2002. Crystal structure of *Escherichia coli* MscS, a voltage-modulated and mechanosensitive channel. *Science.* 298:1582-1587.
24. Elmore, D. E., and D. A. Dougherty. 2001. Molecular dynamics simulations of wild-type and mutant forms of the *Mycobacterium tuberculosis* MscL channel. *Biophys. J.* 81:1345-1359.
25. Elmore, D. E., and D. A. Dougherty. 2003. Investigating lipid composition effects on the mechanosensitive channel of large conductance (MscL) using molecular dynamics simulations. *Biophys. J.* 85:1512-1524.
26. Anishkin, A., and S. Sukharev. 2004. Water dynamics and dewetting transitions in the small mechanosensitive channel MscS. *Biophys. J.* 86:2883-2895.
27. Sotomayor, M., and K. Schulten. 2004. Molecular dynamics study of gating in the mechanosensitive channel of small conductance MscS. *Biophys. J.* 87:3050-3065.
28. Chanda, B., O. K. Asamoah, R. Blunck, B. Roux, and F. Bezanilla. 2005. Gating charge displacement in voltage-gated ion channels involves limited transmembrane movement. *Nature.* 436:852-856.
29. Cuello, L. G., D. M. Cortes, and E. Perozo. 2004. Molecular architecture of the KvAP voltage-dependent K⁺ channel in a lipid bilayer. *Science.* 306:491-495.
30. MacKinnon, R. 2004. Voltage sensor meets lipid membrane. *Science.* 306:1304-1305.
31. Posson, D. J., P. H. Ge, C. Miller, F. Bezanilla, and P. R. Selvin. 2005. Small vertical movement of a K⁺ channel voltage sensor measured with luminescence energy transfer. *Nature.* 436:848-851.
32. Kashket, E. R. 1985. The proton motive force in bacteria—a critical-assessment of methods. *Annu. Rev. Microbiol.* 39:219-242.

33. Bostick, D., and M. L. Berkowitz. 2003. The implementation of slab geometry for membrane-channel molecular dynamics simulations. *Biophys. J.* 85:97-107.
34. Aksimentiev, A., and K. Schulten. 2005. Imaging alpha-hemolysin with molecular dynamics: ionic conductance, osmotic permeability, and the electrostatic potential map. *Biophys. J.* 88:3745-3761.
35. Crozier, P. S., D. Henderson, R. L. Rowley, and D. D. Busath. 2001. Model channel ion currents in NaCl-extended simple point charge water solution with applied-field molecular dynamics. *Biophys. J.* 81:3077-3089.
36. Chandrasekhar, J., D. C. Spellmeyer, and W. L. Jorgensen. 1984. Energy component analysis for dilute aqueous-solutions of Li⁺, Na⁺, F⁻, and Cl⁻ ions. *J. Am. Chem. Soc.* 106:903-910.
37. Lu, J., and M. E. Green. 1997. Simulation of water in a pore with charges: Application to a gating mechanism for ion channels. *Progr. Colloid Polym. Sci.* 103:121-129.
38. Harvey, S. C. 1989. Treatment of electrostatic effects in macromolecular modeling. *Proteins.* 5:78-92.
39. Gullingsrud, J., D. Kosztin, and K. Schulten. 2001. Structural determinants of MscL gating studied by molecular dynamics simulations. *Biophys. J.* 80:2074-2081.
40. Tieleman, D. P., H. J. Berendsen, and M. S. Sansom. 2001. Voltage-dependent insertion of alamethicin at phospholipid/water and octane/water interfaces. *Biophys. J.* 80:331-346.
41. Ramakrishnan, V., D. Henderson, and D. D. Busath. 2004. Applied field nonequilibrium molecular dynamics simulations of ion exit from a beta-barrel model of the L-type calcium channel. *Biochim. Biophys. Acta.* 1664:1-8.
42. Faraldo-Gomez, J. D., G. R. Smith, and M. S. Sansom. 2002. Setting up and optimization of membrane protein simulations. *Eur. Biophys. J.* 31:217-227.
43. Essmann, U., L. Perera, M. L. Berkowitz, T. Darden, H. Lee, and L. G. Pedersen. 1995. A smooth particle mesh Ewald method. *J. Chem. Phys.* 103:8577-8593.
44. Berendsen, H. J. C., D. Vandespoel, and R. Vandrunen. 1995. Gromacs—A message-passing parallel molecular-dynamics implementation. *Comput. Phys. Comm.* 91:43-56.
45. Lindahl, E., B. Hess, and D. van der Spoel. 2001. GROMACS 3.0: A package for molecular simulation and trajectory analysis. *J. Mol. Mod.* 7:306-317.

46. Berger, O., O. Edholm, and F. Jahnig. 1997. Molecular dynamics simulations of a fluid bilayer of dipalmitoylphosphatidylcholine at full hydration, constant pressure, and constant temperature. *Biophys. J.* 72:2002-2013.
47. Berendsen, H. J. C., J. P. M. Postma, W. F. Vangunsteren, A. Dinola, and J. R. Haak. 1984. Molecular-dynamics with coupling to an external bath. *J. Chem. Phys.* 81:3684-3690.
48. Israelachvili, J. 1991. *Intermolecular & Surface Forces, Second Edition*. London: Academic Press.
49. Smart, O. S., J. Breed, G. R. Smith, and M. S. Sansom. 1997. A novel method for structure-based prediction of ion channel conductance properties. *Biophys. J.* 72:1109-1126.
50. Humphrey, W., A. Dalke, and K. Schulten. 1996. VMD: Visual molecular dynamics. *J. Mol. Graph.* 14:33-38.

Chapter 2

The Delivery of tRNA to Cultured Mammalian Cells Mediated by Peptide Transduction Domains

Abstract

In vivo incorporation of unnatural amino acids using nonsense suppression is a powerful technique to study proteins. However, one challenge to the method is that the amount of unnatural protein that can be produced is directly limited by the amount of unnatural aminoacyl-tRNA presented to the cellular translation machinery. Therefore, the success of this technique depends heavily on the ability to deliver aminoacyl-tRNA, which is produced *in vitro*, into cells. Currently, the most commonly used system involves injection of a *Xenopus* oocyte. It is desirable to transfer the technology to a mammalian expression system, but because mammalian cells are so much smaller than oocytes, injection is not a practical delivery method, so other techniques must be utilized. An intriguing possibility is the use of protein transduction domains (PTDs), small peptides that greatly enhance the internalization of extracellular material. Several PTD-based approaches for tRNA delivery were attempted: covalent ligation of tRNA to a PTD, noncovalent complexation of tRNA and PTDs, and production of a fusion protein containing a PTD and a tRNA-binding domain. However, none of these methods was useful in delivering tRNA into mammalian cells in culture.

INTRODUCTION

Unnatural Amino Acid Incorporation by Nonsense Suppression

Proteins are the workhorses of the cell. This class of biological macromolecules is involved in essentially every process necessary to sustain life [1]. Given the incredible diversity of protein functions, it is remarkable that practically all proteins in all forms of life are built from a set of just twenty amino acids. Within each protein, specific residues play important roles, giving the protein the characteristics required to carry out its function [2]. Obtaining a detailed understanding of a protein's operation as a molecular machine depends heavily on the elucidation of its important residues and the roles that they perform.

A common method for studying proteins involves mutating particular residues to other amino acids and determining how the change affects protein function. This technique can provide a wealth of information about the involvement of the residues in intra- and intermolecular binding and recognition interactions as well as the catalytic mechanisms of enzymes. With the discovery of the genetic code, the site-specific mutation of one amino acid to another has become a straightforward process. However, conventional mutagenesis techniques are limited to the set of twenty natural amino acids, which provide a relatively narrow range of chemical functionalities.

To overcome this limitation, a technique for incorporating unnatural amino acids has been developed to expand the set of amino acids available for mutagenesis beyond the natural twenty [3]. A wide variety of amino acids, subtly or drastically different from the natural amino acids, have been site-specifically incorporated into proteins, which has

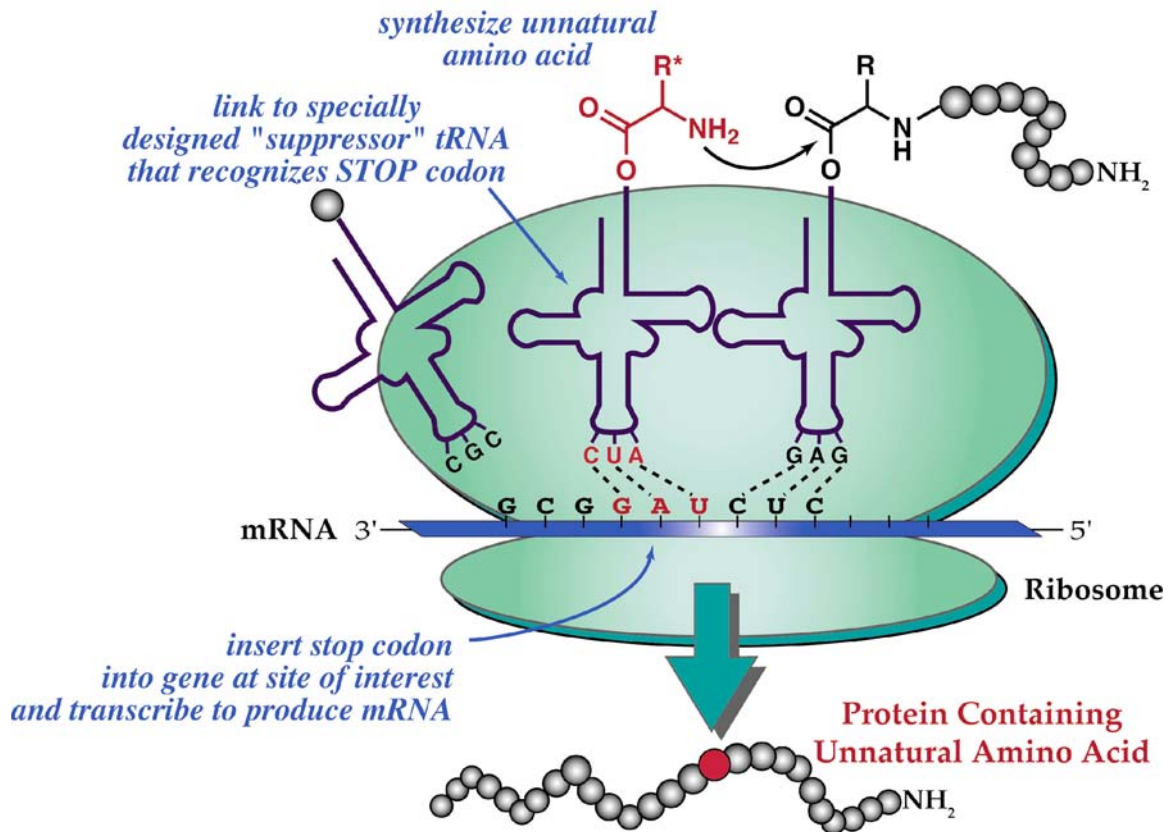


Fig. 2.1. The nonsense suppression method for unnatural amino acid incorporation.

opened the door to a whole world of new experiments. Proteins can be studied in much finer detail, and proteins with novel properties can be generated [4–8].

The technique takes advantage of the phenomenon known as nonsense suppression, in which a codon that ordinarily is noncoding is manipulated and used to incorporate a unique amino acid (fig. 2.1) [9, 10]. The site of interest within the gene is mutated to a stop codon, which normally signals for the termination of translation and has no cognate tRNA molecules. In addition, the desired unnatural amino acid is chemically ligated to a specially designed suppressor tRNA containing the stop anticodon. The mutated gene and the suppressor tRNA are presented to the cellular translational machinery, either *in vivo* or *in vitro*. The synthesis of the protein proceeds normally at

first, but when the machinery reaches the stop codon that has been inserted into the gene, instead of terminating translation, it binds the suppressor tRNA and appends the unnatural amino acid to the nascent polypeptide chain. The rest of the polypeptide is then synthesized normally, producing a full-length protein with the unnatural residue at the desired site.

An important challenge in the production of unnatural proteins by this method is the fact that the unnatural aminoacyl-tRNA is a stoichiometric reagent. Because the aminoacyl-tRNA is not regenerated, the number of proteins that can be produced is directly limited by the number of aminoacyl-tRNA molecules delivered to the system. Therefore, this technique hinges on the ability to deliver sufficient amounts of tRNA to the ribosomes. Until recently, the only *in vivo* expression system that could be used to generate and study unnatural proteins was the oocyte of *Xenopus laevis* [11, 12]. Its large size allows for easy tRNA delivery by injection through the membrane.

Although in many cases the *Xenopus* oocyte system works well, there are clear benefits to transferring this technology to a mammalian cell expression system. Many of the proteins that have been studied with unnatural amino acids are ion channels of mammalian origin. Several of these channels do not express well in oocytes, and it is likely that their expression could be improved in a more native environment. Furthermore, expression in mammalian cells will allow for studies on signaling pathways that are absent in oocytes. However, progress on developing a mammalian cell expression system for unnatural proteins has been slow, because mammalian cells (~10 μm in diameter) are so much smaller than oocytes (~1 mm in diameter), making it much more difficult to deliver enough tRNA to produce a detectable amount of protein.

Our lab has only recently developed the methodology for generating unnatural proteins in mammalian cells [13]. Electroporation was chosen from a number of transfection techniques as the most suitable method for delivering the mutated mRNA and suppressor tRNA to the cells. Although this technique works reasonably well, other methods should be explored to improve the delivery of tRNA, and as a result, produce more protein.

Protein Transduction Domains

An intriguing possibility is the use of protein transduction domains (PTDs) as delivery agents for tRNA. PTDs, also known as cell-permeable peptides or CPPs, are relatively short peptides, ranging from 7 to ~40 residues in length, that have the capability to cross through biological membranes [14–17]. At least twenty distinct sequences from natural proteins have been discovered to have PTD properties, and many derivatives of these have been developed. The best characterized include the PTDs from the Antennapedia homeoprotein from *Drosophila* (Antp or penetratin) [18] and the HIV-1 transactivator of transcription (Tat) [19].

Amazingly, the peptides can confer their translocation properties to other molecules. Conjugation or tight noncovalent association of PTDs to other molecules or molecular assemblies facilitates the delivery of the full cargo into the cytoplasm. The diverse range of the cargo that PTDs have delivered includes other peptides [20, 21], fluorophores and drugs [22, 23], full-length proteins [24–26], DNA and peptide nucleic acids [27–29], magnetic nanoparticles [30], and intact liposomes [31]. Thus, PTDs

Table 2.1. Primary sequences of selected PTDs.

PTD	Sequence^a
Antp	RQIKIWFQNRRMKWKK
Tat	YGRKKRRQRR
MPG ^b	Ac-GALFLGFLGAAGSTMGAWSQPKSKRKKV-Cya

^a Basic residues are shown in blue to highlight their abundance. ^b MPG has an acetyl group (Ac) at its N-terminus and a cysteamide residue (Cya) at its C-terminus.

appear to act as nonspecific delivery agents, and the mechanism of the uptake of PTDs into cells has been an area of intense research.

Other than the fact that PTDs generally contain many basic and hydrophobic residues, they do not have any obvious sequence or structural similarity, as shown by the examples in table 2.1, which contains the sequences of the PTDs that were used in this study. Initial experiments indicated that PTDs were able to cross membranes rapidly in an energy-independent, receptor-independent, and nonendocytotic manner. However, more recent work has demonstrated that most of these assertions were based on artifactual results [32–36]. The current leading hypothesis on the translocation of PTDs involves tight, nonspecific binding of the PTD to the cell surface phospholipids and polysaccharides through electrostatic interactions, followed by endocytosis and release from the endosomes into the cytoplasm or nucleus. There is still debate on the precise details, however, and it is possible that in some cases, PTDs may actually traverse the membrane via a nonendocytotic mechanism [36–38].

PTDs are an attractive option for efficient delivery of unnatural aminoacyl-tRNA into mammalian cells. There are several PTD-based approaches for tRNA delivery: covalent ligation of a PTD to a tRNA molecule, the formation of large noncovalently associated PTD/tRNA complexes, and the generation of a fusion protein consisting of a

tRNA-binding domain linked to a PTD. There are no reports of tRNA delivery with PTDs in the literature, so all of these options were explored to determine which, if any, is the most viable method.

RESULTS AND DISCUSSION

Covalent Ligation

The most straightforward methodology for employing PTDs to transfect mammalian cells with tRNA involved forming covalently linked conjugates. Although this approach has not been previously reported for RNA delivery, covalently linked conjugates with DNA have been used several times [27, 28]. Conjugation requires the presence of reactive groups on both the PTD and the cargo molecule. As short peptides, PTDs can be easily generated by solid-phase synthesis, which allows for a wide variety of reactive groups to be appended to the peptide chain. Similarly, short oligonucleotides can be prepared by solid-phase techniques with an appropriate chemical group. Many peptide-DNA conjugates have been made by reacting the two molecules prepared in this manner [39]. To date, the largest DNA strand that has been conjugated to a PTD is 55 nucleotides in length [40]. However, for larger nucleic acids, such as plasmids, full-length mRNA transcripts, or tRNA molecules, solid-phase synthesis is inefficient and prohibitively expensive. It is much easier to generate them by biochemical means, but this method does not allow for the incorporation of any chemically reactive groups that could be used for conjugation. Consequently, there are very few strategies for the chemical modification of nucleic acids.

One possibility that was considered for modifying a biochemically produced tRNA transcript involved successive treatment of the tRNA with alkaline phosphatase, to remove the 5' phosphates, and polynucleotide kinase with ATP- γ -S, to append a thiophosphate to the 5' end of the tRNA [41]. If the thiophosphate has chemical properties similar to thiols, it will be capable of reacting with a maleimide group attached to a PTD.

The reaction of the thiophosphate-modified tRNA (tRNA-5'-S) with a PTD-maleimide was attempted, but was not successful in forming a covalent linkage between the two molecules [42]. There are at least two possible explanations for the failure of this reaction: (1) nonspecific association through electrostatic interactions of the highly negative tRNA and the positive PTDs prevented the reactive groups from coming into contact, or (2) thiophosphates are not very reactive towards maleimides at the concentrations used in our preparations.

Explanation (1) was previously explored and found to be unlikely, for several reasons. First, the formation of the conjugate was not enhanced by the presence of a high salt concentration in the buffer. Ionic screening of the interactions between the tRNA and PTD should have decreased the amount of nonspecific binding. Second, the use of Tat-4, a Tat analogue containing only 3 basic residues (instead of 7 on Antp, for example) did not improve the formation of the conjugate [42].

However, explanation (2) remained to be tested. Thiophosphates of mono- or dinucleotides at concentrations of ~ 10 mM have been shown to be at least modestly reactive towards maleimide reagents [43–45], but there is much less data for lower concentrations, such as those in the range of 1–10 μ M that can be produced for

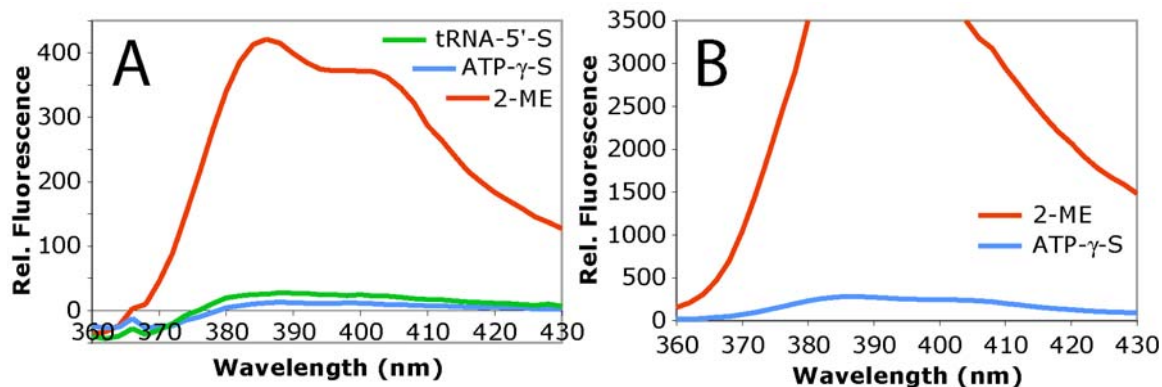


Fig. 2.2. Emission spectra showing the fluorescence of PM after reaction with various thiol or thiophosphate compounds, relative to the fluorescence of PM alone. *A*, 5 μM thiol/thiophosphate and 50 μM PM. At wavelengths less than 375 nm, there were strange peaks in the raw data, which seemed to be related to the plate itself. The fluorescence of the unreacted PM solution had an unusually large peak there, which caused the relative fluorescence curves shown here to dip below zero. Despite this, the peak PM fluorescence is obvious at 386 nm. *B*, 12.9 μM thiol/thiophosphate and 50 μM PM. The fluorescence of the 2-ME solution saturated the detector.

tRNA-5'-S. Therefore, the hypothesis that thiophosphates at low concentrations do not react efficiently with maleimides was explored by using N-(1-pyrenyl)maleimide (PM) as a probe molecule. PM is nonfluorescent unless a thiol or thiophosphate reacts with the maleimide moiety.

The reactivity of tRNA-5'-S with PM was measured by monitoring the PM fluorescence. 5 μM of tRNA-5'-S, ATP- γ -S, and 2-mercaptoethanol (2-ME) were incubated with 50 μM PM, and the fluorescence emission spectrum for each reaction mixture was obtained after 27 hours (fig. 2.2A). The 2-ME reacted very well with PM, but reaction of the thiophosphate compounds could not be detected.

The concentration of the thiol/thiophosphate compounds was increased to 12.9 μM , which is near to the highest practical concentration of tRNA-5'-S that can be produced by PNK treatment and dialysis. This experiment did not include tRNA-5'-S because there was not enough material to make such a highly concentrated solution. It is

clear there is some reactivity of the thiophosphate of ATP- γ -S with the PM (fig. 2.2B), but it is approximately an order of magnitude less than that of the thiol of 2-ME, which saturated the detector at this concentration.

Therefore, generating a 5'-thiophosphate by AP and PNK treatment of the tRNA failed to provide a reactive chemical handle for linkage to PTDs. This result, together with the fact that linking a PTD to any nucleic acid produced biochemically has never been reported in the literature, leads to the conclusion that the formation of a covalently linked PTD-tRNA conjugate is particularly difficult and is not a practical option for tRNA delivery.

Noncovalent Delivery Complexes

Because of the difficulty in preparing covalently linked PTD-tRNA conjugates, the method of tRNA delivery by noncovalent complexation with PTDs was explored. This method was used in the only report of RNA delivery with a PTD to date. Divita and co-workers used the 21-residue peptide MPG to transport plasmid DNA as well as mRNA into the nuclei of living cells [46]. Based on this work, MPG was chosen for study in our system.

MPG was prepared by solid-phase synthesis. HPLC and MS analysis indicated that the final product was very pure and had the desired mass (fig. 2.3).

Complexation of MPG with Nucleic Acids

The tryptophan fluorescence of MPG can be used to monitor its complexation with nucleic acids [47, 48]. Plasmid DNA binds MPG with a relatively high affinity,

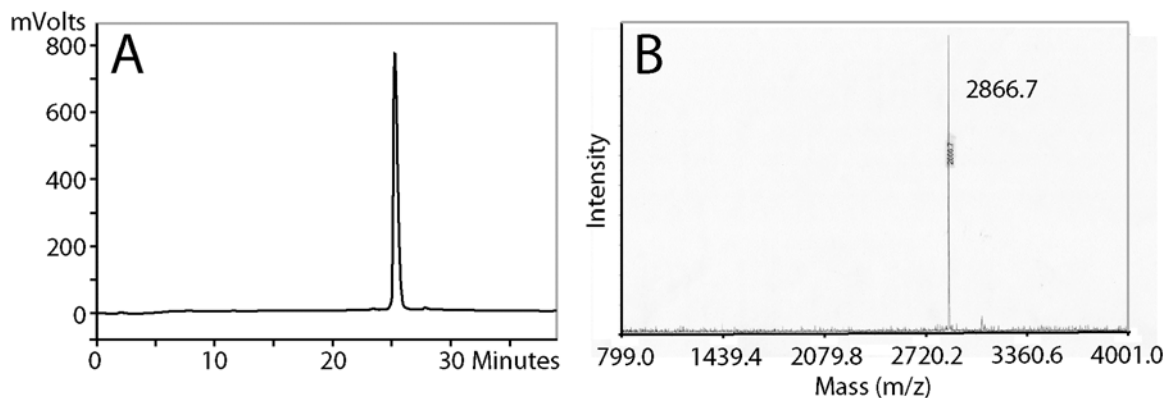


Fig. 2.3. HPLC trace (A) and MS (B) of MPG prepared by solid-phase synthesis, indicating the purity of the product. The MS peak was expected to be 2867.4, indicating that the desired product was synthesized.

quenching the fluorescence of MPG by up to 30%. In experiments with 10 μM MPG, only 0.5 nM DNA was required for 15% quenching (half of the full reduction of fluorescence), and 2 nM DNA was sufficient for maximal quenching. As a first step in our work with MPG, we attempted to reproduce this work.

Two different plasmids—pTAT (2955 bp) and pCS2 containing an EGFP gene (~4800 bp)—were used. Solutions containing 10 μM MPG were incubated in buffer containing DNA at concentrations ranging from 0 to 19.2 μM , which should have been more than enough to fully quench the MPG fluorescence, according to the previous work.

Surprisingly, we could not reproduce the previous results. The MPG fluorescence decreased only slightly with the addition of DNA (fig. 2.4A), even at the highest concentration, and this was quite possibly due to photobleaching of the fluorophore. There was no indication that the DNA and MPG were forming noncovalent complexes.

Because it contains a cysteamide moiety (table 2.1), MPG may form covalently linked homodimers under oxidizing conditions that may interfere with its binding to DNA. The above experiment was repeated for pTAT in solutions with and without

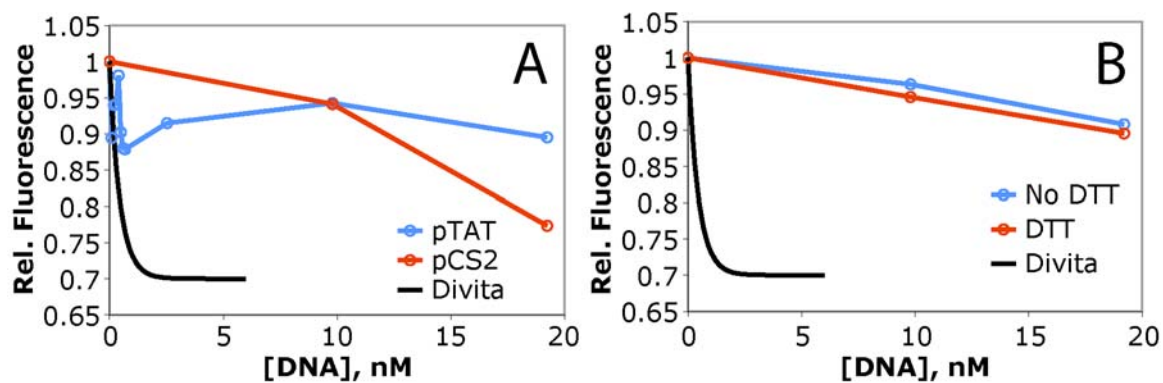


Fig. 2.4. Fluorescence quenching of 10 μM MPG due to complexation with plasmid DNA. The black curves approximate the data reported by Divita and co-workers [47]. *A*, Fluorescence quenching with two different plasmids. *B*, Fluorescence quenching by pTAT with and without 30 μM DTT.

30 μM dithiothreitol (DTT) to prevent the formation of disulfide bonds. However, the presence of DTT had no influence on the fluorescence quenching (fig. 2.4B).

It is unclear why our results differed so significantly from those seen previously. Despite this, we proceeded with experiments attempting to use noncovalent complexes with MPG to deliver both plasmid DNA and tRNA to living cells.

Optimization of Cell Culture Conditions

Because of the cost of generating peptide by solid-phase synthesis, it is important to develop an experimental system that minimizes the amount of the peptide required for application to cultured mammalian cells. Even in the smallest commonly used culture dishes, which are 35 mm in diameter, the amount of medium necessary to maintain healthy cells is ~ 3 mL. Given that MPG experiments required concentrations of ~ 100 μM , if we were to use these dishes, the amount of MPG needed would be on the order of 1 mg per dish, which is excessive. Therefore, we sought a culture system that

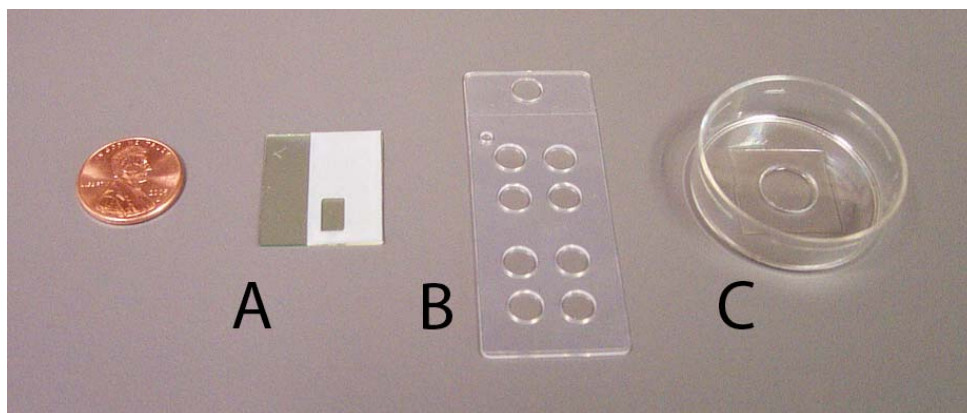


Fig. 2.5. The three small-well containers used to grow cells. *A*, Epizap slide, consisting of a glass cover slip coated with an indium-tin oxide alloy and a Teflon cover that surrounds a 4 x 7 mm rectangular well. *B*, CultureWell slide, consisting of a glass slide covered with a silicone gasket that surrounds eight wells, each with a diameter of 5 mm. *C*, MatTek glass-bottom dish, consisting of a 35 mm culture dish with a 10 mm hole. A glass cover slip is mounted at the bottom of the hole. The penny is shown for scale.

allowed for the growth of cells in tiny wells, on the order of 30 μL instead of 3 mL, requiring only 10 μg of MPG per well.

Possibilities for an appropriate culture system included Epizap slides, CultureWell slides, and MatTek glass-bottom dishes (fig. 2.5), all of which contain wells that can be fully covered with 50 μL or less of medium. To determine the ideal system, CHO-K1 cells were cultured in each type of container, and after 24–48 hours of growth, visualized to determine which had the healthiest appearance.

The best system was found to be the MatTek dishes. The cells on the glass cover slip inside the well grew nicely and remained healthy (fig. 2.6A).

The cells on the Epizap slides also remained generally healthy (fig. 2.6B), although often their health was noticeably compromised compared to those in the MatTek dishes, as noted previously [42]. These slides were designed specifically for use with the Epizap electroporation system, which transfects cells with DNA from the bath solution

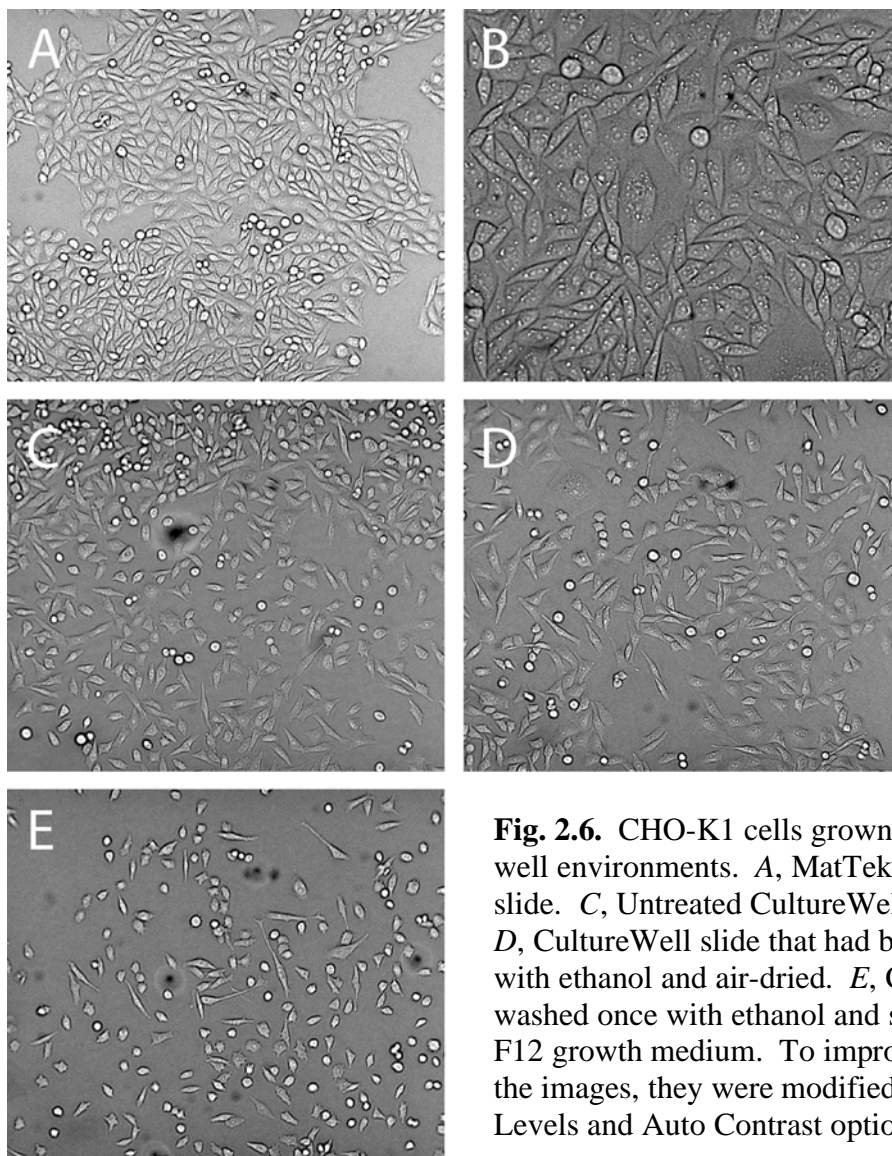


Fig. 2.6. CHO-K1 cells grown in different small-well environments. *A*, MatTek dish. *B*, Epizap slide. *C*, Untreated CultureWell slide. *D*, CultureWell slide that had been washed once with ethanol and air-dried. *E*, CultureWell slide washed once with ethanol and several times with F12 growth medium. To improve the quality of the images, they were modified with the Auto Levels and Auto Contrast options in Photoshop.

by the application of electrical pulses, and as such, were required in all the experiments in which the cells were subjected to the Epizap protocol. The probable cause of the slight decrease in health was the coating of indium-tin oxide on the slides, used because the slide itself is one of the electrodes for electroporation.

The CultureWell slides provided the harshest environment. Many cells in the wells died, and even those that looked healthy did not appear to be dividing, as they were all spaced relatively far apart (fig. 2.6C–E). Often, this was true even when cells that

were in the bottom of the dish outside of the wells looked reasonably healthy, indicating that the environment inside the wells was itself detrimental to the cells. The slides were also subjected to different sterilization treatments before the addition of cells in order to determine if this would improve cell health. Some slides were rinsed in ethanol and allowed to air dry in the laminar flow hood overnight, and some were rinsed once in ethanol and several times in growth medium. None of these treatments had any effect on cellular health. The poor health was unexpected, because these slides were specifically developed to culture mammalian cells in small volume compartments.

Therefore, in most experiments that did not require electroporation, MatTek dishes were used. When electroporation was required and in a few other early experiments, the Epizap slides were used.

Because the purpose of the small-well containers was to minimize the amount of solution the cells needed to survive, it was important to make sure that the wells of the MatTek dishes provided a healthy environment for the cells even when covered with a small amount of medium. Therefore, cells growing in a MatTek dish were subjected to conditions they were likely to encounter during experiments with MPG, and their health was monitored. CHO-K1 cells were cultured in a MatTek dish for 2 days in a normal amount of F12 growth medium (2 mL). The growth medium was removed from the dish, and only 30 μ L of serum-free F12 was applied to the well. The cells were incubated for an hour before 2 mL of fresh F12 growth medium was added to the dish. From visual inspection, it was clear that the health of the cells in the well was not compromised by this procedure. They remained healthy throughout the low-volume incubation and were still healthy 24 hours later.

Finally, it was important to optimize the seeding conditions for the cell cultures. Using too many seed cells would cause the culture to become overgrown and unhealthy, while using too few would reduce transfection efficiency. Therefore, different numbers of CHO-K1 and HEK293 cells were used to seed cultures in MatTek dishes, and the culture densities were observed after 72–96 hours of growth. The optimal seeding numbers were found to be 2×10^5 and 1×10^5 cells for CHO-K1 and HEK293 cells, respectively. Therefore, these numbers of cells were used to seed cultures for subsequent experiments.

Experiments with peptides began once the cell culture conditions were optimized.

DNA Delivery by MPG

Previous work has demonstrated that the application of MPG/DNA complexes is an effective technique for transfection of many types of mammalian cells [46–49]. The transfection procedure consisted simply of the preincubation of MPG with plasmid in a charge ratio of 5/1 (positive charges to negative charges) and addition to cells in culture, which resulted in robust expression of the gene on the plasmid [47].

Our experiments utilized a wild-type EGFP reporter gene inserted into the pCS2 plasmid (wt-EGFP DNA). Solutions of 100 μ M MPG with 6.25, 12.5, 25, or 50 nM DNA (charge ratios of 2.2/1, 4.4/1, 8.9/1, and 17.8/1) were prepared in serum-free F12. The solutions were incubated for 10 minutes and applied to CHO-K1 cells for 60 minutes before dilution in F12 growth medium. The cells were imaged by fluorescence microscopy 24–48 hours later.

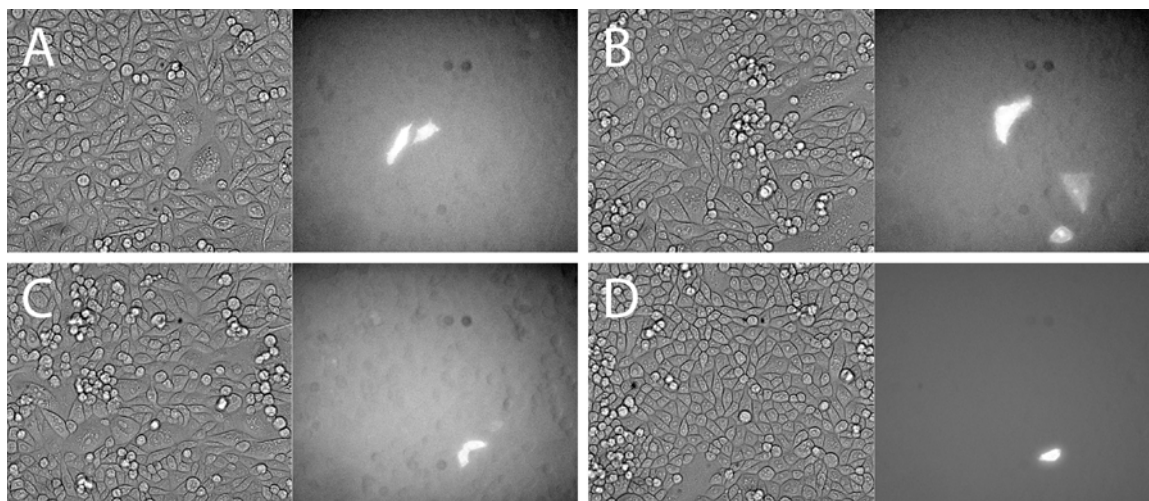


Fig. 2.7. CHO-K1 cells treated with solutions containing MPG and wt-EGFP DNA. The MPG/DNA ratios were 100 μ M/25 nM (4.4/1 charge ratio) (A–B) and 100 μ M/12.5 nM (8.9/1 charge ratio) (C–D). Corresponding bright field and fluorescent images are paired. Exposure times for the fluorescent images were 1 s (A–B), 4 s (C), or 0.5 s (D). To improve the quality of the images, they were modified with the Auto Levels and Auto Contrast options in Photoshop.

The cells remained healthy throughout the experiment, indicating that 100 μ M MPG is not toxic, in agreement with previous work. Although a few cells expressed EGFP, the vast majority did not (fig. 2.7). Thorough inspection of all the cultures revealed that of the thousands of cells, just 11 were fluorescent. Eight were from the 4.4/1 sample (fig. 2.7A–B), three were from the 8.9/1 sample (fig. 2.7C–D), and no fluorescent cells were found in either the 2.2/1 or 17.8/1 sample. However, given the extremely low efficiency of transfection, the numbers of fluorescent cells cannot be meaningfully compared. Subsequent attempts of this experiment confirmed these results, which suggests that contrary to previous reports, transfection by MPG is not efficient at all. In fact, it is quite possible that a mechanism completely independent of MPG resulted in the very limited uptake of plasmid DNA into the cells.

Other DNA Delivery Techniques

Although MPG failed as a delivery vector for plasmid DNA, it was still possible that it could be used to deliver tRNA. Compared to plasmid DNA, tRNA is much smaller and has a very different three-dimensional structure. However, testing this hypothesis required a suitable method to deliver DNA. Many methods exist for transfecting cultured cells, including electroporation and transfection reagents, both of which were tried. Specifically, the Epizap electroporation system was used because it is compatible with the small volume wells necessary for the peptide experiments, and PolyFect Transfection Reagent (PF) was used because it was specifically designed for transfection of common cell lines such as CHO and HEK293.

Transfection of CHO-K1 cells with wt-EGFP DNA was performed with both Epizap and PF, and transfection of HEK293 cells was also performed with PF. Fluorescence microscopy was used to determine the percentage of fluorescent cells, indicating how effectively each technique delivered DNA. In general, Epizap led to high transfection efficiencies (~50%; fig. 2.8A) but often resulted in high cell death. Previous work in our lab has shown that attempts to optimize the electroporation conditions did not significantly improve the health of the cells [42].

In contrast, PF generally led to healthier cells but lower transfection efficiencies (~12% in CHO-K1, ~40% in HEK293; fig. 2.8B–C). We performed experiments to optimize the amount of PF and the amount of DNA in CHO-K1 cells. First, transfection was performed with different amounts of PF and DNA such that the ratio of the two reagents remained nearly the same: 3 μ L PF/0.5 μ g DNA, 10/1.5, 30/5, and 60/10 (fig. 2.9). Exposure to 30 or 60 μ L PF killed all of the cells, and the transfection

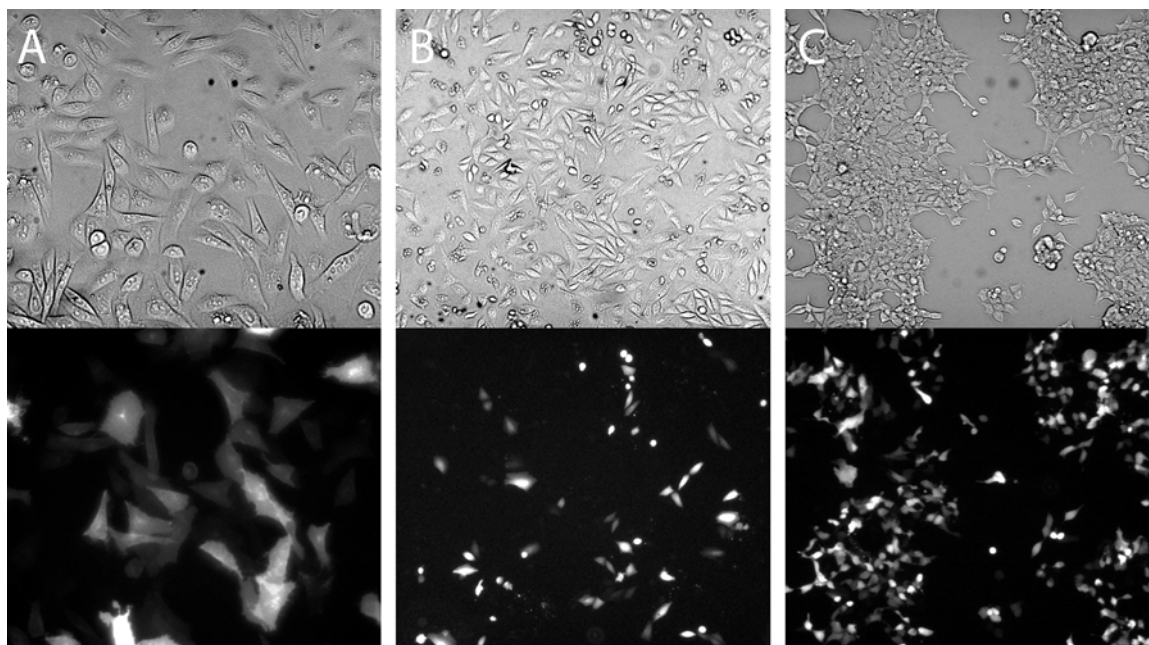


Fig. 2.8. Transfection efficiency for Epizap in CHO-K1 (A) and PolyFect in CHO-K1 (B) and HEK293 cells (C). Corresponding bright field and fluorescent images are paired. Exposure times for fluorescent images were 1 s (A), 0.5 s (B), or 0.3 s (C). To improve the quality of the images, they were modified with the Auto Levels and Auto Contrast options in Photoshop.

efficiency with 3 μL PF was lower than that with 10 μL PF. Second, transfection was performed with 10 μL PF and 0.75, 1.5, 3.0, or 5.0 μg DNA (fig. 2.10). The efficiency was highest for the cells that received 1.5 and 3.0 μg DNA (fig. 2.10B–C). These results confirmed that the manufacturer recommendations (10 μL PF and 1.5 μg DNA) were the best for transfection in our system, and therefore these amounts were used in further experiments that utilized PF for transfection.

Because neither of these methods was significantly better than the other in both preservation of cell health and transfection efficiency, both of them were used to deliver DNA in MPG/tRNA delivery experiments.

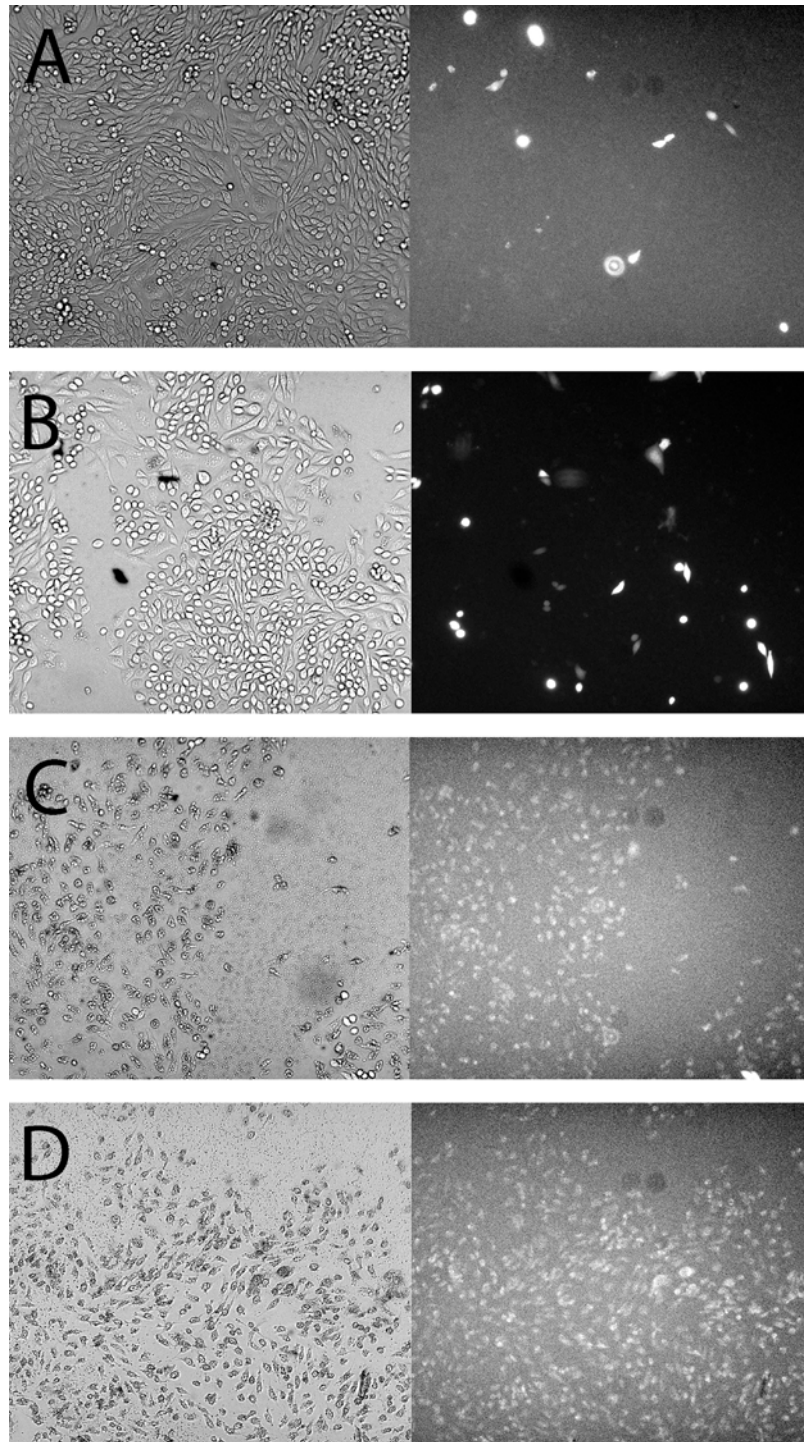


Fig. 2.9. Expression of EGFP in CHO-K1 cells transfected using different amounts of PF and wt-EGFP DNA. PF/DNA ratios (in $\mu\text{L}/\mu\text{g}$) were 3/0.5 (A), 10/1.5 (B), 30/5.0 (C), and 60/10.0 (D). The cells in C and D are all dead. Corresponding bright field and fluorescent images are paired. Exposure times for all fluorescent images were 2 s. To improve the quality of the images, they were modified with the Auto Levels and Auto Contrast options in Photoshop.

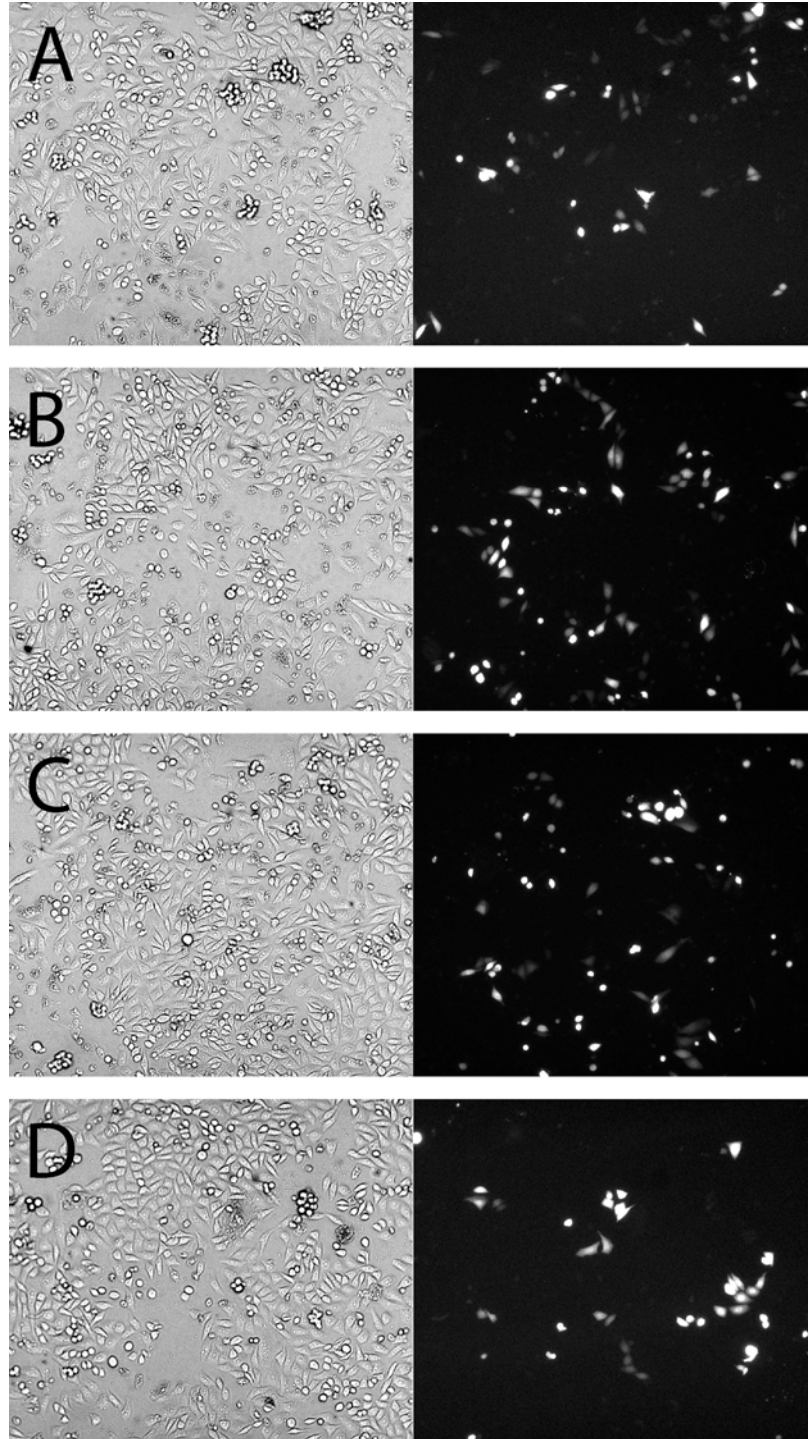


Fig. 2.10. Expression of EGFP in CHO-K1 cells transfected using 10 μ L PF and 0.75 (A), 1.5 (B), 3.0 (C), or 5.0 μ g wt-EGFP DNA (D). Corresponding bright field and fluorescent images are paired. Exposure times for all fluorescent images were 0.5 s. To improve the quality of the images, they were modified with the Auto Levels and Auto Contrast options in Photoshop.

MPG Delivery of tRNA

The assay to detect tRNA delivery into mammalian cells, previously developed in our lab, is outlined in fig. 2.11 [13]. It requires two components: an S29TAG-mutant EGFP gene, in which the amber stop codon (TAG) has replaced a serine codon, and the human serine amber suppressor (HSAS) tRNA [50]. HSAS is an unusual tRNA in that the anticodon was mutated to recognize the amber stop codon instead of its natural serine codon, but because seryl-tRNA synthetases do not use the anticodon as a recognition element, it can still be charged with serine like the natural tRNA^{Ser} molecules. Under normal circumstances, the translation of the S29TAG-EGFP gene would terminate at position 29 due to the TAG codon, and no fluorescent protein would be produced. However, HSAS can rescue expression of this gene because it is charged with serine but recognizes the TAG codon, thereby delivering the wild-type amino acid at position 29, resulting in a wild-type EGFP protein. Therefore, the presence of HSAS can be easily detected in cells expressing S29TAG-EGFP by fluorescence microscopy. Cells that contain HSAS are fluorescent, but those lacking HSAS are not.

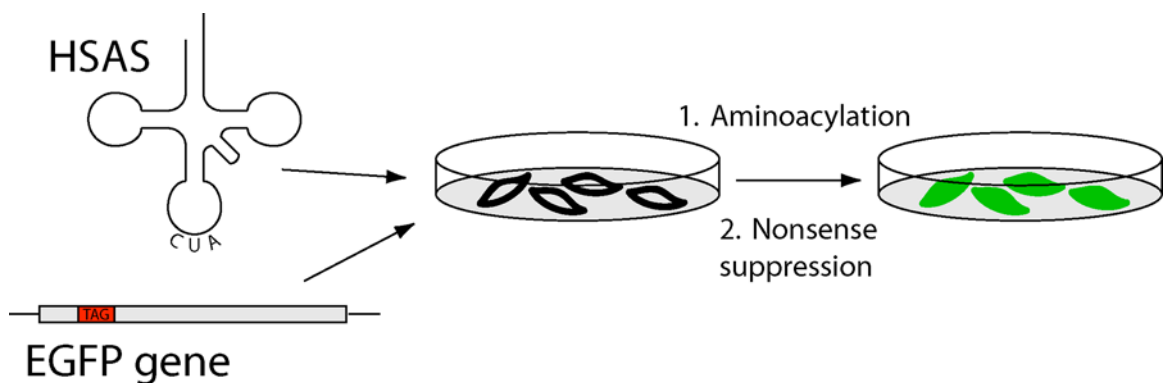


Fig. 2.11. The HSAS assay for tRNA delivery. Cells that contain a gene for a mutant EGFP with an internal TAG stop codon will not produce EGFP because the translation will terminate. However, if HSAS is delivered to the cells, aminoacylation by the endogenous synthetases and nonsense suppression at the TAG site will yield wild-type EGFP, detectable by fluorescence.

To determine if MPG could be used to deliver tRNA, cells were transfected with S29TAG-EGFP DNA using Epizap or PF, and MPG/HSAS complexes were applied ~24 hours later. 24–48 hours after HSAS application, the cells were observed for EGFP fluorescence. In contrast to the MPG/DNA complexation experiments, the initial results were somewhat promising. Transfection by Epizap was attempted first because it was able to deliver more DNA. CHO-K1 cells were transfected with S29TAG-EGFP, and precomplexed 51 μM MPG/0.5 μM HSAS (5/1 charge ratio) solution was applied to the cells. The application of the MPG and HSAS resulted in many fluorescent cells (fig. 2.12A–B), whereas the control samples missing one or both components had essentially no fluorescence (fig. 2.12C–E). This suggested that MPG effectively delivered HSAS into the cells.

Unfortunately, this result could not be reliably reproduced, because of the inconsistency of the cell health and transfection efficiency after Epizap treatment. No other attempts using Epizap transfection produced more than one or two healthy fluorescent cells.

Transfection with PF was then used because of the improvement in cell health with this technique. These experiments had the additional complication that the cells transfected with S29TAG-EGFP by PF remained healthy and produced small amounts of EGFP without HSAS. This occurred by a process known as readthrough, in which the translational machinery occasionally skipped over the TAG codon or erroneously inserted another amino acid instead of terminating the translation. When MPG/HSAS complexes were applied to the cells, there was obvious fluorescence (fig. 2.13A–B), but it was never significantly higher than that from readthrough (fig. 2.13C–E), even though several

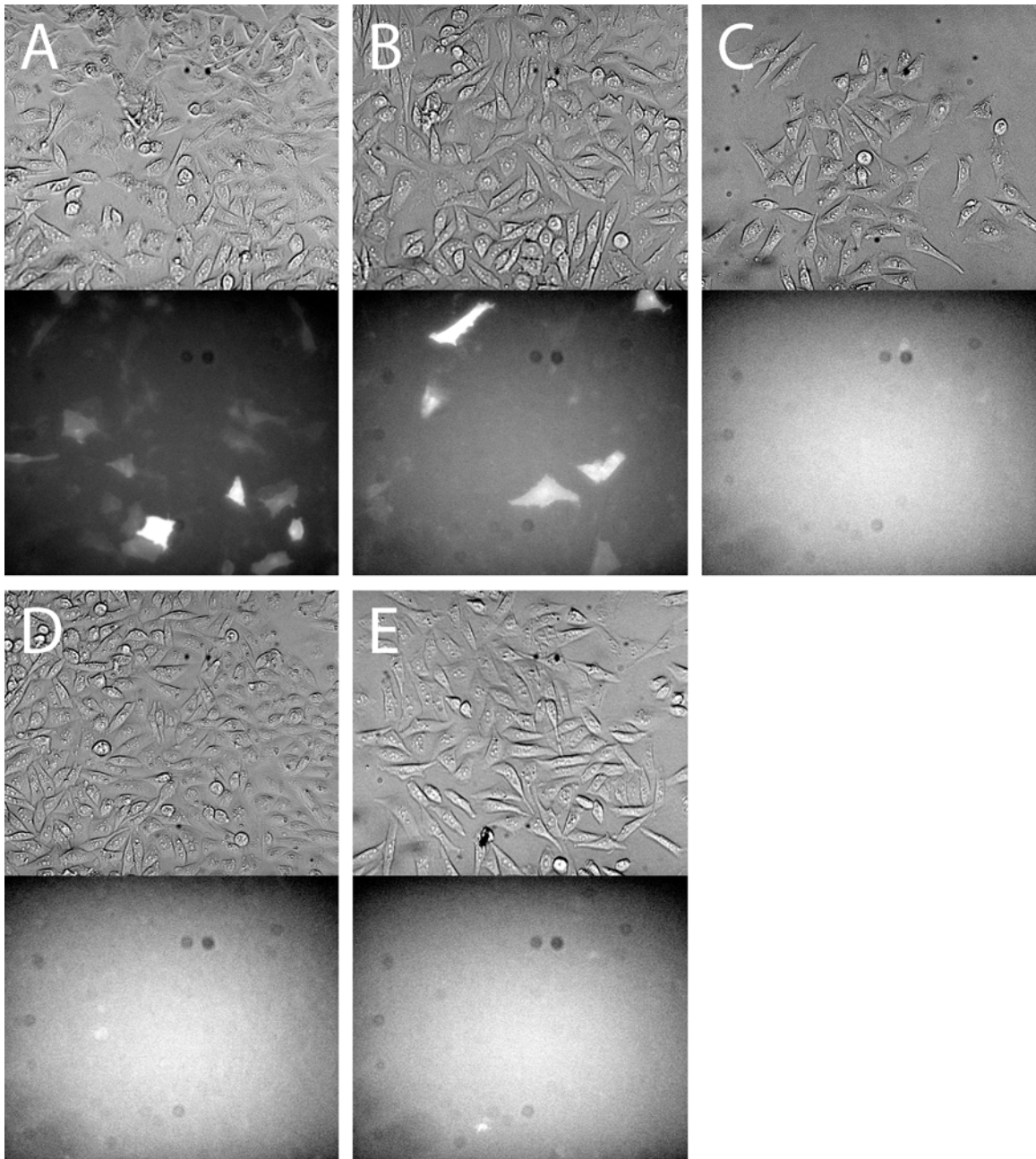


Fig. 2.12. *A–B*, Expression of EGFP in CHO-K1 cells transfected with S29TAG-EGFP DNA and incubated with solutions of 51 μM MPG/0.5 μM HSAS (5/1 charge ratio).

C–E, Control cultures that were incubated with 51 μM MPG only (*C*), 0.5 μM HSAS only (*D*), and F12 medium only (*E*). These results suggested that we had successfully delivered tRNA with MPG, but they could not be reproduced (see fig. 2.13).

Corresponding bright field and fluorescent images are paired. Exposure times for all fluorescent images were 5 s. To improve the quality of the images, they were modified with the Auto Levels and Auto Contrast options in Photoshop.

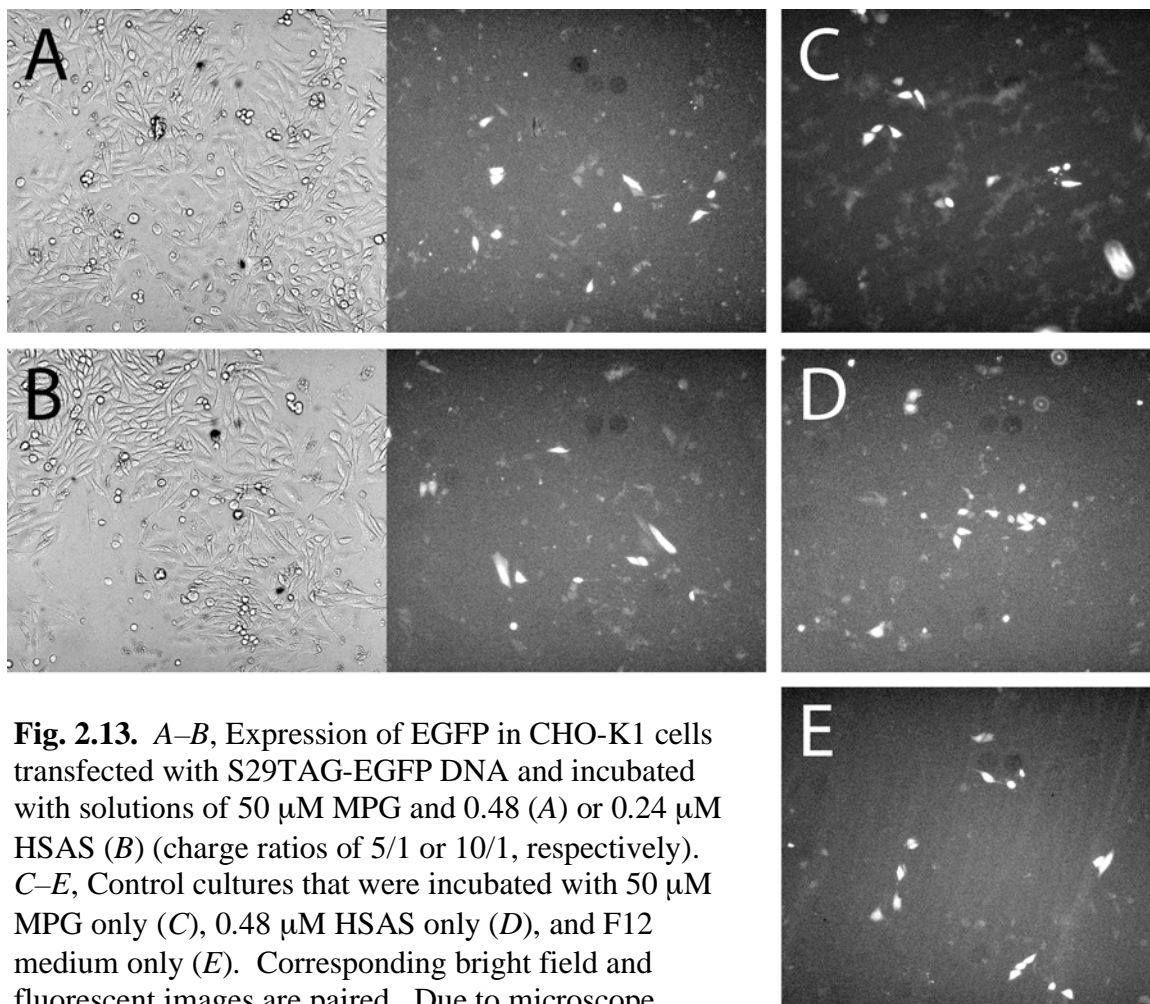


Fig. 2.13. *A–B*, Expression of EGFP in CHO-K1 cells transfected with S29TAG-EGFP DNA and incubated with solutions of 50 μM MPG and 0.48 (A) or 0.24 μM HSAS (B) (charge ratios of 5/1 or 10/1, respectively). *C–E*, Control cultures that were incubated with 50 μM MPG only (C), 0.48 μM HSAS only (D), and F12 medium only (E). Corresponding bright field and fluorescent images are paired. Due to microscope malfunction the bright field images for the fluorescent images in *C–E* were not obtained. Exposure times for all fluorescent images were 2 s. To improve the quality of the images, they were modified with the Auto Levels and Auto Contrast options in Photoshop.

attempts were made to optimize the charge ratio and amount of HSAS in the delivery complexes. Therefore, it could not be definitively stated that the MPG delivered HSAS to the cells. This result was observed in both CHO-K1 and HEK293 cells.

In summary, we were unable to reproduce any of the results of Divita and co-workers [46–48]. We failed to observe MPG and DNA complexation by fluorescence, and we could not use MPG to deliver plasmid DNA or RNA into cells. It is very

puzzling that our results differed so drastically from theirs. A possible explanation is that MPG is a cell-type specific carrier, unable to deliver to CHO or HEK cells. None of the previous reports of Divita and co-workers involved these cell types. Also, it is interesting that so far, no other research group has reported using MPG to deliver nucleic acids into cells, indicating that MPG may be functional as a delivery agent only under very specific conditions. In any case, we concluded that the method of using MPG to form noncovalent complexes with tRNA for delivery into cells is not a viable strategy in our experiments.

Antp Delivery of tRNA

One other noncovalent complexation experiment was performed. Antp was used instead of MPG as the peptide carrier to delivery tRNA into cells. PF was used to transfect CHO-K1 and HEK cells with S29TAG-EGFP DNA, and solutions containing 50 μM Antp and 0.80 μM HSAS (5/1 charge ratio) were applied to the cells. As seen with the MPG experiments above, the cells of the Antp/HSAS sample (fig. 2.14A,C) had no more fluorescence than those of control cells that received no peptide or tRNA (fig. 2.14B,D). Antp, like MPG, failed as a delivery agent, and the fluorescence seen in the samples was due simply to readthrough.

Therefore, we concluded our experiments involving noncovalent complexation with peptides, never having definitively observed tRNA delivery to the mammalian cells. It was decided that this approach is not a viable option to deliver tRNA.

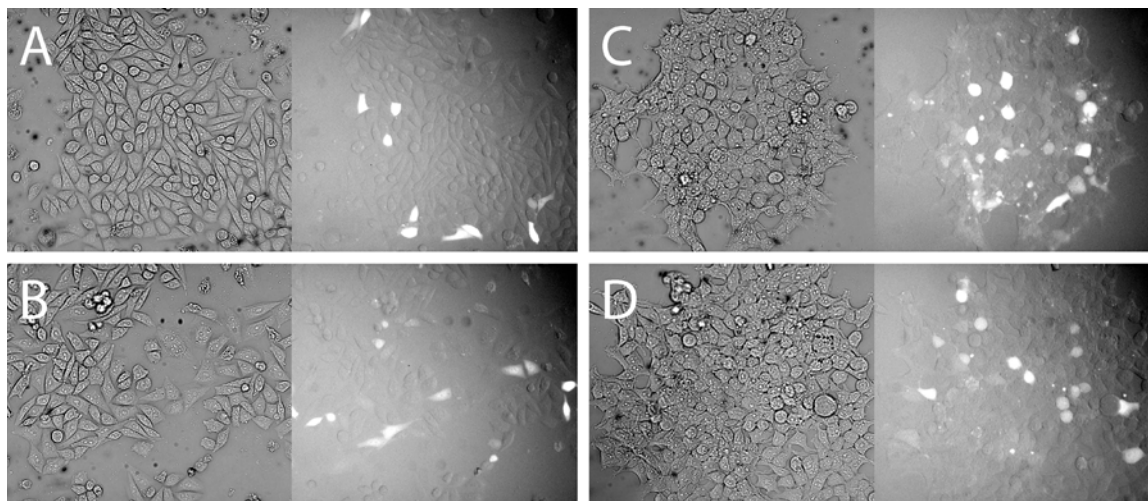


Fig. 2.14. *A–B*, Expression of EGFP in CHO-K1 cells transfected with S29TAG-EGFP DNA and incubated with solutions of 50 μ M Antp and 0.80 μ M HSAS (5/1 charge ratio) (*A*) or F12 only (*B*). *C–D*, Expression of EGFP in HEK293 cells transfected with S29TAG-EGFP DNA and incubated with solutions of 50 μ M Antp and 0.80 μ M HSAS (5/1 charge ratio) (*C*) or F12 only (*D*). Corresponding bright field and fluorescent images are paired. Exposure times for all fluorescent images were 2 s. To improve the quality of the images, they were modified with the Auto Levels and Auto Contrast options in Photoshop.

Preparation of Tat-eEF1A Fusion Protein

The final approach to utilize PTDs to deliver tRNA to cells is the production of a chimera of a PTD and a tRNA-binding protein, specifically the Tat PTD and the eukaryotic elongation factor eEF1A (formerly known as EF-1 α). Fusing proteins and PTDs has been shown to impart them with the PTD translocation properties [24–26], even allowing them to also transport sufficiently tight binding partners of the protein [51]. In this manner, the Tat-eEF1A fusion protein can be mixed with tRNA outside the cell, and the entire complex can be internalized by translocation of the Tat (fig. 2.15).

Furthermore, the ternary complex of eEF1A, GTP, and aminoacyl-tRNA is recruited by the ribosome for tRNA delivery to the ribosomal A site [52, 53]. The formation of this complex is a necessary step for translation, so prebinding the unnatural aminoacyl-tRNA to GTP-activated eEF1A and delivering the complex into the cells

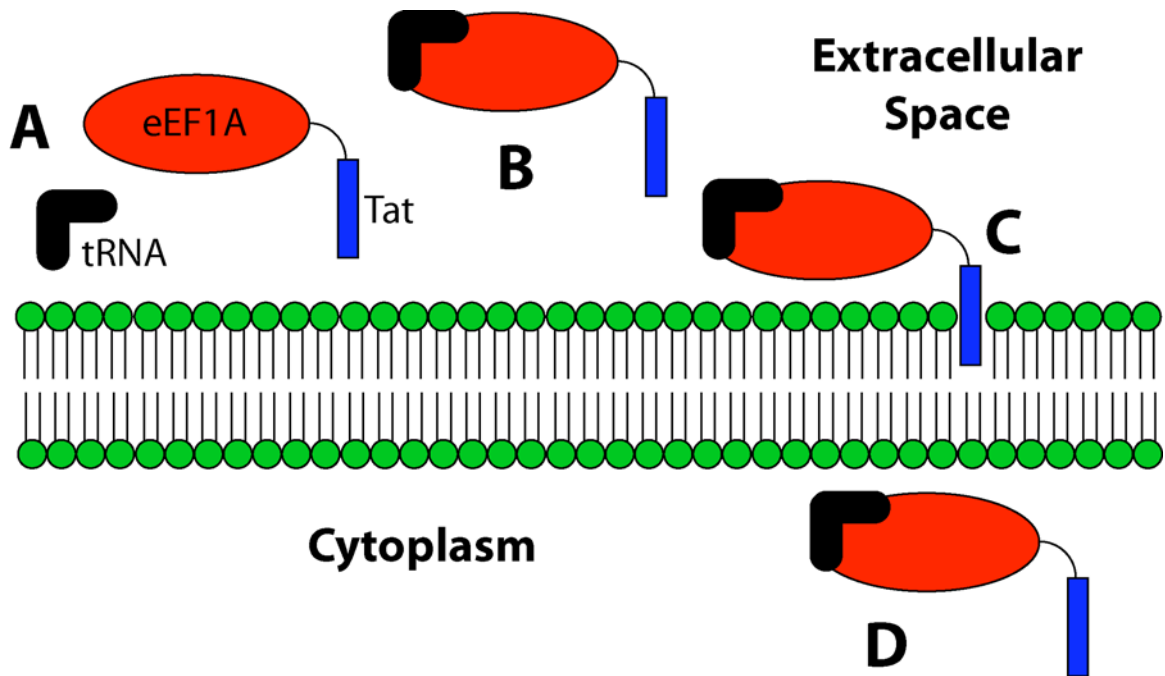


Fig. 2.15. Delivery of tRNA using Tat-eEF1A. The tRNA and Tat-eEF1A are mixed in the external solution (A) and bind together (B). Translocation of the Tat peptide (C) internalizes the entire complex (D).

could make nonsense suppression more efficient. The tRNA molecules would be delivered directly to the ribosome, eliminating the need to encounter an endogenous eEF1A inside the cell.

The binding affinities for the eEF1A and natural aminoacyl-tRNAs range from ~ 1 to 10 nM, which probably is sufficiently high to maintain a stable complex during translocation into the cell [54]. However, studies on the prokaryotic homologue EF1A (formerly known as EF-Tu), which has RNA binding properties similar to eEF1A [54], have demonstrated that the aminoacyl moiety of the charged tRNA strongly influences its binding affinity. The affinities of misacylated tRNA molecules cover a much broader range, from less than 100 pM to more than 300 nM [55, 56]. It is difficult to predict how a specific unnatural aminoacyl-tRNA will bind to eEF1A, but hopefully the complex can

survive intact throughout the delivery into the cell, even if the binding affinity is significantly weaker than the normal interactions between eEF1A and aminoacyl-tRNA.

There are several steps involved in producing recombinant Tat-eEF1A. First, the genetic construct must be generated and transformed into bacteria. Second, the protein must be overexpressed and purified from the numerous bacterial proteins. Finally, if the protein is not already in its native conformation, appropriate refolding conditions must be determined.

Generation of the Fusion Protein Construct, Transformation, and Overexpression

To generate the fusion protein construct, the eEF1A gene from *Xenopus laevis* was subcloned into the pTAT plasmid, a vector that was designed to allow for the easy generation of Tat fusion proteins [57]. The fact that this gene is from *Xenopus*, not of mammalian origin, is not a concern even in a mammalian expression system, because eEF1A is one of the most conserved proteins known [53]. For example, the *Xenopus* and human proteins are 96% identical. The plasmid containing the eEF1A insert was transformed into the Rosetta(DE3) bacterial cell line, which is effective for the overexpression of proteins of eukaryotic origin such as eEF1A. The Rosetta(DE3) line is identical to the BL21(DE3) *E. coli* cell line, except its genome is supplemented with six tRNA genes with anticodons common in eukaryotes but rare in prokaryotes.

Tat-eEF1A was overexpressed, and several different harvesting procedures were attempted. The protein formed inclusion bodies that needed to be purified and solubilized, as observed previously for an EF1A/eEF1A chimera [58], so an inclusion

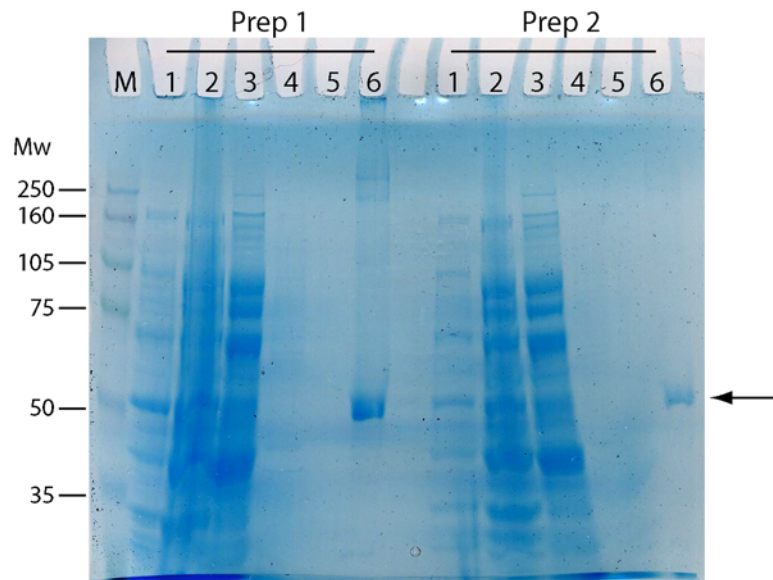


Fig. 2.16. Coomassie-stained polyacrylamide gel showing the protein harvested at different stages of inclusion body purification. Two individual preparations are shown; the same step for each preparation is marked with the same lane number.

Lane M: rainbow markers, with molecular weights at left. Lane 1: uninduced control sample. Lane 2: induced control sample. Lane 3: supernatant 1. Lane 4: supernatant 2.

Lane 5: supernatant 3. Lane 6: inclusion body pellet solubilized in 8 M guanidinium chloride. See methods for the details of the purification. The Tat-eEF1A is marked by the arrow, clearly in a pure, concentrated solution in lane 6.

body preparation procedure was used. This method yielded a large amount of protein, producing 20 to 100 mg per liter of bacterial culture (fig. 2.16).

The presence of Tat-eEF1A in inclusion bodies was fortunate because the relatively simple preparation of the inclusion bodies yielded almost completely pure protein, as inclusion bodies contain only trace amounts of the endogenous bacterial proteins (fig. 2.16). However, it added the complication that the denatured protein needed to be refolded into an active form, and suitable refolding conditions could only be determined by trial and error.

Refolding

The most common method of refolding solubilized, denatured proteins is rapid dilution in buffer containing additives that enhance refolding, such as DTT, arginine (Arg), guanidinium chloride (GuCl), and glycerol. Buffers of eight different compositions were tried: all possible combinations of buffers that contained 0 or 400 mM Arg, 0 or 500 mM GuCl, and 0 or 20% glycerol. 1–2 mg Tat-eEF1A was diluted in 80 mL of each refolding buffer and stirred gently for eight hours. The solution was filtered through a 0.2 μm filter to remove protein that had reaggregated, and was then concentrated.

Upon dilution of the protein, it was immediately obvious that the solutions that contained neither Arg nor GuCl did not promote refolding, because the protein precipitated out and formed a cloudy mixture. However, precipitates were not visible in the other six solutions, so after filtration and concentration, the protein yields were determined by sodium dodecyl sulfate-polyacrylamide gel electrophoresis (SDS-PAGE). The results indicated that three buffers—the Arg/glycerol, Arg/GuCl/glycerol, and Arg/GuCl solutions—all prevented reaggregation of the protein and resulted in good yields of concentrated protein (fig. 2.17). The other three other buffers—the GuCl/glycerol, Arg, and GuCl solutions—did not. Thus, protocols for the purification and solubilization of Tat-eEF1A were determined.

The protein, however, was not stable in solution at high concentrations for very long, even when stored at 4 °C. PAGE performed even one or two days after purification and concentration showed that all the protein had been degraded. It was not clear what mechanism caused the degradation. One possibility is that the inclusion bodies contained

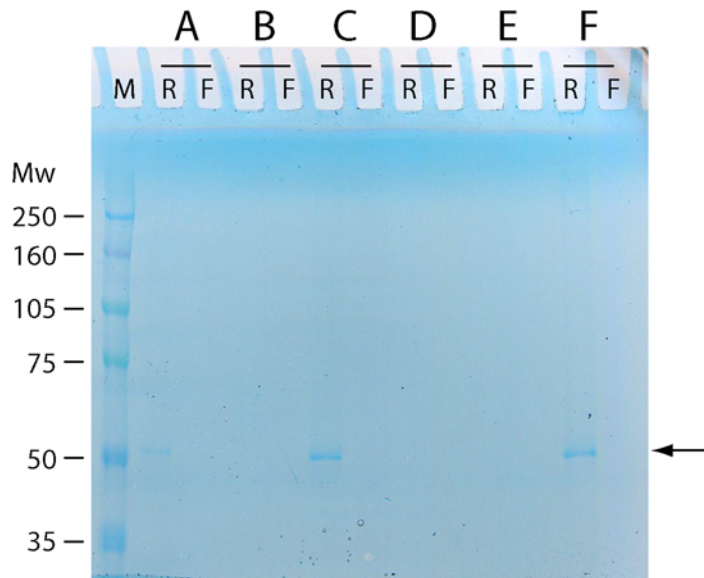


Fig. 2.17. Coomassie-stained polyacrylamide gel of the retentates (R lanes) and filtrates (F lanes) following the concentration of Tat-eEF1A in several refolding buffers. Buffer compositions were 400 mM Arg/20% glycerol (A), 500 mM GuCl/20% glycerol (B), 400 mM Arg/500 mM GuCl/20% glycerol (C), 400 mM Arg (D), 500 mM GuCl (E), and 400 mM Arg/500 mM GuCl (F). Lane M: rainbow markers with molecular weights at left. Tat-eEF1A is marked with the arrow, clearly appearing the retentates of three refolding buffers (A, C, and F).

trace amounts of proteases, which, once refolded, acted to proteolyze the Tat-eEF1A.

Even though it seemed unlikely because the refolding buffers contained protease inhibitors, this hypothesis was tested. Further purification of Tat-eEF1A was performed, taking advantage of its 6His tag, in order to completely isolate it from any proteases. The solubilized inclusion bodies were passed through a column of Ni-NTA beads to isolate the desired protein before refolding. However, the problem of the degradation remained even after the Ni-NTA treatment.

Even though the protein could be purified and concentrated, it still remained to be determined if the Tat-eEF1A had folded into a fully functional form, able to bind tRNA. Efforts were made to develop a gel-shift assay, used previously for RNA-binding proteins [59, 60], which would confirm proper refolding of the protein. The binding of tRNA to

the Tat-eEF1A should change the mass/charge ratio significantly, causing the complex to run at a rate distinct from its individual components in a native PAGE gel.

There were a number of challenges to overcome, most notably getting the protein into a native PAGE gel. Like many proteins that bind nucleic acids, eEF1A has a high pI (~9.3), so it is positively charged at neutral pH. Therefore, the unbound protein should not run into the gel under normal electrophoresis conditions, but should simply drift in the buffer towards the cathode. Forcing a negative charge onto Tat-eEF1A by raising the pH of the buffers was not a good solution because it is almost certain to obliterate binding to tRNA.

One interesting option was setting a native PAGE gel in a horizontal container with the sample wells in the center of the gel instead of at the side nearest the cathode. With this “horizontal PAGE” setup, the protein must enter the gel whether it is positively or negatively charged. Although this was an unorthodox method for PAGE electrophoresis, such a gel was loaded with different amounts of Tat-eEF1A and tRNA and later visualized by silver staining (fig. 2.18A–B), but there were several problems. First, the tRNA bands were very obvious (fig. 2.18A), but a protein band was difficult to find. There may have been a very light band from the protein very near the wells towards the anode (fig. 2.18B), but that was opposite of the expected direction for a positively charged protein. To confuse matters, this possible protein band was not seen in a normally poured native PAGE gel (fig. 2.18C), even though the horizontal PAGE results suggested it should have been, so it remained unidentified. Second, it was difficult to handle and stain the horizontal PAGE gel due to its relatively large size. It is unclear if

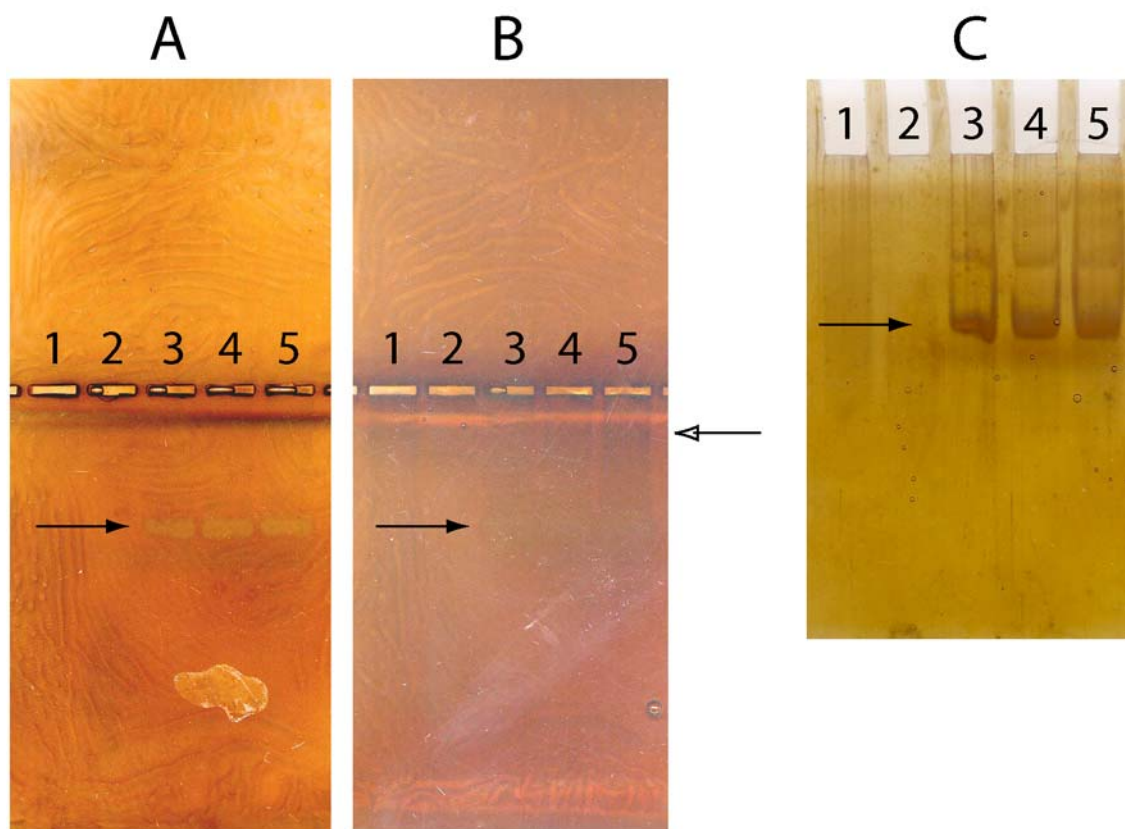


Fig. 2.18. Silver-stained gels from native PAGE of solutions of Tat-eEF1A and HSAS. *A–B*, A gel run horizontally with the wells in the center. *A* and *B* show the same gel at different stages in the development of the silver stain. *C*, A gel run vertically with the wells at the top. All the lanes marked with the same number have identical compositions.

Lane 1: 4 μg Tat-eEF1A. Lane 2: 1 μg Tat-eEF1A. Lane 3: 0.25 μg HSAS.

Lane 4: 1 μg Tat-eEF1A and 0.25 μg HSAS. Lane 5: 4 μg Tat-eEF1A and 0.25 μg HSAS. The black arrow marks the HSAS; the outlined arrow marks a possible protein band, barely discernible in *B* and appearing nowhere else.

the failure to see a protein band was due to degradation, poor staining, or some other factor resulting from the unusual gel technique.

Other methods for detecting the binding of tRNA to Tat-eEF1A were considered but not attempted. Isoelectric focusing, a gel technique that separates proteins based on their pI values, would almost certainly be able to distinguish bound and unbound Tat-eEF1A, but it requires a special apparatus that was not available to us. Also, cross-linking techniques were considered. UV irradiation of a mixture of Tat-eEF1A and

tRNA could result in covalent cross-linking, which would allow for analysis by standard SDS-PAGE. However, cross-linking would probably not be very efficient or quantitative. Even if the protein was properly refolded and bound tRNA, it may not be detectable by this method.

Because of the puzzling problems with degradation of the protein and the lack of a method to determine if the protein was properly refolded, the use of Tat-eEF1A was not a viable strategy for tRNA delivery to mammalian cells.

CONCLUSION

PTDs were expected to be effective vectors for delivering aminoacyl-tRNA to mammalian cells for nonsense suppression. We attempted to develop a PTD-tRNA delivery system by three different approaches: covalent ligation of the two molecules, noncovalent binding, and binding tRNA to a protein linked to a PTD. However, none of these approaches ever successfully transported tRNA into mammalian cells.

To be useful, any PTD technique for tRNA delivery must outperform the relatively easy and effective technique of electroporation. It is possible that such a technique may one day be found. However, this seems much less likely than it did several years ago. The initial reports of the abilities of PTDs to universally cross cell membranes and their seemingly unlimited towing capacity generated much excitement. However, more recent research has shown that the initial results were artifactual and revealed that PTDs were, in fact, relatively limited in their translocation capabilities.

This work was performed concurrently with the optimization of tRNA delivery to mammalian cells by electroporation, which proved to be an effective technique [13].

Because of the success of electroporation, the failure of all three PTD-based approaches, and the diminished likelihood that PTDs could ever be as effective as electroporation, this project was discontinued.

MATERIALS AND METHODS

tRNA Generation

The human serine amber suppressor (HSAS) gene was subcloned into pUC19 as described in [13]. The construct had a T7 transcriptional promoter and a FokI restriction site after 74 bases of the HSAS. The plasmid was amplified and linearized by FokI, and the MegaShortScript Kit from Ambion (Austin, TX) was used for *in vitro* transcription of the 74mer HSAS (the tRNA lacking its two 3' bases).

Thiophosphate Reaction with Maleimide

Alkaline phosphatase (AP) was purchased from Boehringer-Mannheim (Indianapolis, IN), T4 polynucleotide kinase (PNK) from New England Biolabs (Ipswich, MA), and RNase inhibitor from Roche (Indianapolis, IN). ATP-(3-thiophosphate) (ATP- γ -S) was purchased from Boehringer-Mannheim (Indianapolis, IN). N-(1-pyrenyl)maleimide (PM) and 2-mercaptoethanol (2-ME) were purchased from Aldrich. Slide-A-Lyzers were purchased from Pierce (Rockford, IL).

tRNA with a thiophosphate on its 5' end (tRNA-5'-S) was prepared in the following manner. HSAS was prepared by *in vitro* transcription. It was converted to a 5'-OH by AP treatment, with a typical reaction consisting of 100 μ g HSAS, 40 U AP, 80 U RNase inhibitor, and 20 μ L 10x buffer in a total volume of 200 μ L. After

incubating at 50 °C for 2 hours, the protein was removed by PCI treatment, and the tRNA-5'-OH was isolated by ethanol precipitation. This was converted to tRNA-5'-S by PNK treatment, with a typical reaction consisting of 80 µg tRNA-5'-OH, 80 U PNK, 80 U RNase inhibitor, 100 µM spermidine, 500 µM ATP-γ-S, and 20 µL 10x buffer in a total volume of 200 µL. After incubation at 37 °C for 2 hours, the protein was removed by PCI treatment, the free ATP-γ-S was removed by dialysis in Slide-A-Lyzers against 2 L Millipore water (exchanged at 2 hours and 4 hours) for 8 hours, and the tRNA-5'-S was isolated by ethanol precipitation.

A stock solution of 800 µM PM was prepared in 8% DMSO. The DMSO was required to enhance PM's aqueous solubility. Solutions containing various concentrations of 2-ME, ATP-γ-S, and tRNA-5'-S with PM were prepared, in duplicate, in 100 mM phosphate buffer at pH 9.5. Fluorescence emission spectra with an excitation wavelength of 338 nm and a high PMT setting were taken after incubation at room temperature for ~24 hours. The spectra were collected with a SpectraMax Gemini XS fluorescence plate reader using SOFTmax PRO 3.1.2 software.

Noncovalent Complexation Experiments

Materials

Peptides were synthesized on an ABI 433A Peptide Synthesizer and stored as a lyophilized powder. MPG contains a cysteamide at its C-terminus, so it was prepared using a cysteamine 4-methoxytrityl resin, purchased from Calbiochem-Novabiochem (La Jolla, CA). The pTAT plasmid was obtained from Steven Dowdy (Washington University), and the pCS2 plasmid containing the wt-EGFP gene (wt-EGFP DNA) from

Jack Horne (Caltech). The S29TAG-EGFP DNA was obtained by mutation of the wt-EGFP DNA as described previously [13]. Ham's F12 medium and DMEM were purchased from Irvine Scientific (Santa Ana, CA), and CO₂ independent medium was purchased from GIBCO Invitrogen Corporation (Carlsbad, CA). Epizap slides and the Epizap electroporation apparatus were purchased from ASK Science Products (Kingston, Ontario). CultureWell slides were obtained from Grace Bio Labs (Bend, OR). MatTek glass-bottom dishes were obtained from MatTek Corporation (Ashland, MA). PolyFect Transfection Reagent (PF) and the MaxiPrep kits used to isolate plasmids were purchased from Qiagen (Valencia, CA).

Monitoring Complexation with DNA by Fluorescence

Phosphate buffer was prepared with 150 mM NaCl, 18 mM KH₂PO₄, and 5 mM Na₂HPO₄, pH 7.4, the same composition as in [47]. Solutions with 10 μM MPG and 0 to 19.2 μM plasmid DNA (pTAT or wt-EGFP DNA) with or without 30 μM DTT were prepared in phosphate buffer. The fluorescence of the tryptophan residue in MPG was measured at excitation and emission wavelengths of 290 and 345 nm, respectively, at medium PMT, with a SpectraMax Gemini XS fluorescence plate reader using SOFTmax PRO 3.1.2 software.

Cell Culture

CHO-K1 cells were grown in Ham's F12 medium supplemented with fetal bovine serum (10%), glutamine, penicillin, and streptomycin. HEK293 cells were grown in

DMEM with the same additives. The medium with the additives is referred to as “growth medium.” Cells were incubated at 37 °C under 5% CO₂.

CHO-K1 cells were seeded in 8-well CultureWell slides, Epizap slides, or 35 mm MatTek glass-bottom culture dishes. Before seeding, the CultureWell slides were either left untreated, rinsed with ethanol and left to air dry, or rinsed once in ethanol and several times in F12 growth medium. The Epizap slides and MatTek dishes were used without treatment.

During seeding, cells were counted with a bright line counting chamber from Hausser Scientific (Horsham, PA). Usually, 2×10^5 CHO-K1 cells or 1×10^5 HEK293 cells were added to dishes. DNA transfection was usually performed ~48 hours after plating.

DNA Transfection by MPG

CHO-K1 cells were plated on Epizap slides held in 35 mm dishes. The DNA to be transfected was precipitated in ethanol and ammonium acetate and left at –20 °C for at least 1 hour. This was subjected to microcentrifugation at 15,000 rpm and 4 °C for 15 minutes, vacuum dried for 5 minutes, and resuspended in 20 µL serum-free F12 medium with 100 µM MPG. The amounts of DNA used were 6.25, 12.5, 25, or 50 nM wt-EGFP DNA, corresponding to charge ratios of 17.8/1, 8.9/1, 4.4/1, and 2.2/1, respectively. The solution was left for ~30 minutes to allow complexation of the MPG and DNA. 20 µL control solutions of 100 µM MPG only, 25 nM DNA only, and F12 only were also prepared. All medium was removed from the dishes that contained the Epizap slides, and the MPG/DNA solutions were applied to the cells for ~60 minutes at

37 °C. 3 mL F12 growth medium was then added to the dishes, and they were returned to the incubator. The cells were imaged by fluorescence microscopy ~24 hours later.

Transfection by Epizap

CHO-K1 cells were plated on Epizap slides. DNA was precipitated and dried as above and resuspended in CO₂-independent medium to give a final concentration of ~1 µg/µL. The medium was removed from the dishes, and 17 µL of the DNA solution was applied to the cells. Electroporation was performed with an Epizap electroporation apparatus by applying a series of 4 pulses of 50 V with a capacitance of 1.0 µF. F12 growth medium was immediately added and the dishes were returned to the incubator. The cells were imaged by fluorescence microscopy 24–48 hours later.

Transfection by PolyFect Reagent

CHO-K1 or HEK293 cells were plated on MatTek dishes. For transfection, the procedure outlined in the PolyFect Transfection Reagent Handbook was followed. 1.5 µg wt-EGFP or S29TAG-EGFP DNA was diluted to a total volume of 100 µL in serum-free F12 (for CHO-K1 cells) or DMEM (for HEK293 cells). 10 µL PF was added to the solution and mixed thoroughly. The solution was incubated for 10 minutes at room temperature. The medium was removed from the cells, and 1.5 mL of fresh growth medium was reapplied. 600 µL of growth medium was then mixed into the DNA/PF solution and added to the dish. The dish was returned to the incubator. Other amounts of DNA and PF were also used in initial experiments to determine the optimal conditions. The cells were imaged by fluorescence microscopy 24–48 hours later.

MPG and Antp Delivery of tRNA

Cells were transfected by Epizap or PF with S29TAG-EGFP DNA. ~24 hours after transfection, solutions of peptide and HSAS were prepared in serum-free F12 (for CHO-K1 cells) or DMEM (for HEK293 cells) and left for ~30 minutes to allow complexation to occur. The volumes of the solutions were 20 μ L for Epizap slides and 50 μ L for MatTek dishes, and typical concentrations were 50 or 100 μ M peptide and 0.25, 0.5, or 0.8 μ M HSAS, giving charge ratios of 10/1, 5/1, or 3/1. The medium was removed from the dish, and the peptide/HSAS solutions were applied to the wells in the dishes for ~60 minutes at 37 °C. 2 mL fresh growth medium was added to the dishes and they were returned to the incubator. The cells were imaged by fluorescence microscopy 24–48 hours later.

Production of Tat-eEF1A Fusion Protein

Materials

The gene for *Xenopus laevis* eEF1A was obtained from the mMessage mMachine kit, which was purchased from Ambion (Austin, TX). Synthetic DNA oligonucleotides were synthesized by an ABI 394 DNA Synthesizer on site. The pTAT plasmid was a generous gift from Steven Dowdy (Washington University). Rosetta(DE3) cells were purchased from Novagen (San Diego, CA). Luria Broth (LB) was purchased from DIFCO. Terrific Broth (TB) was purchased from Invitrogen (Carlsbad, CA). Ready Gels, 5x TBE buffer, and 40% 29:1 acrylamide:bisacrylamide were purchased from Bio-Rad (Hercules, CA). Ni-NTA Superflow beads were purchased from Qiagen (Valencia, CA). EDTA-free protease inhibitor cocktail pellets were purchased from Roche

(Indianapolis, IN). Centricon Plus-80 concentrators were purchased from Millipore (Billerica, MA).

Mutagenesis and Plasmid Generation

Two synthetic oligonucleotide primers were designed to add a KpnI restriction site just to the 5' side of the gene and an EcoRI site just to the 3' side. PCR was used to incorporate these primers into the eEF1A gene. Using the restriction enzymes, the gene was inserted into the pTAT plasmid, which contains a T7 promoter, a sequence encoding the Tat PTD, and a polylinker allowing for easy generation of Tat-fusion proteins. The proper insertion of the gene was confirmed by DNA sequencing. The peptide sequence appended to the N-terminus of eEF1A was

MRGSHHHHHHHGMASMTGGQMGRLDYDDDDKDRWGSKLGYGRKKRRQRRR
GGSTMAGTT, where both the 6His tag and the Tat PTD are underlined. The gene encoded a 521 amino acid protein with a molecular weight of 57 kD.

Transformation and Overexpression

The pTAT plasmid containing the Tat-eEF1A gene was transformed into Rosetta(DE3) competent cells. This cell line is identical to the BL21(DE3) cell line, except it contains an additional chloramphenicol-resistant plasmid that encodes six tRNA genes with anticodons that are rare in *E. coli* but abundant in eukaryotic genes: AGG and AGA (Arg), AUA (Ile), CUA (Leu), CCC (Pro), and GGA (Gly). Therefore, it is recommended for use in overexpressing eukaryotic proteins. Because 30 of the 521 codons in the Tat-eEF1A gene (5.8%) are among these six, the Rosetta cell line provided

a significant advantage over other cell lines. The cells were plated on agar plates of LB+Amp.

A seed culture for overexpression of the protein was started by picking a colony from the plate and growing overnight in 25 mL LB+Amp. The entire seed culture was poured into 500 mL TB+Amp and incubated until the OD₆₀₀ reached 0.6–0.8. A 1 mL aliquot of the culture was removed as the uninduced control. Protein expression was induced by adding IPTG to a final concentration of 0.4 mM, and the culture was grown for 2 more hours. A 1 mL aliquot was again removed as the induced control. The cells were pelleted by centrifugation for 20 minutes at 6000g and 4 °C.

In preparation for analysis by sodium dodecyl sulfate-polyacrylamide gel electrophoresis (SDS-PAGE), the control samples were pelleted by microcentrifugation. The pellets were washed twice in 1.5 mL cold phosphate buffered saline (PBS) and resuspended in 50 µL water. 50 µL of 2x SDS loading buffer was added, and the solutions were boiled for 5 minutes.

Protein Purification from Inclusion Bodies

The protocol for the isolation of proteins from inclusion bodies was obtained from the lab of Pamela Bjorkman (Caltech), available at the link for “Inclusion body preparation” on her website (<http://www.its.caltech.edu/~bjorker/protocols.html>).

Solution buffer consisted of 50 mM Tris-Cl, 25% sucrose, 1 mM NaEDTA, 0.1% NaN₃, and 10 mM DTT, pH 8.0. Lysis buffer consisted of 50 mM Tris-Cl, 1% Triton X-100, 1% sodium deoxycholate, 100 mM NaCl, 0.1% NaN₃, and 10 mM DTT, pH 8.0. Washing buffer without Triton X-100 contained 50 mM Tris-Cl, 100 mM NaCl, 1 mM

NaEDTA, 0.1% NaN₃, and 1 mM DTT, pH 8.0. Washing buffer with Triton X-100 was also prepared by including 0.5% Triton X-100 in the above washing buffer.

The bacterial pellet was suspended in 13 mL solution buffer on ice and transferred to a 30 mL centrifugation bottle. It was probe sonicated for 2 pulses of 30 seconds each at level 75 (~12 W). 5 mg lysozyme, 125 U DNaseI, and 25 µL 500 mM MgCl₂ were added, and the mixture was vortexed. 12 mL of lysis buffer was added, and the mixture was incubated for 45 minutes at room temperature. 372 µL 500 mM NaEDTA in 50 mM Tris-Cl, pH 8.0 was added, and the mixture was rapidly frozen in liquid nitrogen, then thawed at 37 °C for 30 minutes. 100 µL 500 mM MgCl₂ was added, and the mixture was incubated for 45 minutes at room temperature. 372 µL 500 mM NaEDTA in 50 mM Tris-Cl, pH 8.0 was again added. All the remaining steps were done on ice. The mixture was pelleted by centrifugation for 20 minutes at 11,000g and 4 °C, and 1 mL of the supernatant was saved as supernatant 1. The pellet was resuspended in 10 mL wash buffer with Triton X-100 and probe sonicated as above. The mixture was again pelleted as above, and 1 mL of the supernatant was saved as supernatant 2. The pellet was resuspended in 10 mL wash buffer without Triton X-100 and probe sonicated as above. The mixture was pelleted as above, and 1 mL of the supernatant was saved as supernatant 3. The final pellet consisting of the inclusions bodies was dissolved in 9 mL of a solution of 8 M guanidinium chloride (GuCl) and 4 mM DTT by shaking at room temperature. Often, the dissolution of the pellet required more than a day of shaking.

The samples were analyzed for purity by SDS-PAGE. The uninduced and induced expression control samples, supernatants 1, 2, and 3, and the final protein sample were run on a 7.5% Tris-Cl Ready Gel at ~150 V for ~1 hour. The protein was visualized

by staining with Coomassie brilliant blue. Because the mixture of GuCl and SDS precipitates out of solution, which blocks the flow of current, the protein sample was diluted fourfold in water before loading in the gel.

Purification of Tat-eEF1A Using Ni-NTA Beads

~5 µg denatured Tat-eEF1A, dissolved in 8 M GuCl and 4 mM DTT, was incubated with 1–2 mL of Ni-NTA Superflow beads for ~2 hours while shaking at room temperature. The beads have a binding capacity of 5–10 mg protein/mL. The mixture was poured into a small fritted column. The flowthrough was reapplied to the beads in the column several times, and the final flowthrough was collected. The beads were washed with 8 mL of 6 M GuCl, pH 6.3, and the wash solution was also collected. The protein was eluted from the beads by four applications of 1 mL of 6 M GuCl, pH 4.5. Each mL of the eluted solution was saved.

Refolding and Binding Assay

Refolding of the Tat-eEF1A (with or without the Ni-NTA purification) was attempted in eight buffers, which contained all possible combinations of 0 or 400 mM arginine (Arg), 0 or 500 mM GuCl, and 0 or 20% glycerol. Also, each buffer contained 50 mM Tris-Cl, 20 mM NaCl, 10 mM MgCl₂, 10 mM DTT and 1 pellet of EDTA-free protease inhibitor cocktail. The pH was brought to 6.8. 1–2 mg of protein in 8 M GuCl solution was slowly dripped into 80 mL of the various refolding buffers, and gently stirred for ~8 hours. The solutions were then passed through a 0.2 µm filter and concentrated using Centricon Plus-80 concentrators, reducing the volume to 1 mL or less.

Protein content in the filtrates and retentates was analyzed by SDS-PAGE, as described above.

To activate the eEF1A with GTP before tRNA complexation, EF buffer was prepared as in [54]: 40 mM HEPES, 100 mM NH₄Cl, 10 mM MgCl₂, 1 mM DTT, pH 7.5. 4x loading buffer for native PAGE consisted of 1% bromophenol blue and 60% glycerol. 10 μ L solutions were prepared from 2 μ L 5x EF buffer, 3.5 μ L 4x loading buffer, 1 μ L 30 mM GTP, ~4 or ~1 μ g Tat-eEF1A (~70 or ~15 pmol), and 0.25 μ g HSAS (10 pmol). Before HSAS addition, all components (except HSAS) were incubated at 30 °C for 20 minutes to activate eEF1A with GTP. The samples were then run on a native PAGE gel.

Native PAGE gels were prepared in the following manner. A solution of 1x TBE pH 8.3, 12.5% glycerol, and 10% acrylamide (29:1 acrylamide:bisacrylamide), and a separate solution of 10% ammonium persulfate were prepared. Both solutions and TEMED were kept on ice. When sufficiently cold, 112 μ L ammonium persulfate solution and 5 μ L TEMED were added to 7.5 mL of TBE solution. The mixture was shaken and immediately poured into the gel caster. It was allowed to polymerize for several hours. The gel composition was similar to that used previously for a gel-shift assay for tRNA/synthetase binding [60], although the amounts of Tris, boric acid, and EDTA were not identical because we used a Bio-Rad premixed buffer, and the glycerol amount was increased slightly. For horizontal gels in the casters that are normally used for agarose gels, the solution amounts were scaled up 2.5-fold. The protein and tRNA were visualized by silver staining.

REFERENCES

1. Berg, J. M., J. L. Tymoczko, and L. Stryer. 2002. *Biochemistry, Fifth Edition*. New York: W. H. Freeman and Company.
2. Fersht, A. 1999. *Structure and Mechanism in Protein Science*. New York: W. H. Freeman and Company.
3. England, P. M. 2004. Unnatural amino acid mutagenesis: A precise tool for probing protein structure and function. *Biochemistry*. 43:11623-11629.
4. Cashin, A. L., E. J. Petersson, H. A. Lester, and D. A. Dougherty. 2005. Using physical chemistry to differentiate nicotinic from cholinergic agonists at the nicotinic acetylcholine receptor. *J. Am. Chem. Soc.* 127:350-356.
5. England, P. M., H. A. Lester, N. Davidson, and D. A. Dougherty. 1997. Site-specific, photochemical proteolysis applied to ion channels *in vivo*. *Proc. Natl. Acad. Sci. USA*. 94:11025-11030.
6. Gallivan, J. P., H. A. Lester, and D. A. Dougherty. 1997. Site-specific incorporation of biotinylated amino acids to identify surface-exposed residues in integral membrane proteins. *Chem. Biol.* 4:739-749.
7. Petersson, E. J., G. S. Brandt, N. M. Zacharias, D. A. Dougherty, and H. A. Lester. 2003. Caging proteins through unnatural amino acid mutagenesis. *Methods Enzymol.* 360:258-273.
8. Zhong, W., J. P. Gallivan, Y. Zhang, L. Li, H. A. Lester, and D. A. Dougherty. 1998. From *ab initio* quantum mechanics to molecular neurobiology: A cation- π binding site in the nicotinic receptor. *Proc. Natl. Acad. Sci. USA*. 95:12088-12093.
9. Ellman, J., D. Mendel, S. Anthony-Cahill, C. J. Noren, and P. G. Schultz. 1991. Biosynthetic method for introducing unnatural amino acids site-specifically into proteins. *Methods Enzymol.* 202:301-336.
10. Noren, C. J., S. J. Anthony-Cahill, M. C. Griffith, and P. G. Schultz. 1989. A general method for site-specific incorporation of unnatural amino acids into proteins. *Science*. 244:182-188.
11. Nowak, M. W., J. P. Gallivan, S. K. Silverman, C. G. Labarca, D. A. Dougherty, and H. A. Lester. 1998. *In vivo* incorporation of unnatural amino acids into ion channels in *Xenopus* oocyte expression system. *Methods Enzymol.* 293:504-529.
12. Nowak, M. W., P. C. Kearney, J. R. Sampson, M. E. Saks, C. G. Labarca, S. K. Silverman, W. Zhong, J. Thorson, J. N. Abelson, N. Davidson, P. G. Schultz, D. A. Dougherty, and H. A. Lester. 1995. Nicotinic receptor binding site probed with unnatural amino acid incorporation in intact cells. *Science*. 268:439-442.

13. Monahan, S. L., H. A. Lester, and D. A. Dougherty. 2003. Site-specific incorporation of unnatural amino acids into receptors expressed in mammalian cells. *Chem. Biol.* 10:573-580.
14. Bogoyevitch, M. A., T. S. Kendrick, D. C. Ng, and R. K. Barr. 2002. Taking the cell by stealth or storm? Protein transduction domains (PTDs) as versatile vectors for delivery. *DNA Cell Biol.* 21:879-894.
15. Deshayes, S., M. C. Morris, G. Divita, and F. Heitz. 2005. Cell-penetrating peptides: Tools for intracellular delivery of therapeutics. *Cell. Mol. Life Sci.* 62:1839-1849.
16. Fischer, P. M., E. Krausz, and D. P. Lane. 2001. Cellular delivery of impermeable effector molecules in the form of conjugates with peptides capable of mediating membrane translocation. *Bioconjug. Chem.* 12:825-841.
17. Fischer, R., M. Fotin-Mleczek, H. Hufnagel, and R. Brock. 2005. Break on through to the other side—biophysics and cell biology shed light on cell-penetrating peptides. *ChemBiochem.* 6:2126-2142.
18. Derossi, D., A. H. Joliot, G. Chassaing, and A. Prochiantz. 1994. The third helix of the Antennapedia homeodomain translocates through biological membranes. *J. Biol. Chem.* 269:10444-10450.
19. Vives, E., P. Brodin, and B. Lebleu. 1997. A truncated HIV-1 Tat protein basic domain rapidly translocates through the plasma membrane and accumulates in the cell nucleus. *J. Biol. Chem.* 272:16010-16017.
20. Bonny, C., A. Oberson, S. Negri, C. Sauser, and D. F. Schorderet. 2001. Cell-permeable peptide inhibitors of JNK: Novel blockers of beta-cell death. *Diabetes.* 50:77-82.
21. Fujimoto, K., R. Hosotani, Y. Miyamoto, R. Doi, T. Koshiba, A. Otaka, N. Fujii, R. D. Beauchamp, and M. Imamura. 2000. Inhibition of pRb phosphorylation and cell cycle progression by an antennapedia-p16(INK4A) fusion peptide in pancreatic cancer cells. *Cancer Lett.* 159:151-158.
22. Rousselle, C., P. Clair, J. M. Lefauconnier, M. Kaczorek, J. M. Scherrmann, and J. Temsamani. 2000. New advances in the transport of doxorubicin through the blood-brain barrier by a peptide vector-mediated strategy. *Mol. Pharmacol.* 57:679-686.
23. Waizenegger, T., R. Fischer, and R. Brock. 2002. Intracellular concentration measurements in adherent cells: a comparison of import efficiencies of cell-permeable peptides. *Biol. Chem.* 383:291-299.
24. Sahai, E., M. F. Olson, and C. J. Marshall. 2001. Cross-talk between Ras and Rho signalling pathways in transformation favours proliferation and increased motility. *EMBO J.* 20:755-766.

25. Schwarze, S. R., A. Ho, A. Vocero-Akbani, and S. F. Dowdy. 1999. *In vivo* protein transduction: Delivery of a biologically active protein into the mouse. *Science*. 285:1569-1572.
26. Soga, N., N. Namba, S. McAllister, L. Cornelius, S. L. Teitelbaum, S. F. Dowdy, J. Kawamura, and K. A. Hruska. 2001. Rho family GTPases regulate VEGF-stimulated endothelial cell motility. *Exp. Cell Res.* 269:73-87.
27. Allinquant, B., P. Hantraye, P. Mailleux, K. Moya, C. Bouillot, and A. Prochiantz. 1995. Downregulation of amyloid precursor protein inhibits neurite outgrowth in vitro. *J. Cell. Biol.* 128:919-927.
28. Troy, C. M., D. Derossi, A. Prochiantz, L. A. Greene, and M. L. Shelanski. 1996. Downregulation of Cu/Zn superoxide dismutase leads to cell death via the nitric oxide-peroxynitrite pathway. *J. Neurosci.* 16:253-261.
29. Villa, R., M. Folini, S. Lualdi, S. Veronese, M. G. Daidone, and N. Zaffaroni. 2000. Inhibition of telomerase activity by a cell-penetrating peptide nucleic acid construct in human melanoma cells. *FEBS Lett.* 473:241-248.
30. Lewin, M., N. Carlesso, C. H. Tung, X. W. Tang, D. Cory, D. T. Scadden, and R. Weissleder. 2000. Tat peptide-derivatized magnetic nanoparticles allow *in vivo* tracking and recovery of progenitor cells. *Nat. Biotechnol.* 18:410-414.
31. Torchilin, V. P., R. Rammohan, V. Weissig, and T. S. Levchenko. 2001. TAT peptide on the surface of liposomes affords their efficient intracellular delivery even at low temperature and in the presence of metabolic inhibitors. *Proc. Natl. Acad. Sci. USA.* 98:8786-8791.
32. Kramer, S. D., and H. Wunderli-Allenspach. 2003. No entry for TAT(44-57) into liposomes and intact MDCK cells: Novel approach to study membrane permeation of cell-penetrating peptides. *Biochim. Biophys. Acta.* 1609:161-169.
33. Leifert, J. A., S. Harkins, and J. L. Whitton. 2002. Full-length proteins attached to the HIV tat protein transduction domain are neither transduced between cells, nor exhibit enhanced immunogenicity. *Gene Ther.* 9:1422-1428.
34. Leifert, J. A., and J. L. Whitton. 2003. "Translocatory proteins" and "protein transduction domains": A critical analysis of their biological effects and the underlying mechanisms. *Mol. Ther.* 8:13-20.
35. Richard, J. P., K. Melikov, E. Vives, C. Ramos, B. Verbeure, M. J. Gait, L. V. Chernomordik, and B. Lebleu. 2003. Cell-penetrating peptides. A reevaluation of the mechanism of cellular uptake. *J. Biol. Chem.* 278:585-590.
36. Thoren, P. E., D. Persson, P. Isakson, M. Goksor, A. Onfelt, and B. Norden. 2003. Uptake of analogs of penetratin, Tat(48-60) and oligoarginine in live cells. *Biochem. Biophys. Res. Commun.* 307:100-107.

37. Terrone, D., S. L. Sang, L. Roudaia, and J. R. Silvius. 2003. Penetratin and related cell-penetrating cationic peptides can translocate across lipid bilayers in the presence of a transbilayer potential. *Biochemistry*. 42:13787-13799.
38. Thoren, P. E., D. Persson, M. Karlsson, and B. Norden. 2000. The antennapedia peptide penetratin translocates across lipid bilayers—the first direct observation. *FEBS Lett.* 482:265-268.
39. Tung, C. H., and S. Stein. 2000. Preparation and applications of peptide-oligonucleotide conjugates. *Bioconjug. Chem.* 11:605-618.
40. Derossi, D., G. Chassaing, and A. Prochiantz. 1998. Trojan peptides: The penetratin system for intracellular delivery. *Trends Cell Biol.* 8:84-87.
41. Igloi, G. L. 1988. Interaction of tRNAs and of phosphorothioate-substituted nucleic acids with an organomercurial. Probing the chemical environment of thiolated residues by affinity electrophoresis. *Biochemistry*. 27:3842-3849.
42. Monahan, S. L. 2004. Site-specific incorporation of unnatural amino acids into receptors expressed in mammalian cells. Ph.D. thesis, California Institute of Technology.
43. Karim, A. S., C. S. Johansson, and J. K. Weltman. 1995. Maleimide-mediated protein conjugates of a nucleoside triphosphate gamma-S and an internucleotide phosphorothioate diester. *Nucleic Acids Res.* 23:2037-2040.
44. Karim, A. S., and J. K. Weltman. 1993. Formation of protein conjugates of phosphorothioate nucleoside diphosphate beta-S. *Nucleic Acids Res.* 21:5281-5282.
45. Madhusoodanan, K. S., and R. F. Colman. 2001. Adenosine 5'-0-[S-(4-succinimidyl-benzophenone)thiophosphate]: a new photoaffinity label of the allosteric ADP site of bovine liver glutamate dehydrogenase. *Biochemistry*. 40:1577-1586.
46. Vidal, P., M. C. Morris, L. Chaloin, F. Heitz, and G. Divita. 1997. New strategy for RNA vectorization in mammalian cells. Use of a peptide vector. *C. R. Acad. Sci. III.* 320:279-287.
47. Morris, M. C., L. Chaloin, J. Mery, F. Heitz, and G. Divita. 1999. A novel potent strategy for gene delivery using a single peptide vector as a carrier. *Nucleic Acids Res.* 27:3510-3517.
48. Morris, M. C., P. Vidal, L. Chaloin, F. Heitz, and G. Divita. 1997. A new peptide vector for efficient delivery of oligonucleotides into mammalian cells. *Nucleic Acids Res.* 25:2730-2736.

49. Marthinet, E., G. Divita, J. Bernaud, D. Rigal, and L. G. Baggetto. 2000. Modulation of the typical multidrug resistance phenotype by targeting the MED-1 region of human MDR1 promoter. *Gene Ther.* 7:1224-1233.
50. Capone, J. P., P. A. Sharp, and U. L. RajBhandary. 1985. Amber, ochre and opal suppressor tRNA genes derived from a human serine tRNA gene. *EMBO J.* 4:213-221.
51. Pooga, M., C. Kut, M. Kihlmark, M. Hallbrink, S. Fernaeus, R. Raid, T. Land, E. Hallberg, T. Bartfai, and U. Langel. 2001. Cellular translocation of proteins by transportan. *FASEB J.* 15:1451-1453.
52. Andersen, G. R., P. Nissen, and J. Nyborg. 2003. Elongation factors in protein biosynthesis. *Trends Biochem. Sci.* 28:434-441.
53. Negrutskii, B. S., and A. V. El'skaya. 1998. Eukaryotic translation elongation factor 1 alpha: structure, expression, functions, and possible role in aminoacyl-tRNA channeling. *Prog. Nucleic Acid Res. Mol. Biol.* 60:47-78.
54. Dreher, T. W., O. C. Uhlenbeck, and K. S. Browning. 1999. Quantitative assessment of EF-1alpha. GTP binding to aminoacyl-tRNAs, aminoacyl-viral RNA, and tRNA shows close correspondence to the RNA binding properties of EF-Tu. *J. Biol. Chem.* 274:666-672.
55. Asahara, H., and O. C. Uhlenbeck. 2002. The tRNA specificity of *Thermus thermophilus* EF-Tu. *Proc. Natl. Acad. Sci. USA.* 99:3499-3504.
56. LaRiviere, F. J., A. D. Wolfson, and O. C. Uhlenbeck. 2001. Uniform binding of aminoacyl-tRNAs to elongation factor Tu by thermodynamic compensation. *Science.* 294:165-168.
57. Becker-Hapak, M., S. S. McAllister, and S. F. Dowdy. 2001. TAT-mediated protein transduction into mammalian cells. *Methods.* 24:247-256.
58. Arcari, P., M. Masullo, A. Arcucci, G. Ianniciello, B. de Paola, and V. Bocchini. 1999. A chimeric elongation factor containing the putative guanine nucleotide binding domain of archaeal EF-1 alpha and the M and C domains of eubacterial EF-Tu. *Biochemistry.* 38:12288-12295.
59. Cilly, C. D., and J. R. Williamson. 1997. Analysis of bacteriophage N protein and peptide binding to boxB RNA using polyacrylamide gel coelectrophoresis (PACE). *RNA.* 3:57-67.
60. Rubelj, I., I. Weygand-Durasevic, and Z. Kucan. 1990. Evidence for two types of complexes formed by yeast tyrosyl-tRNA synthetase with cognate and non-cognate tRNA. Effect of ribonucleoside triphosphates. *Eur. J. Biochem.* 193:783-788.

Chapter 3

Efforts Toward a High Throughput Assay for Gating of the Mechanosensitive Channel of Large Conductance

Abstract

The bacterial mechanosensitive channel of large conductance (MscL) is an ideal starting point for understanding the molecular basis of mechanosensation. However, current methods for the characterization of its mutants, patch clamp and bacterial growth analysis, are difficult and time consuming, so a higher throughput method for screening mutants is desired. We have attempted to develop a fluorescence assay for detecting MscL activity in synthetic vesicles. The assay involved the separation of two solutions—one inside and one outside the vesicles—that are separately nonfluorescent but fluorescent when mixed. It was hoped that MscL activity due to downshock of the vesicles would bring about mixing of the solutions, producing fluorescence. The development of the assay required the optimization of several variables: the method for producing a uniform vesicle population containing MscL, the fluorescence system, and the lipid and protein composition of the vesicles. However, no MscL activity was ever detected even after optimization, so the assay was not fully developed. The probable cause of the failure was the inability of current techniques to produce a sufficiently uniform vesicle population.

INTRODUCTION

The Mechanosensitive Channel of Large Conductance

The ability to detect and respond to pressure stimuli is essential for an organism to survive. This process, called mechanosensation, is fundamentally involved in many sensory events in all forms of life, such as touch, hearing, and balance in animals, gravitropism and turgor pressure regulation in plants, and osmotic regulation for many cell types, particularly in bacteria and archaea [1–3]. In all of these processes, transmembrane proteins called mechanosensitive ion channels play a key role [4]. These proteins transduce a mechanical signal such as movement or an increased membrane tension into a conformational change, resulting in the formation of an ion-permeable channel through the membrane. Mechanosensitive channels have been discovered in more than thirty cell types in many kinds of organisms.

Mechanosensitive channels play an especially crucial role in osmotic pressure regulation in bacteria. Because bacteria are single-celled organisms unable to traverse large distances, sudden inundation is a threat to their survival. A rapid decrease in the external osmotic pressure, called osmotic downshock, results in a great influx of water through their cellular membranes, causing swelling. Without appropriate defenses, cell death due to lysis would occur with even a mild downshock.

Three bacterial channels—the mechanosensitive channels of large, small, and “mini” conductance (MscL, MscS, and MscM, respectively)—are thought to function as “release valves” to protect the cell during osmotic downshock (fig. 3.1) [5, 6]. When the cellular swelling during downshock increases the tension in the membrane, the channels respond to the accompanying deformation of the lipid bilayer by opening pores in the

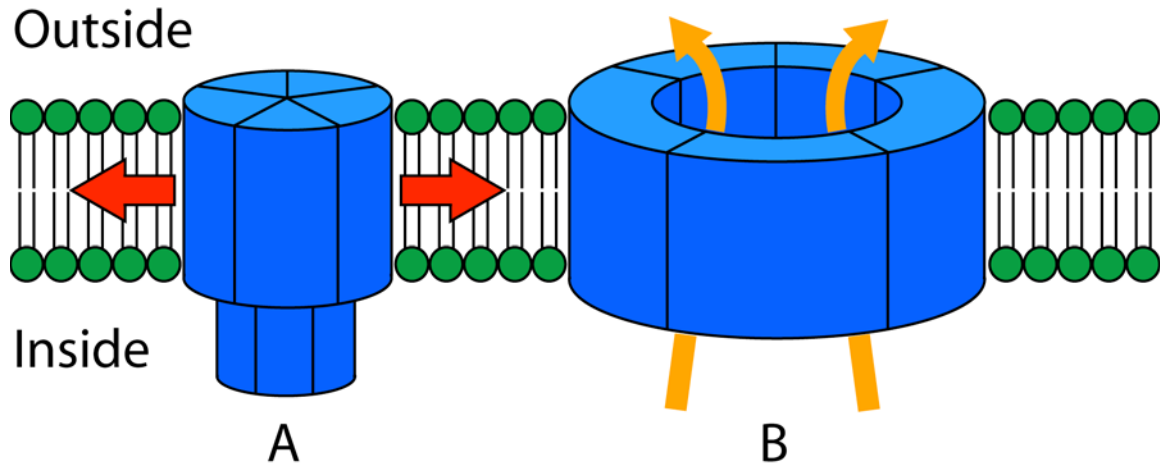


Fig. 3.1. Schematic of the mechanosensation of MscL. Under resting conditions, MscL is in the closed state (A). Osmotic downshock increases the tension in the membrane (red arrows), resulting in a transition to the open state (B). The wide pore of the open state allows the release of intracellular osmolytes (orange arrows), hopefully equilibrating the internal and external osmotic pressures before cell lysis. The outside and inside of the bacterium are noted.

membrane. The cell, instead of swelling to the point of lysis, uses the channels for a somewhat controlled equilibration of the internal and external solutions. The equilibration reduces the osmotic pressure difference, thereby preserving the bacterium.

The three channels differ in their sensitivities to membrane tension. MscM opens at lower tensions than MscS, and MscL requires the largest tension of all for gating (~ 10 dyn/cm) [5, 7]. This pattern suggests that these channels form different lines of defense, with MscL serving as bacteria's last resort for osmoprotection. MscL is activated only if the less severe activities of MscM and MscS fail to rescue the swelling cell [5].

E. coli MscL was the first mechanosensitive channel to be cloned [8].

Homologues have since been found in over 30 species of bacteria [9], and many of these have been cloned as well. Functional characterization of *E. coli* MscL has shown that it opens a large pore. Patch clamping experiments have determined that gating results in a

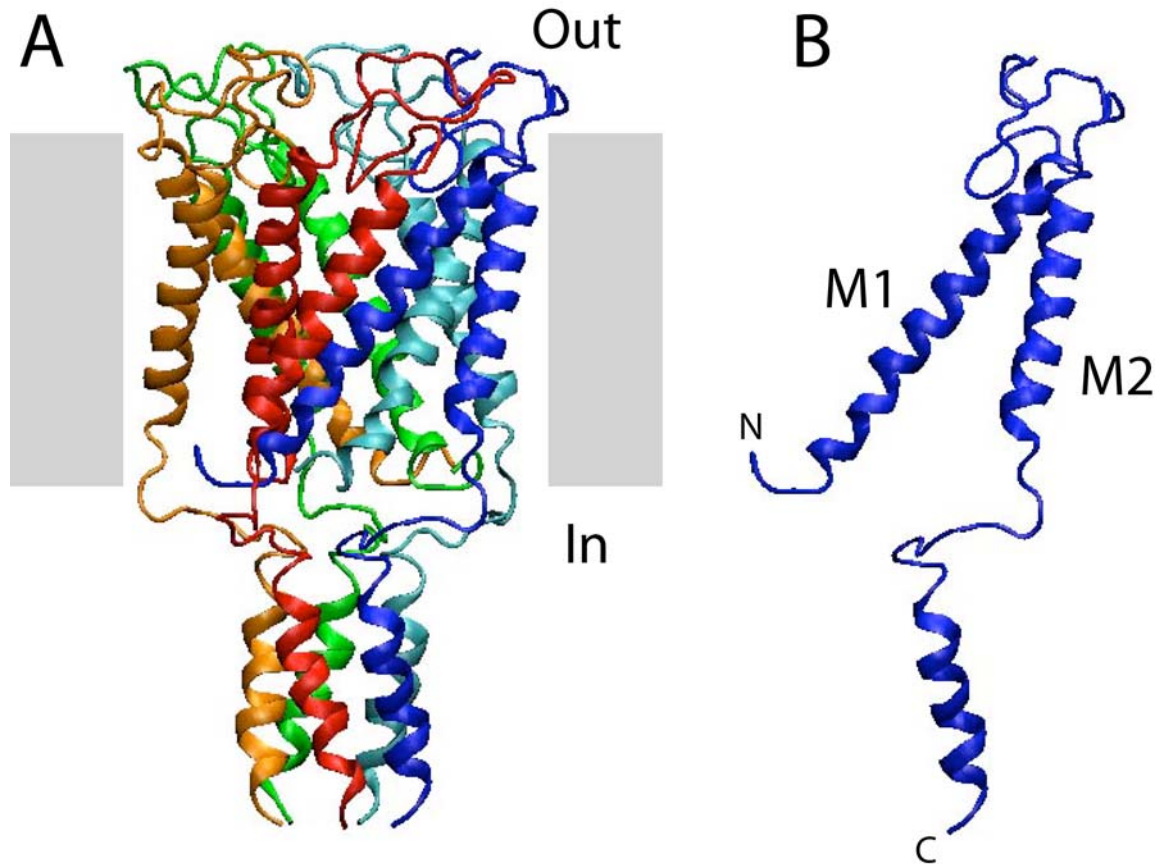


Fig. 3.2. The MscL crystal structure. MscL consists of a homopentamer (A) of identical subunits, one of which is shown (B) with the TM helices M1 and M2 and the N- and C-termini marked. The gray rectangles in A note the probable location of the membrane. The inside and outside of the cell are also indicated. The protein images were prepared with VMD.

highly conductive (~ 3.0 nS), nonspecific channel [10]. In addition, biochemical studies have shown that both ions and small molecules such as ATP can pass through MscL [10]. It is possible that MscL even allows the release of the small proteins EF-Tu, DnaK, and thioredoxin [11, 12], although this claim has been disputed [13]. The permeability data indicate that the pore is 36–42 Å in diameter, extremely large among ion channels [14].

The crystal structure of the closed state of the *M. tuberculosis* homologue of MscL shows that the functional unit is a homopentamer (fig. 3.2A) [15]. Each subunit has two transmembrane (TM) domains M1 and M2 (fig. 3.2B), which are well conserved

across species. Both the N- and C-termini are cytoplasmic [16]. The gate of the channel is formed by the N-terminal part of M1, and the M2 helices form a shell on the periphery of the protein adjacent to the lipid. Each subunit of *E. coli* MscL contains 136 residues [8], the last ~50 of which extend into the cytoplasm and form a pentameric helical bundle [15]. Deletion experiments have shown that the cytoplasmic portion is not necessary for forming a functional channel [17], and its function is still unclear.

Because mechanosensitive channels are important in a wide variety of critical processes, it is of great interest to understand the molecular basis for their function, including their mechanisms for sensing mechanical signals and gating, which are still poorly understood. MscL is invaluable as a model system for the more complicated channels found in higher organisms. Because of its simplicity, understanding MscL and its mutants is an ideal starting point for the study of the principles of mechanosensation. An important step in achieving this goal is the development of an assay to quickly and easily screen MscL mutants, identifying the most promising for more detailed study.

Current Techniques for Studying MscL

Presently, two general techniques—patch-clamp analysis and bacterial growth studies—are used to characterize mutants of MscL. Methods have been developed for either *in vivo* or *in vitro* investigation by patch clamp [18]. For *in vivo*, bacterial cells expressing MscL are enlarged to form giant spheroplasts, allowing for patch-clamp analysis. For *in vitro*, membrane proteins isolated from bacterial preparations are reconstituted into liposomes, which form unilamellar blisters under appropriate conditions that are also suitable for patch clamping. Patch clamping is very useful

because it allows for the direct measurement of the conductance of the channels, the observation of channel opening and closing events (and therefore, kinetic analysis), and determination of the tension applied to the membrane required for channel gating [7, 17, 19]. However, spheroplast and liposome preparations are technically challenging and time consuming, making this technique impractical as a high-throughput screen.

Bacterial growth studies take less time than patch-clamping techniques and are usually the best method available for characterizing mutants [9, 20, 21]. Gain-of-function (GOF) MscL mutants either gate at lower tensions than wild type or have increased spontaneous openings, and therefore are more leaky. Since leaky channels release important intracellular materials, cells expressing GOF mutants do not grow as well as those expressing wild-type MscL in normal culture conditions. Loss-of-function (LOF) MscL mutants require more tension to open them. Hence they do not provide as adequate a defense against downshock as does wild type, and LOF mutant bacteria are more likely to be killed when subjected to downshock.

Bacterial growth analysis is easier than patch clamping for screening but is still quite labor intensive and time consuming. In addition, bacterial growth assays are only suitable for MscL mutants produced *in vivo*. However, MscL has been synthesized chemically via solid-phase synthesis and native chemical ligation [22]. A high-throughput, cell-free assay would be superior to current techniques because it would allow for more rapid screening of mutants as well as characterization of mutants synthesized *in vitro*. One possibility for such an assay is a fluorescence-based technique to detect channel activity in synthetic vesicles.

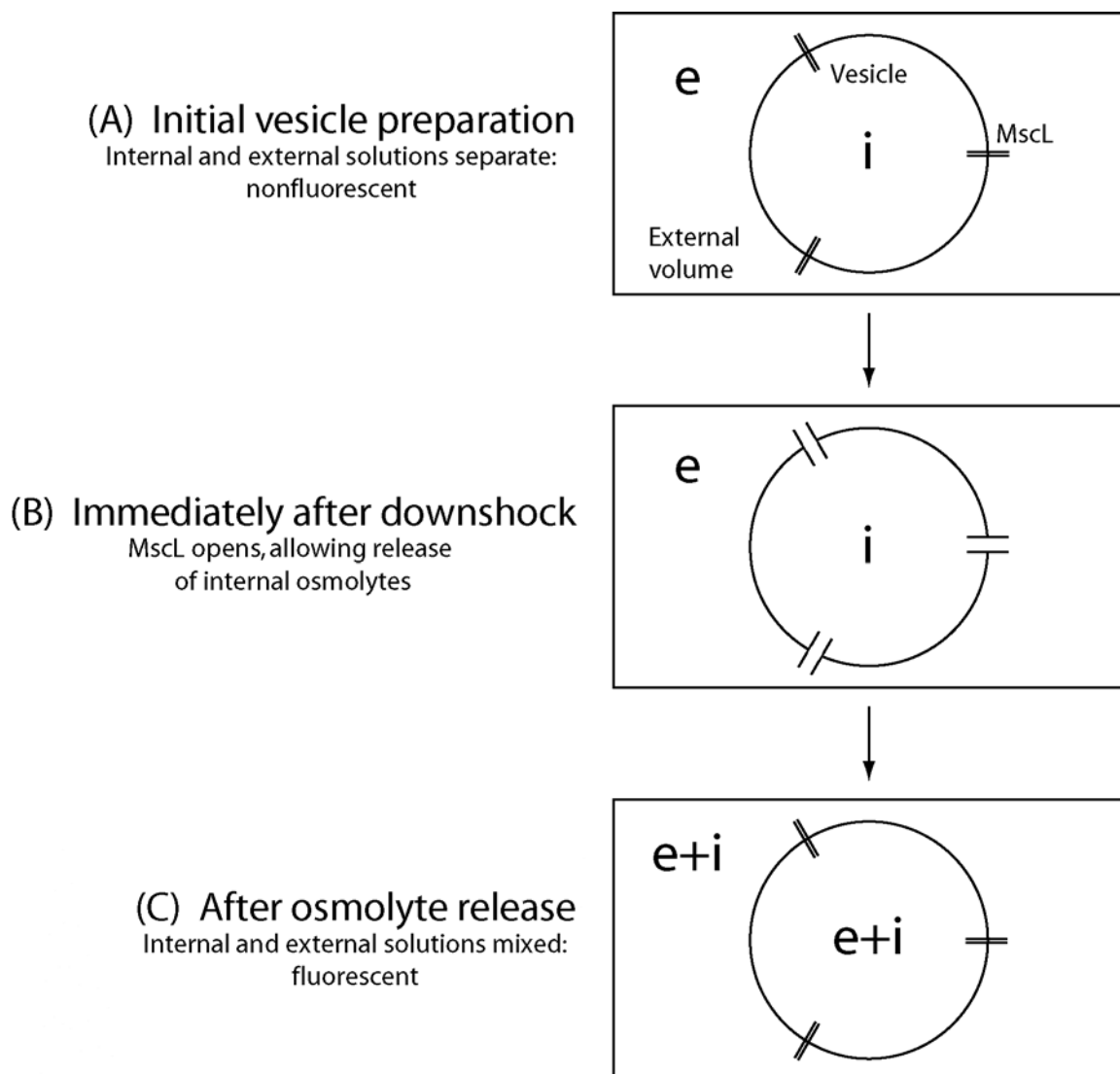


Fig. 3.3. Schematic of the proposed assay. The internal and external solutions, which are individually nonfluorescent but fluorescent when mixed, are *i* and *e*, respectively. The solutions are separate in the initial vesicle preparation (*A*), but MscL gating during downshock (*B*) opens pores in the membrane that allow the internal osmolytes to mix with the external solution (*C*).

The general scheme of the proposed fluorescence assay is outlined in fig. 3.3. The first step is the generation of a vesicle suspension that contains different solutions inside and outside the vesicles. Such a suspension can be easily prepared by forming vesicles in one solution and using gel filtration to exchange the external solution. We choose two solutions that are individually nonfluorescent but fluorescent in combination.

While the vesicles remain intact, the solutions are separate, and therefore the system is nonfluorescent. However, downshock of the vesicles results in the leakage of the interior solution (due to MscL activity or lysis) into the exterior solution, causing a sudden increase in fluorescence. Although the assay cannot directly distinguish between MscL activity and membrane rupture, MscL activity is detectable from differences in the fluorescence responses of vesicle preparations with and without the protein.

Theoretical Descriptions of Downshocked Vesicles

Laplace's Law provides the relationship between the osmotic pressure difference Δp and tension t in the vesicle membrane:

$$t = \frac{1}{2}\Delta p r \quad (3.1)$$

where r is the vesicle radius [23]. The definition of Δp is

$$\Delta p = RT\Delta c = RTD \quad (3.2)$$

where R is the ideal gas constant, T the absolute temperature, and Δc the concentration difference between the solutions inside and outside the vesicle. This equation also defines the downshock D as the concentration difference Δc . From Eq. (3.1) and Eq. (3.2), it is clear that for vesicles of a given radius, the tension is directly proportional to the downshock D .

The guiding principle of this assay is that the bilayer of a vesicle has a threshold tension, t_{thresh} , the maximum tension that it can withstand, dependent on its composition [23]. Eqs. (3.1) and (3.2) allow for the determination of the threshold downshock, D_{thresh} , corresponding to this tension. When downshocks less than D_{thresh} are applied, the vesicle remains intact. However, for greater downshocks, pores form in the vesicle, and it

releases some of its osmolytes. The release continues until the difference between the concentrations of the internal and external solutions is reduced to D_{thresh} , the largest downshock that allows the vesicle to survive intact. Fluorescence can be used to determine the fraction of the osmolytes released by the vesicles as a function of the applied downshock. This relationship allows for the determination of D_{thresh} for a preparation of vesicles.

The simplest model for this system (fig. 3.4A) consists of a uniform, spherical vesicle population with a total internal volume V_i and osmolyte concentration of $c_{i,init}$. If

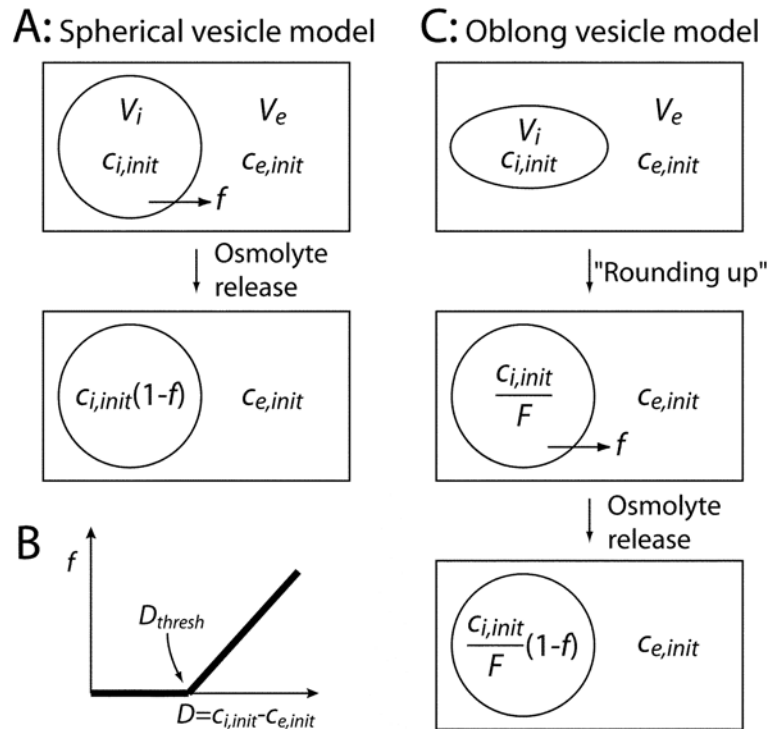


Fig. 3.4. Schematic of the models for vesicles experiencing downshock.

A, The spherical vesicle model. In an applied downshock, osmolyte release from the vesicle (circle) into the external volume changes the internal, and to a much lesser extent, the external concentrations. B, The expected function when the fraction of osmolytes released (f) is plotted against the applied downshock (D). The x -intercept of the sloped line is the threshold downshock D_{thresh} in the spherical vesicle model. C, The oblong vesicle model. The first response of an oblong vesicle (ellipse) experiencing downshock is to “round up” into a sphere. Only after this initial step are the osmolytes released as in A. The variables are explained in the text.

the number of vesicles is relatively small, V_i is much smaller than the external volume, V_e . Downshock occurs when the external osmolyte concentration is reduced to a value $c_{e,init}$ that is lower than $c_{i,init}$. The value of the applied downshock D is the initial difference between internal and external concentrations:

$$D = c_{i,init} - c_{e,init}. \quad (3.3)$$

If $D < D_{thresh}$, by definition, then no osmolytes are released, because the bilayer is strong enough to withstand the downshock. However, if $D > D_{thresh}$, then osmolytes are released. Let f be the fraction of the total intravesicular osmolyte concentration that is released from the vesicles upon downshock. The intravesicular concentration is reduced because of the outward flow of osmolytes, but the external concentration is negligibly affected because the external volume is so large compared to the internal volume.

Therefore, the final internal and external concentrations are

$$c_{i,final} = c_{i,init}(1 - f) \quad (3.4a)$$

$$c_{e,final} = c_{e,init} \quad (3.4b)$$

and the final concentration difference must be equivalent to D_{thresh} .

$$D_{thresh} = c_{i,final} - c_{e,final} \quad (3.5)$$

Combining Eqs. (3.4a), (3.4b), and (3.5) and rearranging gives

$$D_{thresh} = c_{i,init}(1 - f) - c_{e,init} \quad (3.6)$$

$$D_{thresh} = (c_{i,init} - c_{e,init}) - fc_{i,init}. \quad (3.7)$$

Combining Eqs. (3.3) and (3.7) gives

$$D_{thresh} = D - fc_{i,init}. \quad (3.8)$$

Rearranging Eq. (3.8) gives

$$f(D) = \frac{1}{c_{i,init}} D - \frac{D_{thresh}}{c_{i,init}} = mD + b \quad (3.9)$$

$$c_{i,init} = m^{-1} \quad (3.10a)$$

$$D_{thresh} = -\frac{b}{m}. \quad (3.10b)$$

The value of f must be 0 for all $D < D_{thresh}$. However, Eq. (3.9) indicates that for $D > D_{thresh}$, plotting f as a function of D should give a linear plot (fig. 3.4B). The slope m should be the reciprocal of the initial internal osmolyte concentration [Eq. (3.10a)]. D_{thresh} , which is the x -intercept of the line (fig. 3.4B), can be determined from the slope and y -intercept [Eq. (3.10b)].

A more complicated model (fig. 3.4C) also must be addressed. Vesicles prepared under some conditions are oblong, not spherical [24, 25]. In these cases, the first response of vesicles undergoing downshock is to “round up” into spheres, increasing their internal volume, and thus reducing their internal osmolyte concentration with no increase in membrane tension. The effective downshock is the difference between the *new* internal concentration and the external concentration. Let F be the factor by which the volume increases by “rounding up” (requiring $F > 1$). If the effective downshock after “rounding up” is large enough, the osmolytes are released, as in the first model. The definition of applied downshock [Eq. (3.3)] and the relationship between $c_{e,init}$ and $c_{e,final}$ [Eq. (3.4b)] are the same as in the spherical model. However, because of the change in intravesicular concentration, Eq. (3.4a) does not apply. Instead,

$$c_{i,final} = \left(\frac{c_{i,init}}{F} \right) (1 - f). \quad (3.11)$$

Now, combining Eqs. (3.4b), (3.5), and (3.11) gives

$$D_{thresh} = \left(\frac{c_{i,init}}{F} \right) (1 - f) - c_{e,init}. \quad (3.12)$$

Combining Eqs. (3.3) and (3.12) and rearranging yields

$$f(D) = \frac{F}{c_{i,init}} D + \left(1 - F - \frac{FD_{thresh}}{c_{i,init}} \right) = mD + b \quad (3.13)$$

which is again a linear function of D that allows for the determination of F and D_{thresh} .

$$F = mc_{i,init} \quad (3.14a)$$

$$D_{thresh} = \frac{1 - b}{m} - c_{i,init} \quad (3.14b)$$

In contrast to the spherical vesicle model, the oblong vesicle model requires $c_{i,init}$ in the calculation of both F and D_{thresh} , as seen in Eqs. (3.14a) and (3.14b).

The threshold downshock D_{thresh} corresponds to the downshock at which pores form in the vesicle bilayer. For vesicles composed of lipid only (–MscL vesicles), this is the downshock at which membrane rupture occurs. However, for vesicles that contain MscL (+MscL vesicles), the threshold downshock may be quite different. In these vesicles, MscL responds to the increasing tension by gating, thus opening pores at a downshock distinct from that of membrane rupture. To develop the assay for MscL gating, we must find conditions that provide distinct values for D_{thresh} for vesicles with and without MscL.

There are a number of discrete steps in the process of developing this assay. First, the best method for generating a uniform vesicle population must be determined. Second, it must be demonstrated that MscL can be incorporated into the vesicle population. Third, the fluorophore system must be optimized. Last, the vesicle composition (type of lipid and amount of protein) must be optimized. Table 3.1 shows

Table 3.1. Acronyms, names, and chemical groups of lipids.

Acronym	Full name	Headgroup ^a	Chain 1	Chain 2
chol	Cholesterol	N/A	N/A	
DLinPC	1,2-dilinolenoyl- <i>sn</i> -glycero-3-phosphocholine	PC	18:3 ^b	
DLPC	1,2-dilauroyl- <i>sn</i> -glycero-3-phosphocholine	PC	12:0	
DOPC	1,2-dioleoyl- <i>sn</i> -glycero-3-phosphocholine	PC	18:1	
DPPC	1,2-dipalmitoyl- <i>sn</i> -glycero-3-phosphocholine	PC	16:0	
POPC	1-palmitoyl-2-oleoyl- <i>sn</i> -glycero-3-phosphocholine	PC	16:0	18:1
POPE	1-palmitoyl-2-oleoyl- <i>sn</i> -glycero-3-phosphoethanolamine	PE	16:0	18:1
POPS	1-palmitoyl-2-oleoyl- <i>sn</i> -glycero-3-(phospho-L-serine)	PS	16:0	18:1

^a The headgroups include phosphatidylcholine (PC), phosphatidylethanolamine (PE), and phosphatidylserine (PS). ^b The notation m:n describing acyl chains indicates the length of the carbon chain (m) and the number of unsaturated bonds (n). Diacyl lipids have the same chain at both positions.

the types of lipids that will be considered and their acronyms, which will be used in the text.

RESULTS AND DISCUSSION

Vesicle Preparation

Both models discussed above have the important assumption that the bilayer tension in all the vesicles undergoing downshock is nearly the same and that the tension is directly proportional to the applied downshock. However, Laplace's Law [Eq. (3.1)] indicates that the proportionality only holds if all the vesicles have the same radius. Larger vesicles experience a larger tension than smaller vesicles at the same downshock, presenting a significant complication to the models. Therefore, the success of the assay depends heavily on the ability to produce a vesicle population of uniform size. Furthermore, the vesicles must be unilamellar, because the presence of MscL on the interior bilayers of multilamellar vesicles may not be detectable and the behavior of multilamellar vesicles is not well understood.

There are three commonly used methods for producing small, unilamellar vesicles: sonication, dialysis, and extrusion [26]. Sonication, which uses high frequency sound waves to break up large vesicles, produces vesicles that are so small (~30 nm in diameter) that they are osmotically insensitive. Their lack of tension changes under osmotic stress makes them unsuitable for a MscL gating assay. Vesicle preparation by dialysis involves dissolution of lipids in an aqueous detergent solution and dialyzing away the detergent [27]. Only the lipid remains, forming a vesicle suspension, but the resulting size distribution is broad. Because of the drawbacks of sonication and dialysis, the superior choice is extrusion, the passage of a lipid suspension through a filter, squeezing large vesicles into smaller ones. Extrusion can generate vesicles with sizes larger than those produced by sonication (hundreds of nm in diameter) and more narrow in size distribution than dialysis [28].

Previous work has shown extrusion filters with smaller pore sizes generate a higher fraction of unilamellar vesicles and a narrower size distribution. Vesicles extruded through a filter with 100 nm pores were shown to be almost exclusively unilamellar, whereas pore sizes of 200 and 400 nm produced populations that had increasing numbers of multilamellar vesicles [29–31]. Furthermore, 100 nm pores produced a size distribution much narrower than that of 200 nm pores, and the size distributions from 400 and 600 nm pores were multimodal, with vesicle sizes spread over a wide range [29].

Therefore, the characteristics of a vesicle population extruded through 100 nm pores, which were the smallest commercially available, appeared best suited for the assay. To confirm the previously reported size and lamellarity results, DOPC vesicles

were prepared by extrusion through 100, 600, and 1000 nm pores and analyzed by several techniques.

Dynamic light scattering (DLS), which is commonly used to determine size distributions for small particles [25, 29, 32, 33], was attempted on the vesicle preparations. However, the results were unreliable. The distributions varied widely for different vesicle samples prepared with filters of the same pore size and even for identical samples diluted to different degrees.

Because of this inconsistency, electron microscopy (EM) was used instead of DLS [24]. Vesicles prepared by extrusion were imaged by EM (fig. 3.5A–C) and their size distributions were determined (fig. 3.5D–E). Surprisingly, the 100, 600, and 1000 nm filters all yielded distributions centered at a diameter of approximately 100 nm. However, the most important difference was found not in the major peak but in the number of large vesicles. No vesicle observed in the 100 nm preparation was larger than 460 nm, while the other preparations had many vesicles larger than this, including some as large as almost 1000 nm. In addition, the large vesicles in the 600 and 1000 nm preparations tended to be multilamellar, while practically none of the vesicles in the 100 nm preparation were multilamellar, as is evident in the images. EM of other 100 nm samples prepared for different purposes (immunogold-labeled and freeze-fractured, discussed below) also showed size distributions similar to that for 100 nm in this experiment, indicating the consistency of the vesicle populations prepared by extrusion.

Therefore, it was determined that extrusion through 100 nm pores does provide a reasonably uniform population of unilamellar vesicles, making this the best of all available techniques for vesicle preparation for the desired assay.

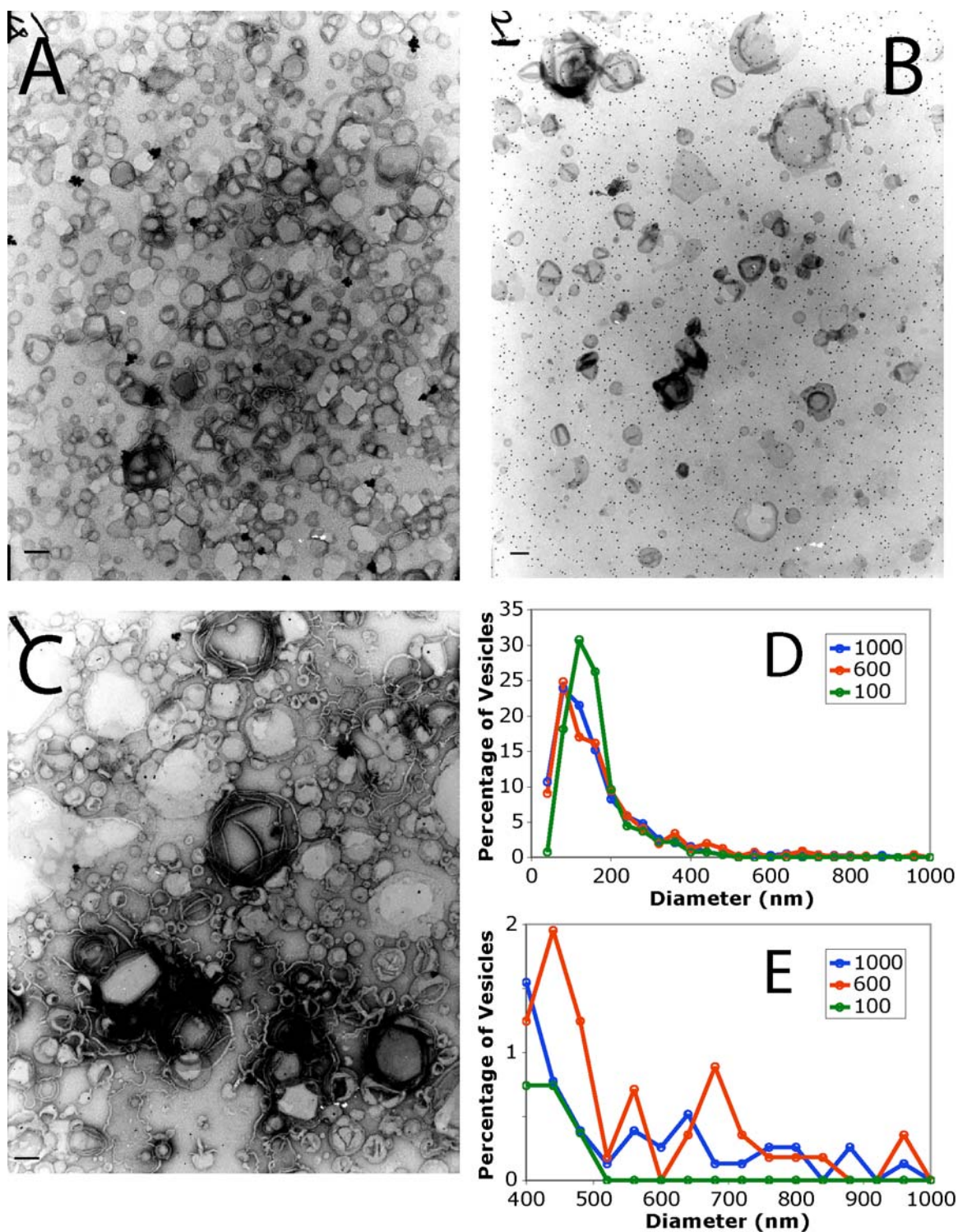


Fig. 3.5. Electron micrographs (A–C) and size distributions (D–E) of extruded vesicles. Representative micrographs showing vesicles extruded from filters with pores of 100 (A), 600 (B), and 1000 nm (C). Scale bars are 200 nm. D, The size distribution for each preparation determined from these and other images. E, An enlargement of the region with diameters greater than 400 nm. Data are the same as in D.

Verifying the Presence of MscL in Extruded Vesicles

It is extremely important to verify that MscL can be incorporated into vesicles prepared by extrusion. Therefore, MscL incorporation was verified by several different methods: Western blot, immunogold labeling, and freeze-fracture electron microscopy.

Western Blot

Because Western blotting is a standard technique for detecting small amounts of a protein with high specificity, it was the first method used to detect MscL in vesicles. In Western blotting, samples are separated during polyacrylamide gel electrophoresis (PAGE) and transferred to nitrocellulose paper, which is successively incubated with a primary antibody specific to the protein of interest and a secondary antibody specific for the primary antibody. The secondary antibody is conjugated to an easily detectable enzyme. Assaying the paper for the enzyme identifies the location of the protein of interest.

Extruded vesicles of DOPC (10 mg/mL) were prepared with and without MscL (100/1 lipid/protein) and purified by gel filtration to remove solubilized MscL from the external solution. PAGE was used to separate the components of each sample. Three lanes of each sample were run on the gel. Also, purified MscL solution was also run on the gel as a positive control; the total protein in the positive control lane was 1.5 μ g.

The protein in the gel was imaged by Western blot (fig. 3.6). The positive control showed a strong band of MscL monomer and a considerably weaker band of higher molecular weight, possibly MscL dimer (lane 1). The -MscL vesicle preparation contained no bands in any of the three lanes, as expected (lanes 5-7). The +MscL vesicle

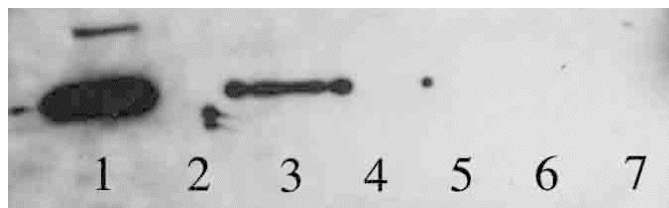


Fig. 3.6. Western blot of vesicles prepared with and without MscL. Lane 1: 1.5 μ g solubilized MscL. The MscL monomer is the large band, but a band of higher molecular weight is also present. Lanes 2–4: Vesicles prepared with MscL. Lanes 5–7: Vesicles prepared without MscL.

preparation did show a MscL band in lane 3, although it was significantly weaker than the positive control. In the other +MscL lanes (2 and 4), there were no MscL bands, but there were significant traces of MscL in both lanes as spots at the lane edge nearest to lane 3. The arrangement of the band and spots suggests that the MscL in lanes 2 and 4 is spillover from lane 3 during gel loading. Why the lanes did not all contain the same amount of protein is not clear. The fact that lane 3, not lane 2, contains the major band rules out the possibility that this band is due to spillover from misloading the positive control. Spillover would have resulted in more protein in lane 2 than lane 3. Therefore, the results suggested that at least some MscL was incorporated into the vesicles, but since there was some ambiguity, a second method for detecting incorporated MscL was used.

Immunogold Labeling

A different method to visualize MscL in vesicles is immunogold labeling. In this technique, the vesicle preparations are successively incubated with primary antibodies specific for the protein of interest and secondary antibodies specific for the primary antibody, which are covalently linked to a gold nanoparticle. Thus, the protein is labeled with a gold particle, observable by EM of the intact vesicles.

100 nm vesicles of DOPC with and without MscL were prepared by extrusion, incubated with different amounts of anti-6His mouse antibody, and then incubated with different amounts of Protein-G gold conjugate, which binds the mouse antibody. Our protein was expressed with a 6His tag at its N-terminus to simplify purification and labeling. –MscL vesicles as well as a +MscL preparation incubated without primary antibody but with Protein G represented negative controls for this experiment, because none of these vesicles was expected to bind gold particles. The final solutions were imaged by EM.

This procedure was performed several times, with different results. In some experiments, there was a clear gold labeling of the +MscL vesicles (fig. 3.7A–C). Almost all vesicles were labeled with one or more gold particles, and there were relatively few free gold particles. However, in other instances the labeling of the +MscL vesicles (fig. 3.7D) was no greater than that of the negative controls (fig. 3.7E–F). In these cases the gold particles appeared to be randomly distributed. The former results suggested the presence of MscL, but the latter suggested its absence.

Therefore, as seen in the Western blot, there is some evidence of MscL incorporation in the vesicles, but the ambiguity in the results necessitates a more definitive study.

Freeze-Fracture Electron Microscopy

Freeze-fracture EM is a definitive method for visualizing proteins embedded in membranes. Bilayers that have been flash-frozen are split relatively easily into their separate leaflets. Transmembrane proteins remain intact in one of the leaflets, resulting

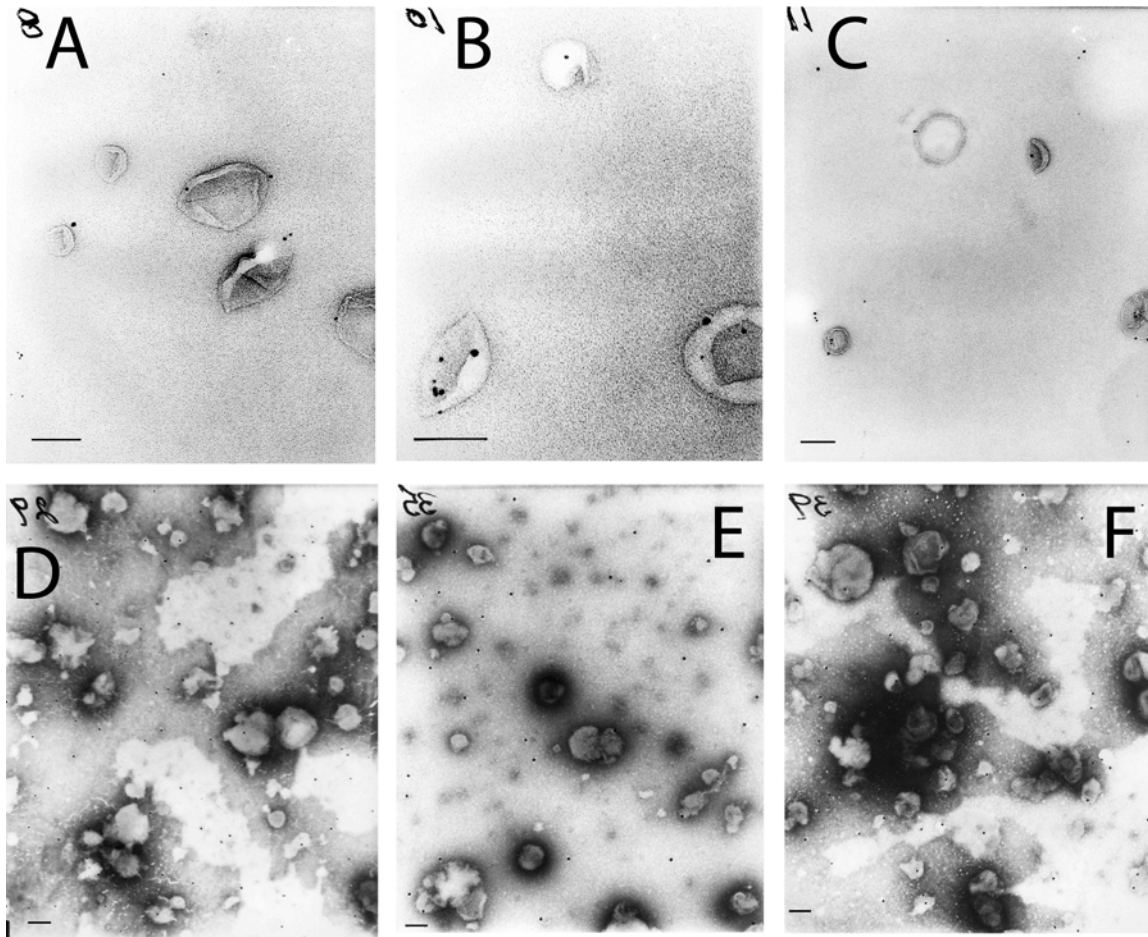


Fig. 3.7. Micrographs of immunogold-labeled vesicles. *A–C*, Representative micrographs from one experiment. All images contain +MscL vesicles labeled with 1° antibody and 2° antibody-gold particle conjugate. The small black dots are gold particles. *D–F*, Representative images from the same experiment performed later. *D*, +MscL vesicles labeled with 1° antibody and a 2° antibody-gold particle conjugate. *E*, –MscL vesicles with the same labeling. *F*, +MscL vesicles labeled with only 2° antibody-gold particle conjugate. The gold particles are associated with the vesicles in *A–C*, but in *D*, the distribution of the gold particles is no different from the negative controls *E–F*. All scale bars are 100 nm.

in a protrusion in one leaflet and a hole in the other. Visualization by EM reveals these defects.

100 nm DOPC vesicles with MscL were prepared by extrusion and analyzed by freeze-fracture EM. The images showed a large number of membrane defects likely due to protein particles in the vesicles (fig. 3.8). While a few vesicles did not contain any

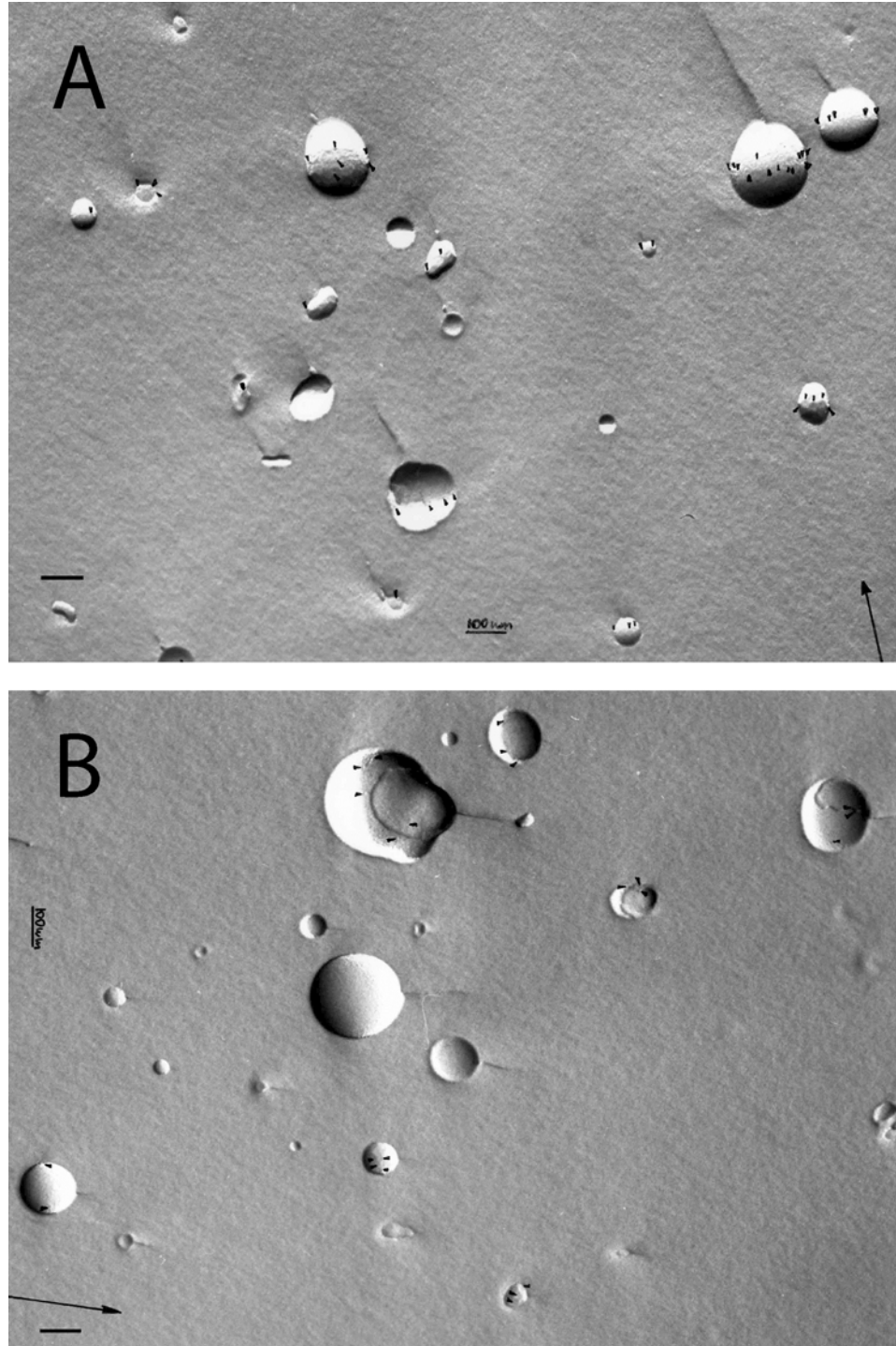


Fig. 3.8. Freeze-fracture electron micrographs of +MscL vesicles. Both images are from the same preparation. The small black arrowheads show probable protein locations. The arrows in the corners indicate the shadow direction. Scale bars are 100 nm.

visible defects, most vesicles contained more than one, with some containing more than ten.

The results here unambiguously indicated that MscL is incorporated in vesicles prepared by extrusion, laying the groundwork for further progress on the assay for MscL activity.

Evaluation of Fluorescence Systems

The assay requires solutions that are independently nonfluorescent but fluorescent when mixed (fig. 3.3). There are many solutions that satisfy this requirement, so we tried several to determine the optimal fluorescence system.

Certain fluorophores or ligands display large fluorescence increases upon binding metal ions, including fluo-3 with Tb^{3+} , calcium green 1 with Tb^{3+} or Cd^{2+} [34], and dipicolinic acid (DPA) with Tb^{3+} [35]. In principle, encapsulation of these fluorophores in vesicles and their subsequent release into an external solution of the metal ions results in a large fluorescence increase. DOPC vesicles with each of these fluorophores were prepared and tested for their usefulness in the assay. The Tb^{3+} /DPA system, which has been used in several biological applications such as endospore detection [36], vesicle fusion [37, 38], and vesicle leakage [38, 39], proved to be superior to the fluo-3 and calcium green 1 systems. The latter fluorophores are sensitive to calcium ions, and there were noticeable background signals due to calcium impurities in the intravesicular solution. The Tb^{3+} /DPA system is insensitive to other common ions, and therefore does not suffer from this complication. Vesicles encapsulating Tb^{3+} that were purified by gel

filtration to replace the external solution with one containing DPA were always free of background fluorescence.

Another system that was also considered involved carboxyfluorescein (CF), a self-quenching fluorophore, which has been used previously in several vesicle leakage assays [24, 40–42]. This molecule is highly fluorescent in dilute concentrations but self-quenching at very high concentrations [34]. Vesicles loaded with high concentrations of CF (100 mM) have no detectable fluorescence, but release from the vesicles results in a dilute, fluorescent external CF solution.

Because both the Tb^{3+} /DPA and CF systems met the requirements for this assay—two nonfluorescent solutions that increased in fluorescence on mixing—both of them were used. Early experiments utilized Tb^{3+} /DPA before CF was explored as an alternative. But later experiments used CF because it possessed two advantages over Tb^{3+} /DPA. First, gel filtration of the vesicles, an essential step that exchanges the extravascular solution, was easier for CF than for Tb^{3+} /DPA. Tb^{3+} and DPA are both colorless, but CF appears brown at high concentrations and green at low concentrations. Therefore, the progress of the vesicles and the free CF in the column could be followed much more easily. Second, in the absence of a chelator, Tb^{3+} has been shown to change the fluidity characteristics of phosphatidylserine (PS) when encapsulated in PS vesicles [37]. Citrate was used as a chelator in the experiments in order to minimize the association of Tb^{3+} with the lipids, but the use of CF avoided this complication entirely.

Optimization of Vesicle Composition—Lipid Composition

Using the optimized vesicle preparation technique and fluorescence systems, vesicles of various types of lipids were investigated in the downshock assay to optimize the lipid system. Ideally, the conditions should result in a large difference in the D_{thresh} values for +MscL and –MscL vesicles, requiring a lipid system with a large difference between the tensions for MscL gating and membrane rupture.

In general, much more is known about membrane rupture than MscL gating in different lipid types. The stability of pure bilayers strongly depends on the melting temperature (T_m) of the lipids [43]. The melting temperature, in turn, depends on the degree of unsaturation in the lipid tails [44, 45]. Lipids with unsaturated tails tend to have lower melting temperatures and are more easily ruptured, while saturated lipids can generally withstand higher membrane tensions.

In contrast, there is very little experimental data on the gating behavior of MscL in different lipid environments. Patch-clamping experiments on MscL have been performed in only two lipid environments, the natural bacterial membrane and the lipid mixture soybean azolectin [18]. Also, while there is a working model for the MscL gating mechanism and the protein/lipid interactions involved [3, 46], it is still relatively unsophisticated. It does not detail any specific roles for the headgroups or unsaturation in the lipid tails.

To complicate matters further, tensions in membranes are not straightforward to determine experimentally, as they depend on both the pressure and the radius of curvature [Laplace's Law, Eq. (3.1)]. In short, it was impossible to predict *a priori* the lipid system

Lipid	T_m (°C)	Ref.
DLinPC	-60	44
DOPC	-20	44
POPC	-2	44
80/20 DOPC/DPPC	12	45
40/60 DOPC/DPPC	30	45

Table 3.2. Melting temperatures (T_m) of lipids and lipid mixtures.

that provides the best conditions for this assay. Therefore, many lipids were tested to determine the optimal lipid or mixture by trial and error.

Membrane Fluidity

First, vesicles were prepared of lipids and lipid mixtures across a broad range of melting temperatures, which are summarized in table 3.2. 100 nm vesicles with and without MscL (1000/1 lipid/protein) were prepared in CF rehydration buffer, and the external solution was replaced with exchange buffer by gel filtration. The vesicle preparations were subjected to a serial downshock protocol.

The data are summarized in fig. 3.9. Each plot of the fraction of osmolytes released versus the downshock had the shape predicted by the theoretical models: very little release of osmolytes for all downshocks less than some threshold, and a linear release for greater downshocks (fig. 3.9A–E). The lines of best fit were determined for the linear release for each vesicle sample, which allowed for the determination of D_{thresh} and other parameters, according to the above equations describing the two models. The data are summarized in table 3.3.

The results indicated that the oblong vesicle model was not an accurate description of the system. The results contradict the model's assumption that the vesicles increase their net volume by "rounding up" in response to osmotic downshock. If

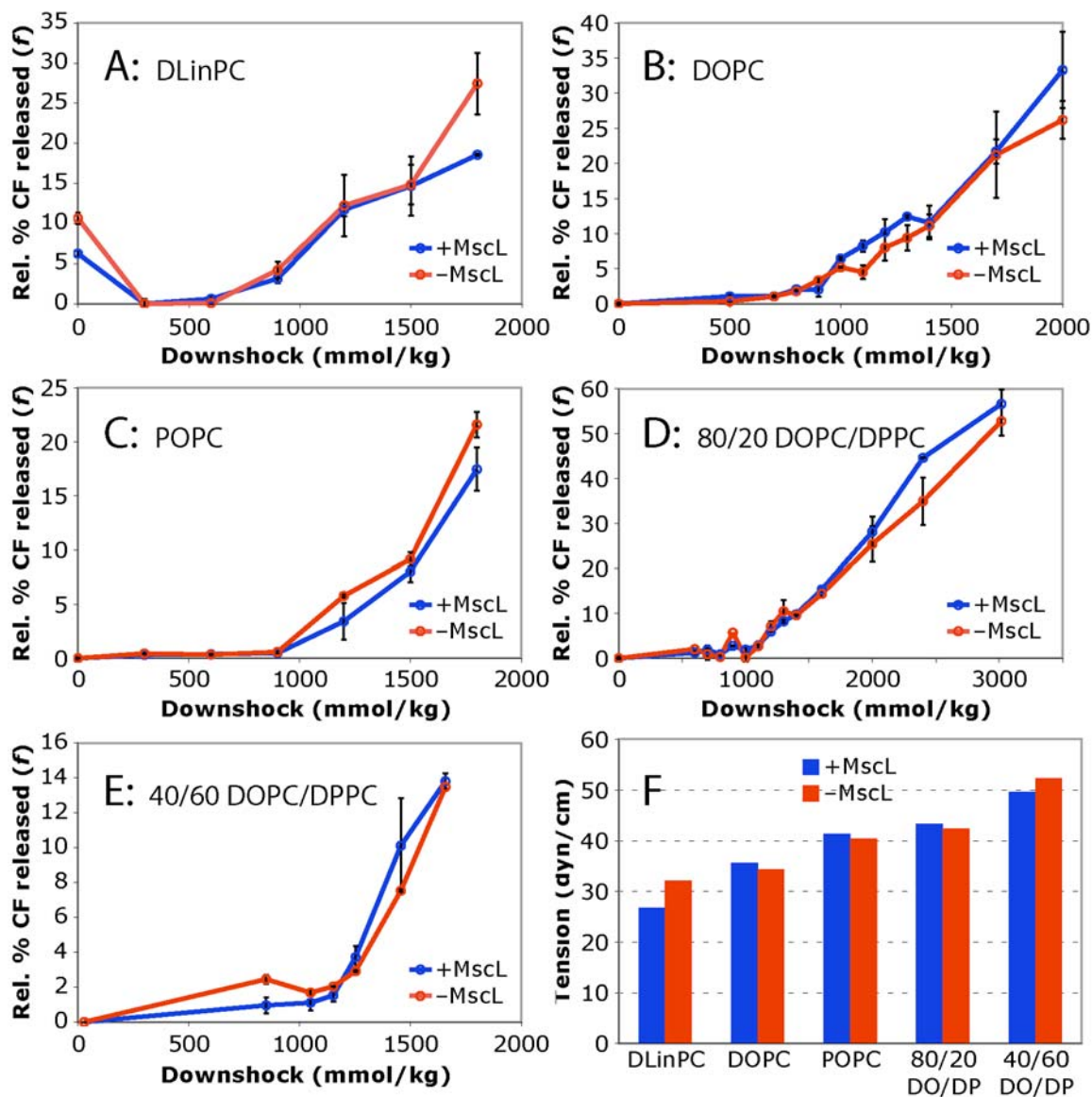


Fig. 3.9. Fraction of released osmolytes versus applied downshock for lipid mixtures with different melting temperatures. *A*, DLinPC. *B*, DOPC. *C*, POPC. *D*, 80/20 (m/m) DOPC/DPPC. *E*, 40/60 (m/m) DOPC/DPPC. *F*, The calculated threshold tensions for osmolyte release for each vesicle preparation. As expected, the tensions increase monotonically with the lipid T_m , but there are no appreciable differences between the tensions for the vesicles with and without MscL for each lipid. Error bars in *A–E* are the standard errors of the mean.

“rounding up” occurred, then the parameter F , which is the factor by which the volume increases, must be greater than 1. However, the analysis of all vesicles samples gave a value of F of less than 1, by a significant amount in most cases, implying a decrease in

Table 3.3. Analysis of serial downshock experiments, varying the lipid.

Vesicle Composition	m	b	Oblong Vesicle Model		Spherical Vesicle Model				
			F	D_{thresh} mmol/kg	Calc. $c_{i,init}$ mmol/kg	D_{thresh} mmol/kg	% Diff $c_{i,init}$	t_{thresh} dyn/cm	
DLinPC	+	0.0164	-10.129	0.525	3520	6100	618	90.5	26.8
	-	0.0241	-17.868	0.771	1690	4150	741	29.7	32.1
DOPC	+	0.0262	-21.554	0.838	1440	3820	823	19.3	35.7
	-	0.0212	-16.807	0.678	2310	4720	793	47.4	34.4
POPC	+	0.0185	-17.634	0.592	3160	5410	953	68.9	41.3
	-	0.0221	-20.619	0.707	2260	4530	933	41.4	40.4
80/20 DOPC/DPPC	+	0.0289	-28.883	0.925	1260	3460	999	8.13	43.3
	-	0.0253	-24.747	0.810	1730	3950	978	23.5	42.4
40/60 DOPC/DPPC	+	0.0251	-27.347	0.803	1870	3980	1090	24.5	49.6
	-	0.0261	-29.986	0.835	1780	3830	1150	19.7	52.3
55/45 POPC/chol	+	0.0164	-12.406	0.525	3650	6100	756	90.5	32.8
	-	0.0181	-12.029	0.579	2990	5520	665	72.7	28.8
37/33/30 DOPC/ DPPC/chol	+	0.0262	-20.970	0.838	1420	3820	800	19.3	34.7
	-	0.0237	-19.275	0.758	1830	4220	813	31.9	35.3

The + and – signs indicate the presence or absence of MscL. m , b , F , D_{thresh} , $c_{i,init}$, and t_{thresh} are defined in the text in the theoretical description of the vesicle models; calc. $c_{i,init}$ is the value of $c_{i,init}$ calculated from Eq. (3.10a); % diff. $c_{i,init}$ is the percent difference between this calculated value and the actual $c_{i,init}$; t_{thresh} is calculated from D_{thresh} and Eqs. (3.1) and (3.2), assuming a vesicle diameter of 100 nm.

the effective volume of the vesicles. It is counterintuitive that vesicles experiencing downshock would shrink, and it is incompatible with the model.

Analysis by the spherical vesicle model, on the other hand, gave more intuitive results. First, the model states that the reciprocal of the slope is the initial intravesicular osmolality. The errors in the predicted osmolality from the actual value (~3200 mmol/kg) are reasonably low (within 30%) in most cases, and there are legitimate reasons for the large errors. Specifically, the lines for the POPC vesicle samples were drawn from only three data points each, the fewest of any sample, so the error in the slopes may have been reduced with more data. Also, the line for the DLinPC +MscL sample was most likely skewed by the data point at 1800 mmol/kg, which does not fit very well with the rest of the DLinPC data. Second, the values for the threshold tension

as calculated by this model increase monotonically with the lipid T_m (fig. 3.9F), which agrees with the literature [44]. Furthermore, these tensions are not far from the 40 dyn/cm tension threshold determined previously for several lipid mixtures [24, 47], although other reports claim significantly lower tension thresholds [32, 43].

For these reasons, the values for D_{thresh} from analysis by the spherical vesicle model are the values reported for the vesicle samples. Unfortunately, none of the lipids display significant differences in D_{thresh} for +MscL and -MscL vesicles, which is not surprising given the way the plots for all lipids overlay each other.

Further experiments were performed using mixtures of lipids and cholesterol, which stiffens membranes and alters their fluidity properties. Experiments were performed exactly as above, except the lipid mixtures were 55/45 POPC/chol and 37/33/30 DOPC/DPPC/chol. The results (fig. 3.10 and table 3.3), as before, show no appreciable differences between +MscL and -MscL vesicles. Thus, using a series of lipids and lipid mixtures with different membrane fluidities failed to provide a lipid system that could differentiate the activity of MscL from membrane rupture.

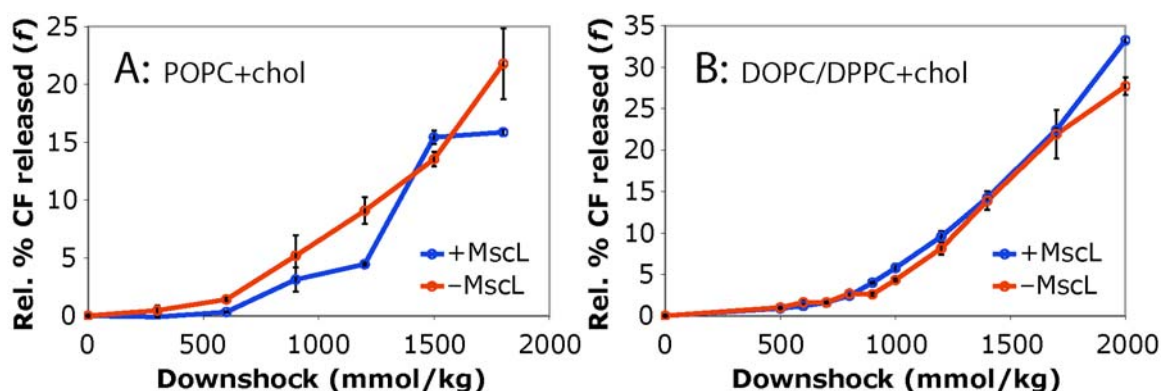


Fig. 3.10. Fraction of released osmolytes versus applied downshock for lipid mixtures containing cholesterol. *A*, 55/45 (m/m) POPC/chol. *B*, 37/33/30 (m/m) DOPC/DPPC/chol. There are no appreciable differences for vesicles with and without MscL. Error bars are standard errors of the mean.

Shorter Lipid Tails

Previous work has shown that MscL has a lower gating tension in lipids with shorter lipid tails [48, 49]. For this reason, +MscL and –MscL vesicles were prepared with DLPC as above. This lipid was found to be unsuitable for the assay because the intravesicular volume after extrusion was very low. It is not clear if this is because the vesicles are very small or few in number. In either case, because of the low signals that resulted from downshock, the data were too noisy to be rigorously analyzed.

Different Headgroups

Lipids with different headgroups—POPS and 50/50 POPE/POPS—were used in the preparation of vesicles with and without MscL, as above, except the fluorescence system chosen was Tb³⁺/DPA instead of CF. These lipids were found to be unsuitable, however, because the vesicles of these compositions were leaky. Even in the absence of any downshock whatsoever, a large amount of background fluorescence was observed. It is not clear why the contents leaked from the vesicles, but such leakage is incompatible with the assay.

Natural Lipid Mixtures

Two natural lipid mixtures, soybean azolectin and *E. coli* membrane extract, were also used. These mixtures were chosen because MscL reconstituted into azolectin has been used in all *in vitro* patch-clamp experiments [18], and the membrane extract from *E. coli* provides as close a match as possible to the native environment of MscL. Vesicles of

these lipid mixtures were prepared with and without MscL as above to determine their suitability for the assay.

The downshock results for +MscL and –MscL vesicles of azolectin, which consists of a mixture of various diacylphosphatidylcholines, were indistinguishable, as seen for all previous lipid systems, and therefore provided no advantage for the assay.

Vesicles prepared from *E. coli* extract, which consists of 57.5% phosphatidylethanolamine, 15.1% phosphatidylglycerol, 9.8% cardiolipin, and 17.6% other lipids, were unsuitable because of problems with their purification. When purified using gel filtration, they became stuck in the column, never eluting. This occurred using beads of two different materials, Sephadex (dextran) and Biogel (polyacrylamide). Purification of the vesicles was also attempted using dialysis, but this was prohibitively time consuming. Using small volume dialyzers to perform the dialysis, there was only partial buffer exchange even after 72 hours. Because the exchange of the external solutions is an absolute requirement for the assay, *E. coli* extract could not be used.

Optimization of Vesicle Composition—Protein Amount

It is possible, although unlikely, that the downshock assay could not detect MscL activity because a lipid/protein ratio of 1000/1 results in only a few channels in each vesicle. The freeze-fracture EM images indicated that many vesicles had only two or three channels (fig. 3.8). Therefore, the effects of using different amounts of protein were also explored.

DOPC vesicles were prepared with lipid/protein ratios of 2000/1, 1000/1, and 400/1, and with no protein, purified, and subjected to a serial downshock protocol.

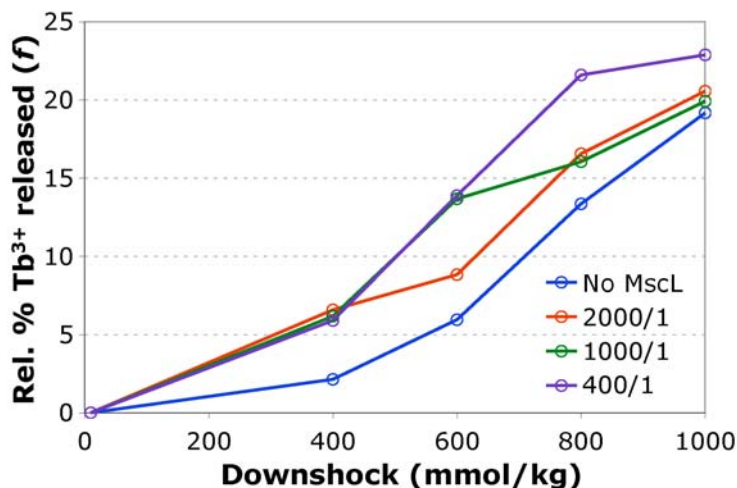


Fig. 3.11. Fraction of released osmolytes versus applied downshock for vesicles containing different amounts of protein. The lipid/protein ratio for each sample is given.

Tb³⁺/DPA instead of CF was used for this experiment. The results are shown in fig. 3.11 and table 3.4.

The data in this experiment appear to indicate that vesicles with any amount of MscL have lower D_{thresh} values than –MscL vesicles. However, the D_{thresh} values for the 1000/1 and –MscL samples differ significantly from those observed in previous experiments (table 3.3). Because the previous data fit with the expected relationship between threshold tensions and T_m , these results are probably not quantitatively accurate. However, the key finding is that having more or less MscL than in the previous experiments did not alter the D_{thresh} value substantially.

Table 3.4. Spherical vesicle model analysis of serial downshock experiments, varying the amount of protein

Lipid/Protein	m	b	Calc. $c_{i,init}$ mmol/kg	D_{thresh} mmol/kg
400/1	0.0293	–4.4603	3410	152
1000/1	0.0218	–1.3126	4590	60.2
2000/1	0.0248	–4.2538	4030	172
No MscL	0.0292	–10.315	3420	353

In summary, no vesicle composition tested produced vesicles that allowed for the detection of MscL activity. For some lipids, the vesicles could not even be produced and purified, as required for the assay. For others, the expected decrease in the downshock threshold values of vesicles with MscL compared to those without MscL was not observed. Also, changing the amount of MscL did not lead to this decrease, either.

CONCLUSION

The development of a high-throughput fluorescence-based assay for MscL activity involved several steps: determining the optimal method for vesicle formation, assuring the presence of MscL in vesicles prepared by this method, determining the optimal fluorescence system, and finding a vesicle composition that allows for MscL detection under downshock conditions. However, the final goal of detecting MscL activity was never met. There are two main possible reasons for the failure of this assay.

The simplest explanation is that MscL was never incorporated into the vesicles. If this were true, then the alleged +MscL vesicle samples were actually no different from the –MscL samples, and it is not surprising that the downshock results never reported any difference. However, this is improbable. While detection of MscL in the vesicles samples by Western blot and immunogold staining was somewhat ambiguous, the most rigorous detection technique—freeze-fracture EM—supported MscL incorporation. Furthermore, the method utilized here has been used previously to reconstitute MscL for patch clamp experiments on larger vesicles, which indisputably demonstrated MscL incorporation [50].

The more likely explanation for the failure of the assay is the inability to produce a sufficiently uniform vesicle sample. The uniformity demanded by an assay for MscL gating may be unattainable by current techniques for producing vesicles. Because the gating tension for MscL is relatively close to the membrane lysis tension, and tension depends directly on the vesicle radius, both phenomena may occur at the same downshock within a population of vesicles, even with a narrow size distribution. Even extrusion through 100 nm pores, the best technique for producing vesicles, resulted in a distribution with a full-width, half-maximum of about 100 nm, and almost 5% of the vesicles had diameters of more than 300 nm (fig. 3.5D–E).

The fact that extrusion may produce a vesicle population that varies not just in size, but in shape as well, is a further complication [24]. The failure of the oblong vesicle model presented earlier to adequately describe the experimental vesicle system does not imply that oblong vesicles do not exist. It is possible that the flaw in the model comes from the oversimplifying assumption that all oblong vesicles are produced with the same ratio of surface area to volume.

It was determined that this project was not worth continuing for two reasons. First, the development of a vesicle-based assay for MscL activity must wait for the development of better techniques for producing uniform vesicle populations. Given the current techniques, no further progress could be made. Second, a separate fluorescence-based bacterial growth assay for screening MscL mutants was developed that rendered the vesicle-based assay obsolete [51]. The only application requiring a vesicle-based assay was the screening of chemically synthesized MscL mutants, and although MscL has been chemically synthesized previously, it is not an area of current research.

MATERIALS AND METHODS

Materials

Most lipids (dissolved in chloroform at concentrations of 20–25 mg/mL), the Mini-Extruder, and the extruder heating block were purchased from Avanti Polar Lipids (Alabaster, AL). Soybean azolectin was purchased from Sigma as a lyophilized powder and was dissolved in chloroform to a concentration of 25 mg/mL before use. Sucrose, NaCl, KCl, and sodium citrate were purchased from Mallinckrodt (St. Louis, MO). MOPS, cholic acid, DPA, and Sephadex G-50 (fine grade) were purchased from Sigma. Carboxyfluorescein (CF) was purchased from Molecular Probes (Eugene, OR). $TbCl_3$ was purchased from Fluka. Mouse anti-6His antibody was purchased from Covance/BAbCo, and the Protein G-gold conjugate was purchased from BBIInternational (Cardiff, Wales). Purified *E. coli* MscL protein was a generous gift from the lab of Douglas Rees [15]. The protein, solubilized in 0.05% β -dodecylmaltoside (DDM), had a concentration of approximately 15 mg/mL. There was a 6His tag at its N-terminus so that it could be easily purified and labeled.

For the CF fluorescence system, high osmolality exchange buffer contained 1000 mM sucrose, 950 mM NaCl, and 10 mM MOPS, pH 7.8. High osmolality rehydration buffer contained 1000 mM sucrose, 750 mM NaCl, 100 mM CF, and 10 mM MOPS, pH 7.8. The osmolalities of the exchange and rehydration buffers were matched at ~3200 mmol/kg. Low osmolality downshock buffer contained only 10 mM MOPS, pH 7.8 (osmolality 30 mmol/kg). Detergent buffer consisted of 20 mM cholic acid in high osmolality exchange buffer. For the Tb^{3+} /DPA fluorescence system, high osmolality rehydration buffer contained 18 mM $TbCl_3$, 180 mM sodium citrate, 600 mM

sucrose, and 10 mM MOPS, pH 7.2. High osmolality exchange buffer contained 3 mM DPA, 800 mM sucrose, 100 mM KCl, and 10 mM MOPS, pH 7.2. The osmolalities were matched at ~1200 mmol/kg. Low osmolality downshock buffer contained 3 mM DPA and 10 mM MOPS, pH 7.2 (osmolality 38 mmol/kg). Detergent buffer consisted of 20 mM cholic acid in high osmolality exchange buffer.

Vesicle Preparation

750 μ L of lipid solution (15 mg total lipid) was placed in a round-bottom flask. The chloroform was removed by rotary evaporation to yield a thin lipid film on the flask bottom. The film was dried further under high vacuum for 8–12 hours. For vesicle preparations with MscL, 1 μ L of MscL solution (~15 μ g, a 1000/1 lipid/protein ratio) was applied to the dried lipid and agitated to reconstitute the protein in the lipid molecules. Other ratios were sometimes used, as indicated in the text. For vesicle preparations without MscL, 1 μ L of 0.05% DDM solution was applied as a control for the DDM in the MscL solution. The lipid film (or lipid/protein mixture) was rehydrated in 5 mL rehydration buffer, giving a lipid concentration of 3 mg/mL in the final suspension. For vesicles that were produced for purposes other than downshock (e.g., electron microscopy), exchange buffer was used instead of rehydration buffer. The flask was agitated until all the lipid was removed from the side of the flask and rehydrated in the buffer, and the suspension was subjected to 3–5 freeze-thaw cycles at -80 °C. Extrusion was performed using the Avanti Mini-Extruder. 1 mL of the suspension was pulled into one of the pair of extruder syringes and passed back and forth 31 times through a polycarbonate filter with pore sizes of 100, 600, or 1000 nm. For lipids that have a T_m

higher than room temperature, the rehydration and extrusion were carried out in the extruder heating block at 50 °C to maintain fluidity.

Gel filtration was used to exchange the solution outside the vesicles. A gel filtration column of fine grade Sephadex G-50 was prepared in exchange buffer with a bed volume about ~10 mL. As the vesicle suspension passed through the column, the vesicles remained in the void volume and were eluted more quickly than the solutes that were free in solution. The vesicle suspension eluted from the column still had rehydration buffer inside, but now had exchange buffer outside. After the application of the vesicle suspension, at least five bed volumes of exchange buffer were flowed through the filtration column to eliminate all traces of the rehydration buffer.

Electron Microscopy

Vesicles were prepared in exchange buffer. A drop of vesicle suspension was placed in a charged gold grid and allowed to sit for 30 seconds. The solution was then dried from the grid by dabbing with the corner of a slice of filter paper. The dried grid was stained with uranyl acid or phosphotungstic acid solution, which was also allowed to sit for 30 seconds before the solution was dried by the same method. The grids were imaged with a scanning electron microscope.

Freeze-fracture EM was performed at Nano Analytical Laboratory (San Francisco, CA).

Immunogold Labeling

Vesicles with and without MscL were prepared in exchange buffer. 300 μL of +MscL vesicle suspension were incubated with 0, 0.3, or 0.6 μL primary antibody solution (0, 1/1000, or 1/500 dilutions). The 1/500 sample was prepared in duplicate. The incubation times were 45 minutes and 75 minutes for the 1/500 and 1/1000 samples, respectively. The primary antibody was a mouse IgG monoclonal antibody specific for the 6His tag, which the protein has at its N-terminus. After incubation, the vesicle samples were purified of unbound antibody by gel filtration. 300 μL of the three vesicle samples were incubated with 6 μL secondary antibody (1/50 dilution) for 45 minutes. In addition, the second 1/500 dilution sample was incubated with 3 μL secondary antibody (1/100 dilution) for 75 minutes. The secondary antibody was Protein-G conjugated to a 10 nm gold particle. As a negative control, -MscL vesicles were also incubated with a 1/500 dilution of primary antibody followed by 1/50 dilution of secondary antibody, as above.

Serial Downshock Protocol

High osmolality exchange buffer and low osmolality downshock buffer were mixed in various proportions to produce solutions of intermediate osmolalities. 5 μL of the purified vesicle preparations were subjected to downshock by dilution in 195 μL of these intermediate solutions in a 96-well plate. In addition, 5 μL of the purified vesicle preparations were also applied to 195 μL detergent buffer, which dissolved the lipids and freed the encapsulated osmolytes. A SpectraMax Gemini XS fluorescence plate reader (Molecular Devices, Sunnyvale, CA) using SOFTmax PRO 3.1.2 software was used to

measure the fluorescence of each sample for 60 minutes, allowing the fluorescence to stabilize. For the CF fluorescence system, the excitation wavelength was 492 nm, and emitted light was filtered at 515 nm and read at 520 nm with low PMT sensitivity. For the Tb³⁺/DPA fluorescence system, the excitation and emission wavelengths were 287 and 544 nm, respectively, and medium PMT sensitivity was used.

Data Analysis

Each raw fluorescence measurement was converted to a fluorophore concentration by comparison with standard curves. For each downshocked sample, the ratio of the fluorophore concentration to that of the corresponding detergent-treated sample was calculated to determine the fraction of the osmolytes released during downshock. The relative released fraction for each sample was determined by subtracting the minimum value for the downshock series. The relative released fraction was then plotted as a function of the applied downshock and analyzed according to the spherical and oblong vesicle models.

It should be noted that in experiments using the CF fluorescence system, after treatment with detergent, the CF concentrations ranged from 1 to 5 μM . This represents a 10^4 - to 10^5 -fold dilution of the initial intravesicular CF concentration of 100 mM. Therefore, the total volume of the solution is 10^4 - to 10^5 -fold greater than the intravesicular volume, which justifies the assumption of Eq. (3.4b) that the intravesicular volume is negligible compared to the external volume.

REFERENCES

1. Martinac, B. 2004. Mechanosensitive ion channels: Molecules of mechanotransduction. *J. Cell Sci.* 117:2449-2460.
2. Strop, P., R. Bass, and D. C. Rees. 2003. Prokaryotic mechanosensitive channels. *Adv. Protein Chem.* 63:177-209.
3. Hamill, O. P., and B. Martinac. 2001. Molecular basis of mechanotransduction in living cells. *Physiol. Rev.* 81:685-740.
4. Sukharev, S. I., P. Blount, B. Martinac, and C. Kung. 1997. Mechanosensitive channels of *Escherichia coli*: The MscL gene, protein, and activities. *Annu. Rev. Physiol.* 59:633-657.
5. Berrier, C., M. Besnard, B. Ajouz, A. Coulombe, and A. Ghazi. 1996. Multiple mechanosensitive ion channels from *Escherichia coli*, activated at different thresholds of applied pressure. *J. Membr. Biol.* 151:175-187.
6. Levina, N., S. Totemeyer, N. R. Stokes, P. Louis, M. A. Jones, and I. R. Booth. 1999. Protection of *Escherichia coli* cells against extreme turgor by activation of MscS and MscL mechanosensitive channels: Identification of genes required for MscS activity. *EMBO J.* 18:1730-1737.
7. Sukharev, S. I., W. J. Sigurdson, C. Kung, and F. Sachs. 1999. Energetic and spatial parameters for gating of the bacterial large conductance mechanosensitive channel, MscL. *J. Gen. Physiol.* 113:525-540.
8. Sukharev, S. I., P. Blount, B. Martinac, F. R. Blattner, and C. Kung. 1994. A large-conductance mechanosensitive channel in *E. coli* encoded by *mscL* alone. *Nature.* 368:265-268.
9. Maurer, J. A., D. E. Elmore, H. A. Lester, and D. A. Dougherty. 2000. Comparing and contrasting *Escherichia coli* and *Mycobacterium tuberculosis* mechanosensitive channels (MscL). New gain of function mutations in the loop region. *J. Biol. Chem.* 275:22238-22244.
10. Anishkin, A., V. Gendel, N. A. Sharifi, C. S. Chiang, L. Shirinian, H. R. Guy, and S. Sukharev. 2003. On the conformation of the COOH-terminal domain of the large mechanosensitive channel MscL. *J. Gen. Physiol.* 121:227-244.
11. Ajouz, B., C. Berrier, A. Garrigues, M. Besnard, and A. Ghazi. 1998. Release of thioredoxin via the mechanosensitive channel MscL during osmotic downshock of *Escherichia coli* cells. *J. Biol. Chem.* 273:26670-26674.

12. Berrier, C., A. Garrigues, G. Richarme, and A. Ghazi. 2000. Elongation factor Tu and DnaK are transferred from the cytoplasm to the periplasm of *Escherichia coli* during osmotic downshock presumably via the mechanosensitive channel mscL. *J. Bacteriol.* 182:248-251.
13. Vazquez-Laslop, N., H. Lee, R. Hu, and A. A. Neyfakh. 2001. Molecular sieve mechanism of selective release of cytoplasmic proteins by osmotically shocked *Escherichia coli*. *J. Bacteriol.* 183:2399-2404.
14. Cruickshank, C. C., R. F. Minchin, A. C. Le Dain, and B. Martinac. 1997. Estimation of the pore size of the large-conductance mechanosensitive ion channel of *Escherichia coli*. *Biophys. J.* 73:1925-1931.
15. Chang, G., R. H. Spencer, A. T. Lee, M. T. Barclay, and D. C. Rees. 1998. Structure of the MscL homolog from *Mycobacterium tuberculosis*: a gated mechanosensitive ion channel. *Science.* 282:2220-2226.
16. Blount, P., S. I. Sukharev, P. C. Moe, M. J. Schroeder, H. R. Guy, and C. Kung. 1996. Membrane topology and multimeric structure of a mechanosensitive channel protein of *Escherichia coli*. *EMBO J.* 15:4798-4805.
17. Blount, P., S. I. Sukharev, M. J. Schroeder, S. K. Nagle, and C. Kung. 1996. Single residue substitutions that change the gating properties of a mechanosensitive channel in *Escherichia coli*. *Proc. Natl. Acad. Sci. USA.* 93:11652-11657.
18. Blount, P., S. I. Sukharev, P. C. Moe, B. Martinac, and C. Kung. 1999. Mechanosensitive channels of bacteria. *Methods Enzymol.* 294:458-482.
19. Sukharev, S. I., B. Martinac, V. Y. Arshavsky, and C. Kung. 1993. Two types of mechanosensitive channels in the *Escherichia coli* cell envelope: Solubilization and functional reconstitution. *Biophys. J.* 65:177-183.
20. Ou, X., P. Blount, R. J. Hoffman, and C. Kung. 1998. One face of a transmembrane helix is crucial in mechanosensitive channel gating. *Proc. Natl. Acad. Sci. USA.* 95:11471-11475.
21. Yoshimura, K., A. Batiza, M. Schroeder, P. Blount, and C. Kung. 1999. Hydrophilicity of a single residue within MscL correlates with increased channel mechanosensitivity. *Biophys. J.* 77:1960-1972.
22. Clayton, D., G. Shapovalov, J. A. Maurer, D. A. Dougherty, H. A. Lester, and G. G. Kochendoerfer. 2004. Total chemical synthesis and electrophysiological characterization of mechanosensitive channels from *Escherichia coli* and *Mycobacterium tuberculosis*. *Proc. Natl. Acad. Sci. USA.* 101:4764-4769.
23. Hallett, F. R., J. Marsh, B. G. Nickel, and J. M. Wood. 1993. Mechanical properties of vesicles. II. A model for osmotic swelling and lysis. *Biophys. J.* 64:435-442.

24. Mui, B. L., P. R. Cullis, E. A. Evans, and T. D. Madden. 1993. Osmotic properties of large unilamellar vesicles prepared by extrusion. *Biophys. J.* 64:443-453.
25. White, G., J. Pencer, B. G. Nickel, J. M. Wood, and F. R. Hallett. 1996. Optical changes in unilamellar vesicles experiencing osmotic stress. *Biophys. J.* 71:2701-2715.
26. Szoka, F., Jr., and D. Papahadjopoulos. 1980. Comparative properties and methods of preparation of lipid vesicles (liposomes). *Annu. Rev. Biophys. Bioeng.* 9:467-508.
27. Paternostre, M. T., M. Roux, and J. L. Rigaud. 1988. Mechanisms of membrane protein insertion into liposomes during reconstitution procedures involving the use of detergents. 1. Solubilization of large unilamellar liposomes (prepared by reverse-phase evaporation) by triton X-100, octyl glucoside, and sodium cholate. *Biochemistry.* 27:2668-2677.
28. Szoka, F., F. Olson, T. Heath, W. Vail, E. Mayhew, and D. Papahadjopoulos. 1980. Preparation of unilamellar liposomes of intermediate size (0.1-0.2 μmol) by a combination of reverse phase evaporation and extrusion through polycarbonate membranes. *Biochim. Biophys. Acta.* 601:559-571.
29. Ertel, A., A. G. Marangoni, J. Marsh, F. R. Hallett, and J. M. Wood. 1993. Mechanical properties of vesicles. I. Coordinated analysis of osmotic swelling and lysis. *Biophys. J.* 64:426-434.
30. Hope, M. J., M. B. Bally, G. Webb, and P. R. Cullis. 1985. Production of large unilamellar vesicles by a rapid extrusion procedure—Characterization of size distribution, trapped volume and ability to maintain a membrane-potential. *Biochim. Biophys. Acta.* 812:55-65.
31. Mayer, L. D., M. J. Hope, and P. R. Cullis. 1986. Vesicles of variable sizes produced by a rapid extrusion procedure. *Biochim. Biophys. Acta.* 858:161-168.
32. Frisken, B. J., C. Asman, and P. J. Patty. 2000. Studies of vesicle extrusion. *Langmuir.* 16:928-933.
33. Hunter, D. G., and B. J. Frisken. 1998. Effect of extrusion pressure and lipid properties on the size and polydispersity of lipid vesicles. *Biophys. J.* 74:2996-3002.
34. Haugland, R. P. 1996. *Handbook of Fluorescent Probes and Research Chemicals, Sixth Edition.* Eugene, OR: Molecular Probes, Inc.
35. Sanny, C. G., and J. A. Price. 1999. Analysis of nonlinear quenching of terbium(III):dipicolinic acid complex fluorescence by chelators and chelate-conjugated macromolecules. *Bioconjug. Chem.* 10:141-145.

36. Rosen, D. L., C. Sharpless, and L. B. McGown. 1997. Bacterial spore detection and determination by use of terbium dipicolinate photoluminescence. *Anal. Chem.* 69:1082-1085.
37. Wilschut, J., N. Duzgunes, R. Fraley, and D. Papahadjopoulos. 1980. Studies on the mechanism of membrane-fusion—Kinetics of calcium-ion induced fusion of phosphatidylserine vesicles followed by a new assay for mixing of aqueous vesicle contents. *Biochemistry.* 19:6011-6021.
38. Aranda, F. J., M. P. Sanchez-Migallon, and J. C. Gomez-Fernandez. 1996. Influence of alpha-tocopherol incorporation on Ca(2+)-induced fusion of phosphatidylserine vesicles. *Arch. Biochem. Biophys.* 333:394-400.
39. Bentz, J., N. Duzgunes, and S. Nir. 1983. Kinetics of divalent-cation induced fusion of phosphatidylserine vesicles—Correlation between fusogenic capacities and binding affinities. *Biochemistry.* 22:3320-3330.
40. Lopezmarin, L. M., D. Quesada, F. Lakhdarghazal, J. F. Tocanne, and G. Laneelle. 1994. Interactions of mycobacterial glycopeptidolipids with membranes—Influence of carbohydrate on induced alterations. *Biochemistry.* 33:7056-7061.
41. Srinivas, S. K., R. V. Srinivas, G. M. Anantharamaiah, J. P. Segrest, and R. W. Compans. 1992. Membrane interactions of synthetic peptides corresponding to amphipathic helical segments of the Human-Immunodeficiency-Virus Type-1 envelope glycoprotein. *J. Biol. Chem.* 267:7121-7127.
42. van Kan, E. J. M., A. van der Bent, R. A. Demel, and B. de Kruijff. 2001. Membrane activity of the peptide antibiotic clavanin and the importance of its glycine residues. *Biochemistry.* 40:6398-6405.
43. Olbrich, K., W. Rawicz, D. Needham, and E. Evans. 2000. Water permeability and mechanical strength of polyunsaturated lipid bilayers. *Biophys. J.* 79:321-327.
44. Silvius, J. R. 1982. *Lipid-Protein Interactions*. New York: John Wiley & Sons, Inc.
45. Furuya, K., and T. Mitsui. 1979. Phase-transitions in bilayer membranes of dioleoyl-phosphatidylcholine-dipalmitoyl-phosphatidylcholine. *J. Phys. Soc. Japan.* 46:611-616.
46. Sukharev, S., S. R. Durell, and H. R. Guy. 2001. Structural models of the MscL gating mechanism. *Biophys. J.* 81:917-936.
47. Needham, D., and R. S. Nunn. 1990. Elastic deformation and failure of lipid bilayer membranes containing cholesterol. *Biophys. J.* 58:997-1009.
48. Kloda, A., and B. Martinac. 2001. Mechanosensitive channel of *Thermoplasma*, the cell wall-less archaea: Cloning and molecular characterization. *Cell Biochem. Biophys.* 34:321-347.

49. Perozo, E., A. Kloda, D. M. Cortes, and B. Martinac. 2002. Physical principles underlying the transduction of bilayer deformation forces during mechanosensitive channel gating. *Nat. Struct. Biol.* 9:696-703.
50. Shapovalov, G., R. Bass, D. C. Rees, and H. A. Lester. 2003. Open-state disulfide crosslinking between *Mycobacterium tuberculosis* mechanosensitive channel subunits. *Biophys. J.* 84:2357-2365.
51. Maurer, J. A., and D. A. Dougherty. 2001. A high-throughput screen for MscL channel activity and mutational phenotyping. *Biochim. Biophys. Acta.* 1514:165-169.